Enviroment of Deposition, Geochemistry, and Diagenesis of the Beda Formation, SW Sirte Basin, Libya

by

BASHIR BASHIR GAREA

This thesis is submitted for the degree of Master of Science (by Research) at the University of Glasgow, Department of Geology and Applied Geology, May 1991

ProQuest LLC.
789 East Eisenhower Parkway
P.O. Box 1346
Ann Arbor, MI 48106 – 1346

DECLARATION

The material presented in this thesis is the results of independent research by the author undertaken between October 1989 and May 1991 at the Department of Geology and Applied Geology, University of Glasgow. Any published or unpublished papers have been given full acknowledgment in the text.

B. B. Garea

Dr. C. J. R. Braithwaite

Department of Geology and Applied Geology
University of Glasgow

ACKNOWLEDGEMENTS

First, I wish to express my thanks to the management of Zueitina Oil Company and in particular the management of the Exploration Department for giving me this opportunity, for the scholarship, and for the release of the data without which this research would not have been possible.

I would like to thank my supervisor, Dr. C. J. R. Braithwaite, for his help and constant support, guidance, generous discussions, and constructive advice throughout this project. I would also like to thank Professor B. E. Leake and the staff of the Department of Geology and Applied Geology for their help and understanding, and for making available the department facilities and resources. I also extend my thanks to my friends and colleagues in the department. I am also grateful to the technicians of the department, especially, Mr. D. Turner, Mr. M. Macleod, Mr. P. Wallace, Mr. J. Gallagher, and Mr. P. Ainsworth for their continuous assistance during the course of this research.

My thanks also go to Dr. A, E. Fallick and Dr. A. Boyce from the Isotope Geology Unit at SURRC for their permission to make use of the Unit facility, and for their very helpful and constructive remarks.

Finally, special thanks go to my parents for their patience and concern, and to my wife and my sons Mohammed and Ali for their patience, understanding, and support.

TABLE OF CONTENTS

page

List of Figures

page

List of Tables

List of Plates

ABSTRACT

The study of the Middle Paleocene Beda Formation, in block NC74F of the southwestern Sirte Basin, was undertaken to investigate the environment of deposition, the geochemistry, the subsequent diagenetic history, and the resultant porosity of part of the lower member of this formation.

Six lithofacies (F1-F6), characterized by shallow-marine sediments (mudstones and wackestones), dolomite, sulfates, and argillaceous carbonate with thin shale interbeds, were recognized in these sediments showing contrasting lateral and vertical distribution. These facies represent three small-scale shallowing-upward cycles. The lower two cycles of the succession begin in the lagoonal part and accrete through intertidal to supratidal sediments, whereas, the third cycle at the top of the succession begins with a new marine transgression, and is terminated by a laterally widespread evaporite sulfate unit.

Geochemical results show strikingly high values of strontium (Sr), while other trace elements (reported in their oxide forms), such as iron (Fe), manganese (Mn) etc., are generally low. The high Sr values are due to the precipitation of minor amounts of celestite (detected by XRD) in the sediments. The Isotopic study shows that the Beda dolomites are depleted in ^{18}O with quite negative $\delta^{18}O$ values ranging between -1.5 to -5.7 per mil (PDB). The $\delta^{13}C$ values of these dolomites tend to show a more marine $\delta^{13}C$ isotopic signature, with an average of +3.27 per mil (PDB). The sulfur $\delta^{34}S$ isotope data measured from the evaporite facies ranges between 19.8

and 22.28 per mil (CDT), and these are generally within the range of $\delta^{34}S$ isotope values characteristic of marine evaporites of Tertiary age.

Diagenesis of the Beda sediments studied has resulted in a number of diagenetic changes. These are dominated by cementation, dissolution, dolomitization, and compaction. Two generations of calcite cements were recognized. The first generation of cement occupied the original intergranular and intragranular porosity, while the second filled residual primary pores and molds and vugs resulting from the first stage of dissolution. Dolomitization followed at least the first phase of calcite cement, and 60-70% of the studied intervals have been dolomitized. On the basis of the sedimentological, petrographic, and geochemical evidence, the dolomite is interpreted as of early, near-surface origin, associated with hypersaline conditions. Evidence of a second stage of dissolution is found as secondary voids and molds filled with calcium sulfates (gypsum-anhydrite). This postdates calcite cementation and dolomitization. The late (or burial) diagenetic events recognized are development locally, of baroque dolomite cement, and Pb-mineralization.

Examination of porosity data from porosity logs shows a wide range of variation in total porosity and shows a general increase in porosity in an eastward direction. This is because the porosity has been less affected by sulfates cementation relative to the western part of the study area.

CHAPTER ONE
INTRODUCTION

The term Beda Formation was first introduced in the study of the subsurface of the western Sirte Basin, Libya, by Barr and Weggar (1972). Generally the Beda Formation of the whole basin varies in thickness from a few meters to hundreds of meters and it has locally been informally subdivided into two members. In much of the southwestern part of the basin (e.g. in the study area) it is divided into an Upper member and a Lower member, while in the Dahra-Hofra area, in the northwestern part of the basin, it is divided into the Thalith member and the Rabia shale member which are, respectively, equivalent to the Lower and Upper members. Potentially, the upper part of the Lower member of the Beda Formation of the study area (Zueitina Oil Company block NC74F), and in particular in the Sabah oilfield, is considered a primary reservoir for hydrocarbon accumulation.

1.1 Purpose of Study

The purpose of the present research has been to examine the sedimentology, the petrography and geochemistry of part of the Lower member of this formation, including the reservoir interval, in an attempt to understand the facies distribution and the depositional environment of this part of the Beda Formation, and the geochemistry and the diagenetic processes influencing reservoir porosity. The study is based on the analysis of a number of core samples from five exploratory and production wells.

These wells (E2, F1, D2, G41, and G4) penetrated the Beda Formation at various depths ranging from approximately 1316 to 1678 metres (4318 to 5505 ft) below sea level. These core samples represent mostly, the upper part of the Lower member and cover a total of approximately 30 metres (≈110 feet).

1.2 Study Area

The study area (Fig. 1.1) is located in the southwestern part of the Sirte Basin between latitude 27° 45` and 28° 15` N and longitude 17° 20` and 18° 30` E. This area was probably dominated throughout the deposition of the Beda Formation by a generally flat-topped and gently subsiding platform which is indicated by a fairly constant thickness of this formation, approximately 300 meters (≈1000 feet) thick, as determined from wells B1 and H1. The area was probably sloping gently to the east-northeast with this slope marked by a slight increase in thickness of this formation in the same direction. The structural configuration of this area was changed during the remainder of Paleocene time, as faulting became evident, especially in the western and eastern parts (Fig. 1.2). During the Quaternary and probably very recently, the area has been affected by the eruption of volcanic activity represented by the Al Haruj Al Aswad formation. This volcanic activity has important implications, for example, on the diagenesis of Paleocene rocks in the study area. The present day structural confiquration of the study area is dominated by the Zella trough in the west, the El-Haleigh High in the central part and the Gerad trough in the east.

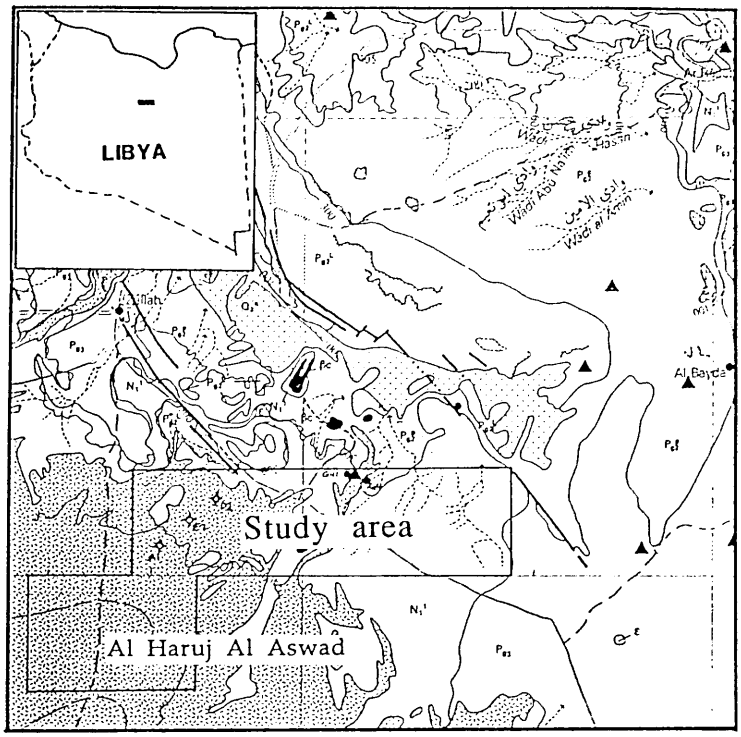

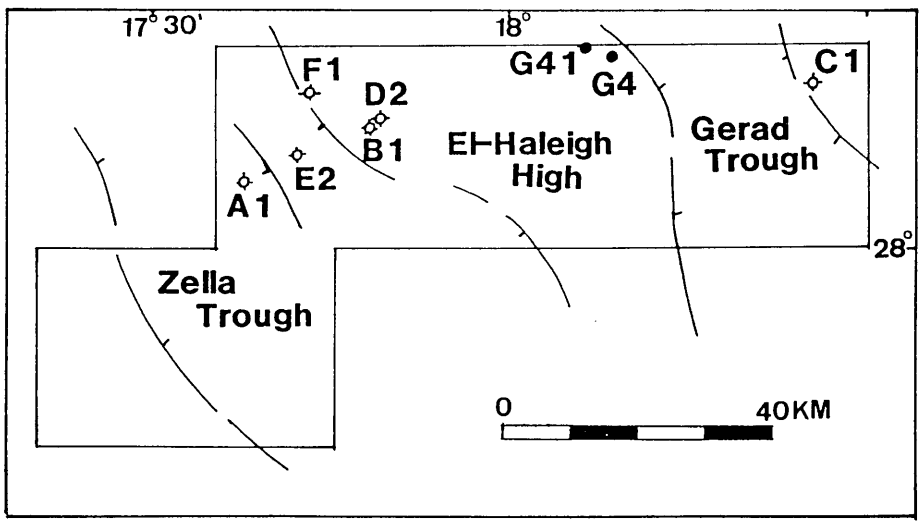

Fig. 1.1, Location map of the study area, showing the present geological setting (top), and the main structural configuration and well location (bottom) of the area.

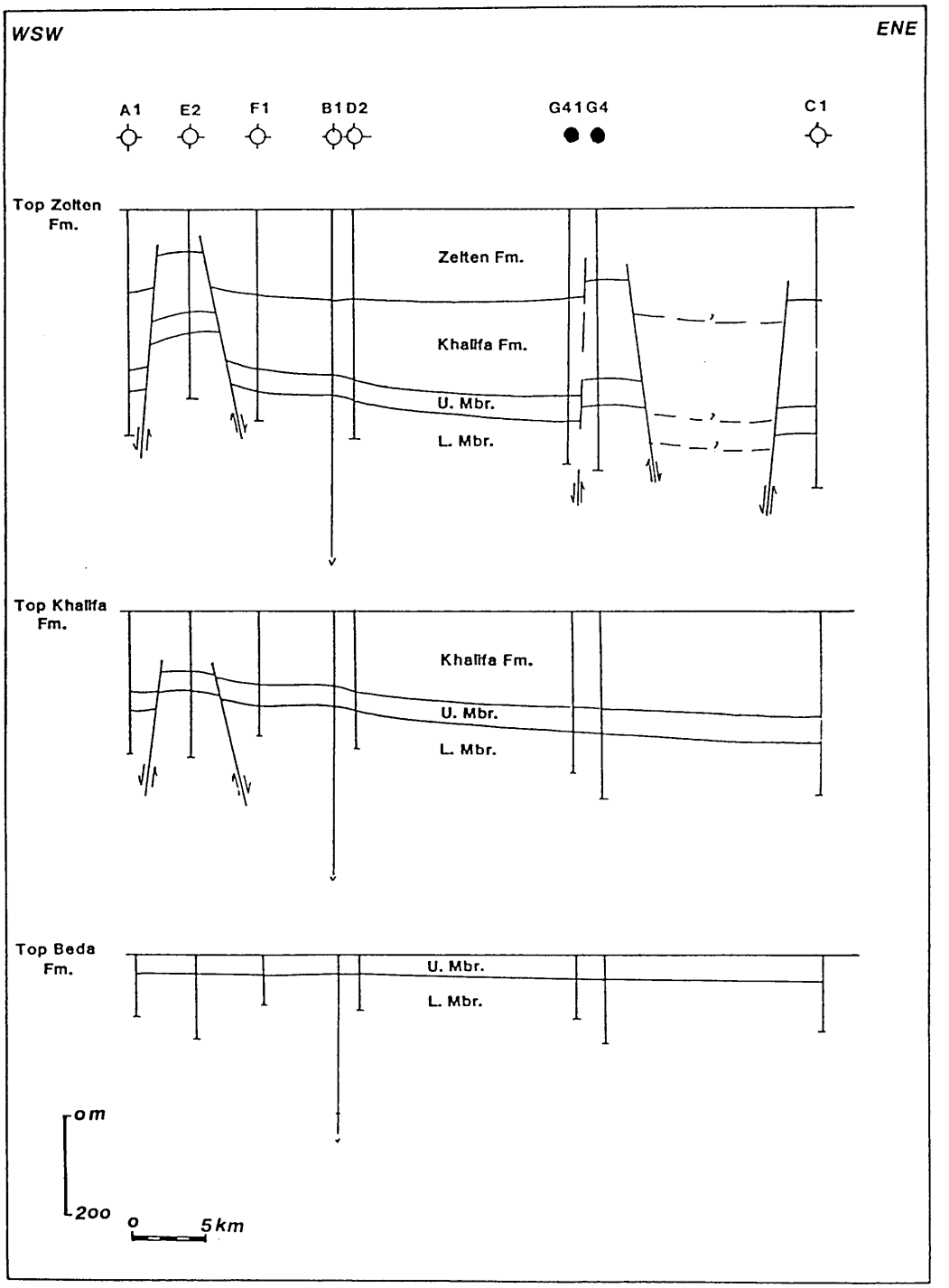

Fig. 1.2, WSW-ENE structural cross-section, using backstripping technique, to illustrate the structural development from the time of deposition of the Beda Formation to near the end of the Paleocene (e.g. the end of the deposition of the Zelten Formation).

1.3 Previous Work

A great deal of work has been carried out in the past on the geology of Libya including the Tertiary and in particular the Paleocene deposits, both in outcrops and in subsurface. Most of this work has described the Paleocene lithofacies in general and has studied the biotic constituents of these facies.

Jordi and Lonfat (1963) descibed the stratigraphic relationships and named the Paleocene units which crop out in northwestern Libya. Furst (1964) studied in detail the same interval exposed along the western and southwestern margins of the Sirte Basin. He attributed the deposition of the middle Paleocene Had Limestone Member, equivalent to the Beda Formation, to the shallowing of the early Paleocene sea. Gohrbandt (1966) also described the general stratigraphic relationships of the Paleocene rocks exposed on the western and southwestern margins of the basin.

Conley (1971) studied the Paleocene units deposited in the subsurface of the Sirte Basin and described in some detail the lower and middle Paleocene lithofacies. He concluded from the stratigraphical, paleontological and lithological evidence that the Paleocene interval in the subsurface is equivalent to that in outcrops and that the sequences are similar, both vertically and laterally.

Berggren (1969 and 1974) discussed the foraminiferal bio-stratigraphy of the Tertiary deposits of the basin where he has recognized a complete sequence of Paleocene foraminifera. He subdivided the Paleocene sequence into five planktonic foraminiferal zones (P1-P5), and assigned a

Montian age to the middle Paleocene unit (e.g. the Beda Formation). Berggren also recognized two distinct lithofacies; shales and marls, containing middle and outer-shelf fauna, and carbonates containing an inner and middle-shelf fauna.

1.4 Methods of Study

A brief outline of the various methods used in this study will be mentioned in this section. However, a more detailed summary of each of these methods will be described at their relavent chapters.

The initial phase of investigation was carried out by describing all the core samples available under the binocular microscope. Following this, more than 130 thin-sections were prepared and petrographically studied, using conventional microscopy and cathodoluminescence (CL) methods. The scanning electron microscope (SEM) was also used to provide exquisite images of porosity and of the tiny clay components of the rock samples.

Geochemical analyses, including calcite-dolomite ratio determination, trace element compositions and major and minor oxides, were carried out using X-ray diffraction (XRD), and X-ray fluorescence (XRFS). Carbon, oxygen and sulfur isotope analyses were also made on a number of samples. Porosity wireline logs were used to determine porosity data of the Beda Formation, and approximately 30 meters (≈110 feet) of this formation were analyzed.

1.5 Problems

Since there is often some difference between depths recorded during drilling operations and those recorded during wireline logging operations, the depths of the considered cored intervals recorded by the driller were, whenever possible, depth-corrected to their depths on the wireline logs. Here the amount of correction applied to these depths, is approximately 2.0 meters (≈7 feet) in well E2, approximately 0.6 meters (≈2 feet) in well F1, and about 0.3 meters (≈1 foot) in well D2. No correction was applied to wells G4 and G41. The second problem encountered during the course of this study was that some core samples had been either displaced and/or inverted. For example core 2 in well G4 is believed to be both displaced and inverted, and the upper most part of the cored interval in well D2 was probably displaced (see Appendix A).

Basically, these discrepencies were considered and corrections were applied. However, the lithologic and petrographic descriptions of core 2 of well G4 were only used as complementary data and were not considered in the correlation.

1.6 Geologic History

1.6.1 General

Libya as a whole is a cratonic basin on the northern fringe of the African shield between latitudes 20° and 33° N and between longitudes 10° and 25° E (Fig. 1.3), covering an area of about 1.6 million square kilometres. Its present day tectonic framework is the result of several orogenic movements ranging from the Caledonian to the Alpine. The country is divided into five sedimentary basins, namely the Ghadames, Murzuk, Kufra, Marmarica, and Sirte Basins which are separated by intervening uplifted arches.

Since the early Paleozoic, the country has been the site of several transgressions and regressions by the sea, resulting in the accumulation of a wide variety of sedimentary rocks (Conant and Goudarzi, 1967). The Paleozoic seas, up through the Carboniferous, were widespread across the country and in late Carboniferous a general regression occured as a result of the Hercynian (Variscan) Orogeny. Throughout this time all the basins with the exception of the Sirte Basin were active and received thick accumulations of Paleozoic sediments varying from continental sands to marine carbonates and shales.

During the Permian and Triassic, only the two northern basins; the Ghadames and the Marmarica Basin were covered by the sea while the rest of the country remained emergent. In the Jurassic the sea began to encroach covering an area further south in the Ghadames Basin and in

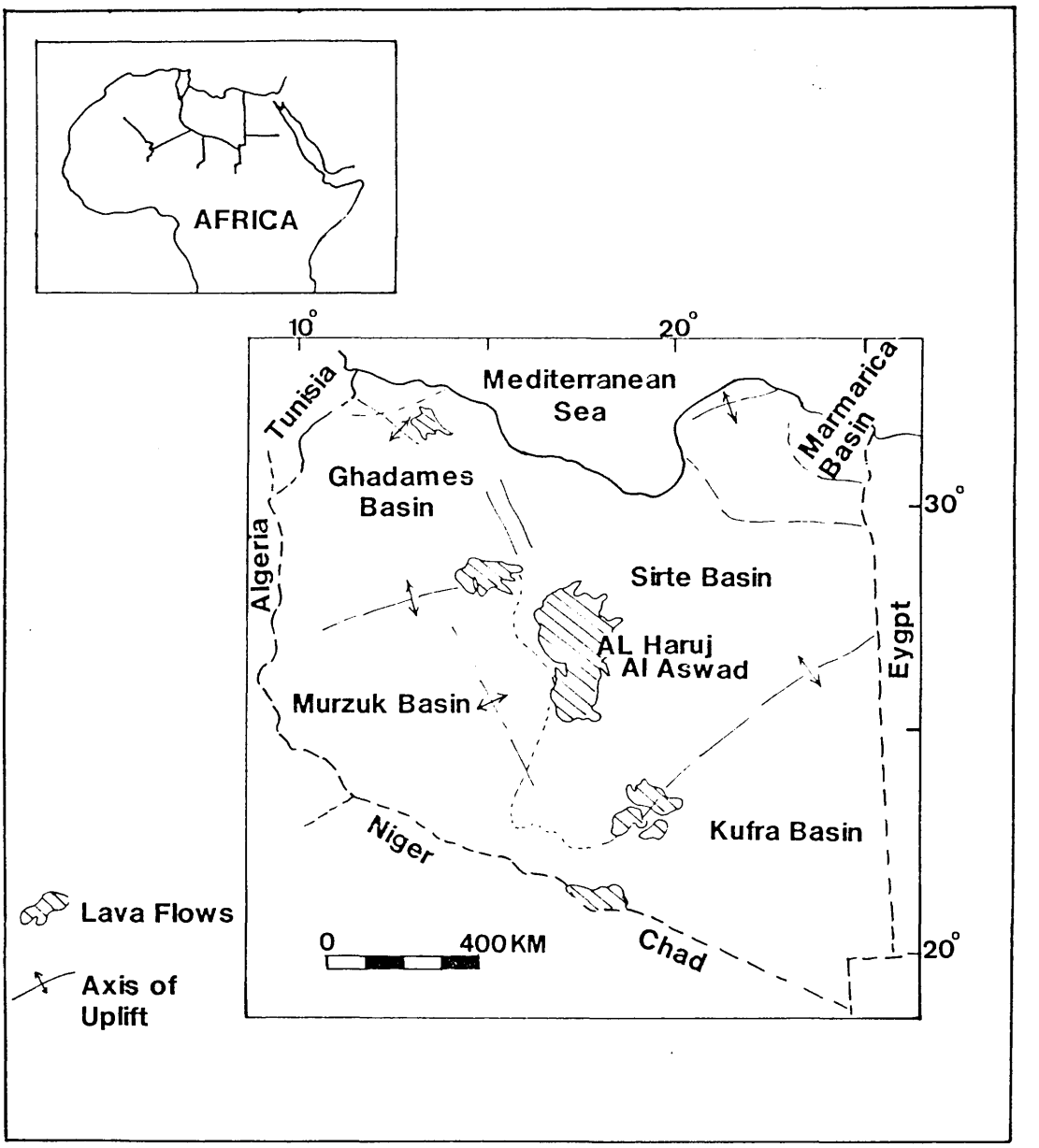

Fig. 1.3, Location and general tectonic framework of Libya, showing the distribution of basins and the main Caledonian-Hercynian axes of uplift. (after Conant and Goudarzi, 1966).

Cyrenaica where terrigenous clastics, carbonates and evaporites were deposited unconformably over Paleozoic sediments.

In the early Cretaceous a regression of the sea took place in the Ghadames Basin area while the Cyrenaica area remained covered by shallow seas until the beginning of the late Cretaceous (Cenomanian). At this time a major tectonic event occured which resulted in the collapse of the paleo-Sirte arch and the opening of the Sirte Basin. Consequently, the northern half of the country was invaded and covered by the sea and as a result the stratigraphic section is dominated by deep marine shales deposited in the trough and by shallow marine carbonates deposited on the high areas.

At the beginning of the Tertiary (Paleocene), the sea continued advancing southward, reaching almost as far south as the 22^{o} parallel, and in early Eocene time, a partial regression occurred to about the 28^{o} parallel (Desio, 1971). The Tertiary deposits, are generally dominated by deep and shallow water sediments, shales, carbonates, and evaporites but in the late Tertiary and particularly since Oligocene time, extensive volcanic activity occured covering a large area in the central and western part of the country, where large basal plateaus were formed by abundant lava flows.

1.6.2 Sirte Basin.

The Sirte Basin is the youngest and most prolific (hydrocarbon) basin in north central Libya. This area was a broad upland early in the Mesozoic (Conant and Goudarzi, 1967) but during the middle Mesozoic the basin

began to form, and by the Cenomanian the pattern of the Sirte Basin was established. Tectonically, it is a northwest elongated basin with a complex structural pattern of northwest-southeast trending horsts and grabens. The western and eastern boundaries of the basin are considered to be the Hun Graben and the edge of the Cyrenaican platform respectively (Fig. 1.4).

After the opening of the Sirte Basin, a late Cenomanian-Turonian transgression (Barr, 1972) spread southward into the subsiding grabens and eventually onto the low-standing highs which were subsiding at a slower rate. Subsidence was also relatively slow during the Coniacian-Santonian but during the Campanian, a sudden increase in the subsidence rate occurred (Gumati and Kanes, 1985; Gumati and Naire, 1991). During this time, the transgression continued southward and by the late Cretaceous (Maastrichtian)-Paleocene the sea had reached its southernmost extent at the 22^{o} parallel (Desio, 1971) and consequently, most of the major highs were inundated. Through the Cenomanian-Turonian the rate of sedimentation kept pace with the rate of subsidence and hence, shallow marine sedimentation dominated. The shallow marine conditions continued until the Coniacian-Santonian when deeper marine conditions prevailed and thick accumulations of organic-rich shales and deep marine carbonates were deposited in the troughs while deposition of open shallow marine or reefoidal sediments continued on the highs.

During the Tertiary, the Sirte Basin continued to subside, reaching a maximum subsidence during the Eocene (Berggren, 1974; Gumati and Kanes, 1985). Consequently, marine sedimentation continued through the Paleocene and early to middle Eocene. Paleocene deposition became mixed and included both deep and shallow marine sediments as movements

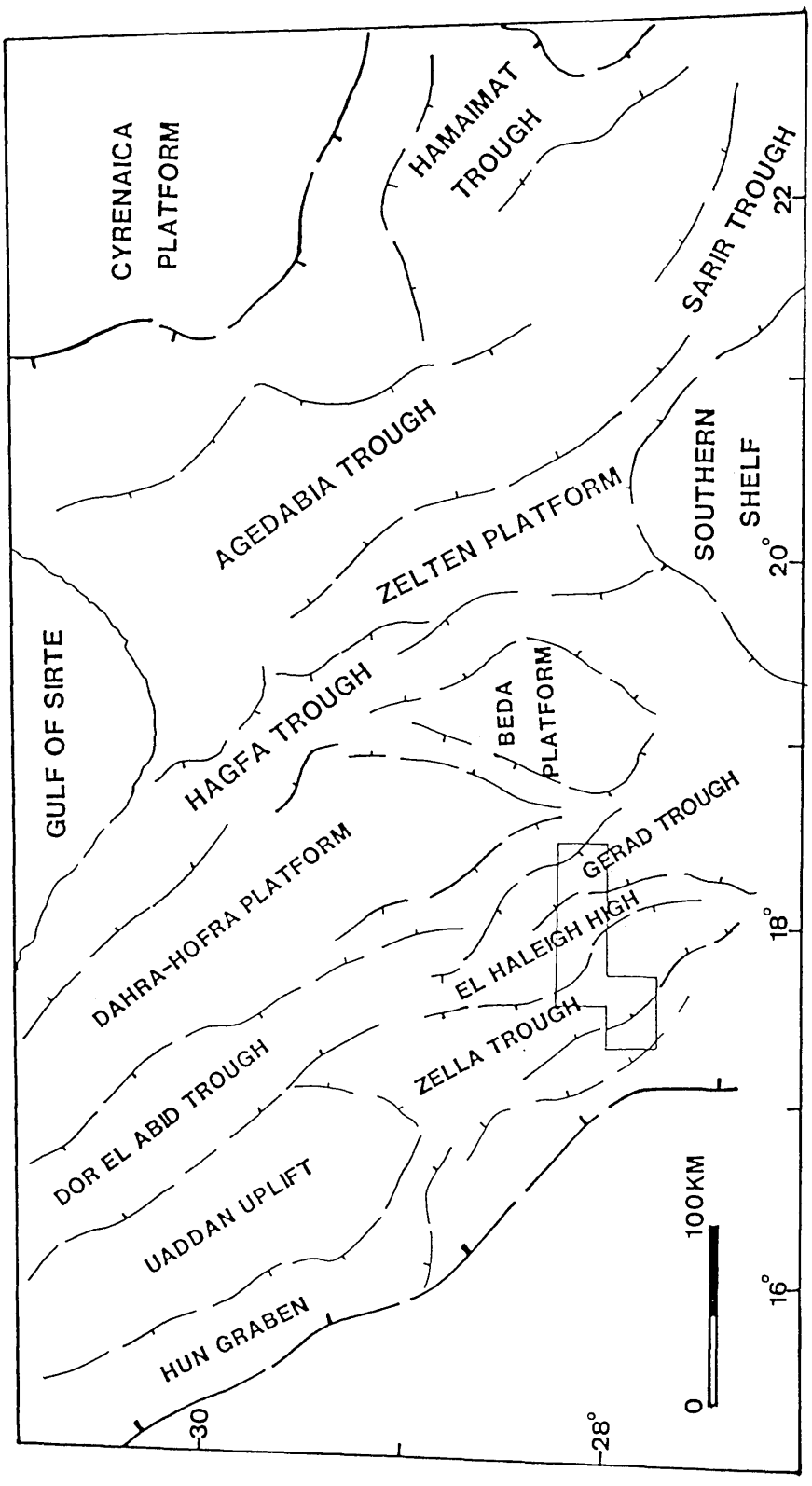

Fig. 1.4, Tectonic framework of the Sirte Basin, showing the distribution of the major troughs and grabens of the basin relative to the study area.

continued along the faults. During the early Eocene, a partial regression occurred creating restricted conditions and evaporite deposition over the south-western part of the basin, while open marine conditions prevailed in the rest of the basin. In the middle Eocene, a marine transgression eliminated the restrictions and marine sedimentation occurred. This transgression continued until the Quaternary, when the basin was covered by continental sedimentation.

1.7 Paleocene Stratigraphy

Paleocene sediments are dominated by thick sequences of shales and carbonates which were deposited in a transgressive sequence at depths of approximately 200 meters or slightly deeper (Berggren, 1974). The onset of the Paleocene (Danian) is characterized by the deposition of open marine shales (the Hagfa Shale), and at the close of the Danian conditions often favored the deposition of shallow water carbonates which exhibit a full range of variety in biotic constituents, structural fabrics and diagenetic modifications (Colley, 1963).

In the late Paleocene, less extensive shale sequences; mostly calcareous shales and carbonates, were deposited. These facies changes from widespread deposition of shales to shallow-shelf carbonates and the return to shales may have resulted from changes in the sediment supply, from reactivation of faults, or from rapid subsidence (Conley, 1971).

Generally deposition from the late Cretaceous (Maastrichtian) to the early Paleocene (Danian) was continuous, but despite this continuity, the

Cretaceous-Tertiary boundary can be readily determined by the occurrence of large foraminifera such as Omphalocyclus macroporus and Siderlites calcitrapoides or the pelagic foraminiferal assemblage including Globotruncana gansseri and Globotruncana spp, that marks the upper Cretaceous (Lehmann, 1964). In contrast the Paleocene-Eocene boundary occurs within a calcareous shale and carbonate sequence, the Kheir Formation, and is somewhat difficult to determine in some cases (Berggren, 1969).

The Paleocene sequence (Fig. 1.5) shows broadly, two sedimentary cycles each of the order of 300 meters thick. These cycles are bound by abrupt stratigraphic contacts and show shale-based or shale dominated units in the lower parts, passing up into limestone-dolomite in their upper parts. These cycles could well be the result of variable subsidence rates and local tectonic movements of the Sirte Basin which took place during the Paleocene. The lithostratigraphic units of the Paleocene sequence penetrated in the study area will be described below, following the nomenclatural scheme of Barr and Weegar (1972). These are, in ascending order, as follows,

1) Hagfa Shale Formation

Based on the planktonic foraminiferal assemblages (e.g. Globo-conusa daubjergensis, Globorotalia pseudobulloides etc.), the Hagfa Formation was interpreted by Berggren (1969) as corresponding to the Danian stage. Stratigraphically, this formation conformably overlies the Maastrichtian Kalash Formation and is conformably overlain by the Beda Formation.

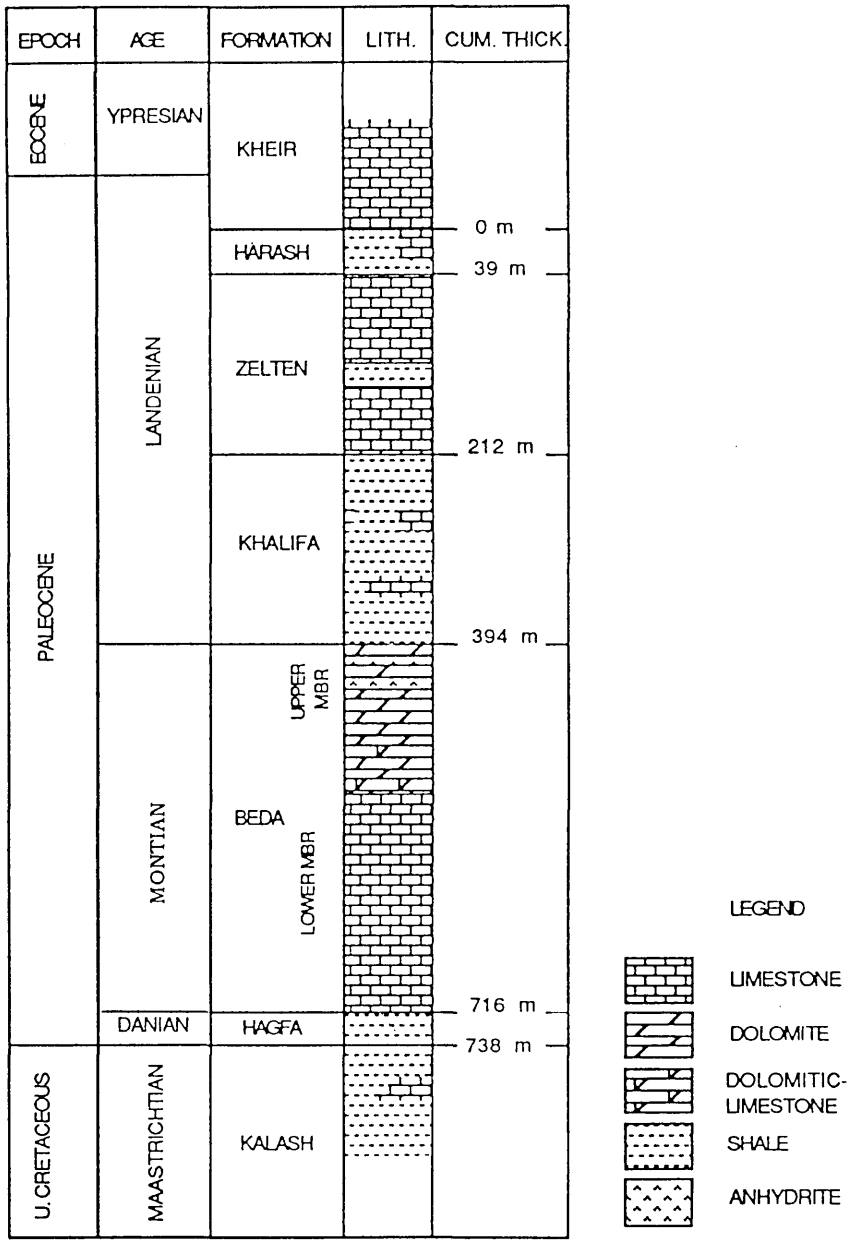

Fig. 1.5, Stratigraphic section, showing the Paleocene sequence and lithology of the study area.

In the study area, the Hagfa shale is represented by approximately 22 meters of shale; grey green and black, soft, calcareous and fissile. Abundant planktonic and also smaller benthonic foraminifera, are present including Valvulineria1, Lenticulina1, Chiloguembelina sp and Gyroidina sp (Tmalla, 1987). The Hagfa Formation becomes increasingly calcareous in eastern and south central parts of the Sirte Basin where it passes respectively into the Lower Sabil Carbonate (e.g. in the Harash and Augila areas) and the Defa Limestone in the Defa oilfield. In the Dahara-Hofra area, north of the study area, it becomes stratigraphically equivalent to the Upper Member of the Satal Formation (Fig. 1.6). The abundance of planktonic forams indicates that this formation was deposited in a fairly deep, open marine environment (Barr and Weegar, 1972).

2) Beda Formation

The Beda Formation is considered to be Montian (middle Paleocene) in age (Berggren, 1969). It conformably overlies the Hagfa Shale, deposited in the central and western Sirte Basin, the Defa Limestone in the Defa oilfield in the south central Sirte Basin, and the Satal Formation (carbonates) deposited in the Dahra-Hofra area in the northwestern part of the basin. It is conformably overlain by the Khalifa Shale Formation in the central and eastern Sirte Basin (e.g. in the Ora and Samah oilfields), and by the Dahra Formation in the Dahra-Hofra area. Laterally, the Beda Formation becomes equivalent to the Had Limestone of Jordi and Lonfat (1963) and the Scedida Dolomite of Furst (1965) which are exposed along the southwestern border of the Hun Graben on the western and southwestern margins of the Sirte Basin. In the subsurface, the Beda Formation is

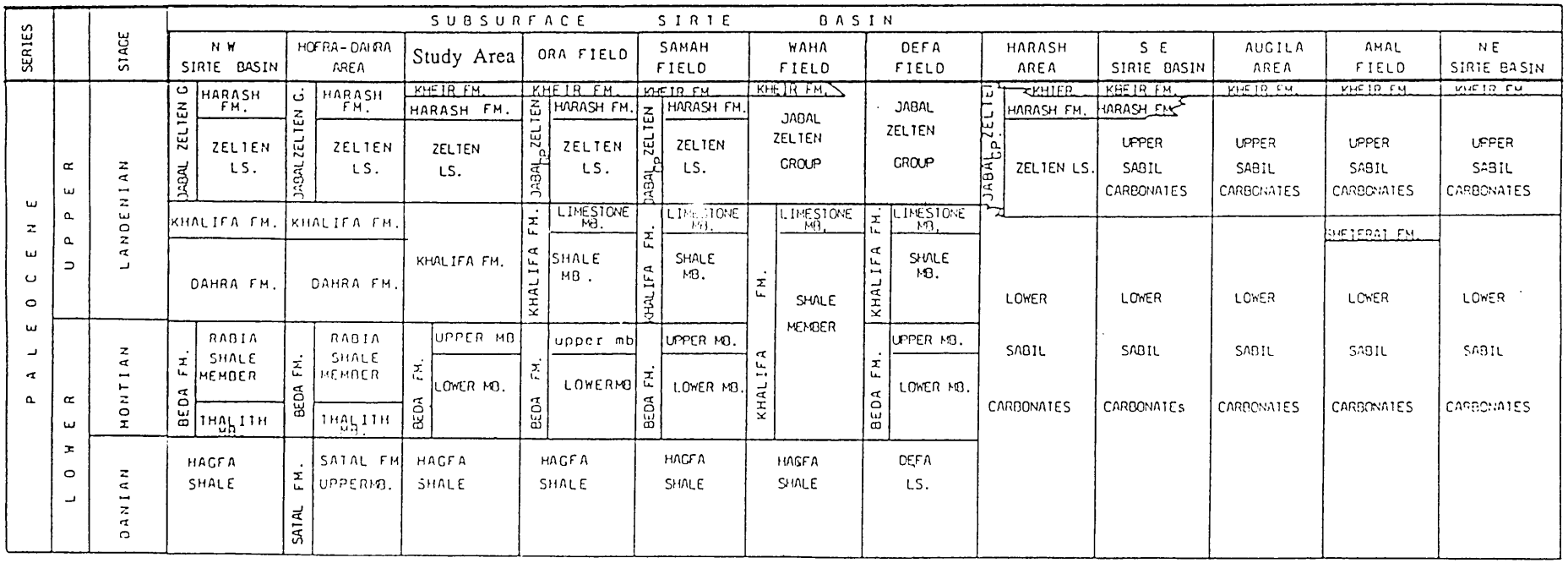

Fig. 1.6, Correlation chart, showing the regional correlation of the Paleocene sequence in the Sirte Basin. (modified after Barr & Weegar, 1971).

equivalent to the Khalifa Formation present in the Waha oilfield and the Lower Sabil Carbonates of Barr and Weggar (1972) present, for example, in the Amal oilfield and the Harash and Augila areas in the eastern part of the basin (Fig. 1.6).

In the study area, the Beda Formation conformably overlies, usually with an abrupt contact, the Hagfa Shale Formation and is conformably overlain by the Khalifa Shale Formation. The Lower member of the Beda Formation is characterized by approximately 250 meters (820 feet) of mainly limestone and dolomite with abundant calcium sulfates, gypsum and anhydrite, present throughout although their abundance decreases with depth.

The upper part of this formation is represented by approximately 50 meters (164 feet) of anhydrites and shales with carbonate interbeds. The shales are dark grey in colour and pyritic. The carbonate units are generally light grey-grey in colour, argillaceous, and pyritic, occasionally becoming marly.

3) Khalifa Formation

The Late Paleocene (Landenian) Khalifa Formation of the study area conformably overlies the Beda Foramtion and is conformably overlain by the Zelten Formation. The contact is often gradational at the base, while the top is marked by a sharp change in lithology (Barr and Weegar, 1972). Laterally, the Khalifa Formation passes into the Lower Sabil Carbonates in

the eastern Sirte Basin and western areas as the lower part of the formation becomes stratigraphically equivalent to the Dahara Formation (Fig. 1.6).

The Khalifa Formation is represented by approximately 182 meters of shale with minor limestone interbeds. The shales are dark grey or black in colour, slightly calcareous, fissile and slightly pyritic. The limestones are mainly wackestones, argillaceous, grey or occasionally tan to off-white with abundant benthonic foraminifera, including common miliolids and rotaliids. Ostracods and echinoderm fragments are also observed (Tmalla, 1987). Generally, this formation represents a shallow to open marine environment of deposition (Barr and Weegar, 1972).

4) Zelten Formation

This formation is also Landenian in age. It conformably overlies the Khalifa Formation and is overlain by the Harash Formation. It is widely distributed in most parts of the Sirte Basin, but in eastern and southeastern areas it becomes laterally equivalent to the Upper Sabil Carbonates.

In the study area, this formation consists of approximately 173 meters of limestone with minor amounts of shale. The limestones are predominantly wackestones and occasionally packstones, ranging from off-white to tan to grey in colour. They are slightly argillaceous and locally become chalky. Abundant foraminifera are present, including larger forms such as Nummulites and Cibicides spp, (Tmalla, 1987). Bryozoan and echinoderm fragments are also present.

Generally, the Zelten Formation represents a variety of shallow marine to offshore environments of deposition. For more details, the reader is referred to Bebout and Pendexter (1975).

5) Harash Formation

The Harash Formation was deposited during the Landenian stage, near the end of the Paleocene. In the study area, this formation shows an abrupt contact with the underlying Zelten Formation and is conformably overlain by the late Paleocene-early Eocene Kheir Formation.

The formation is characterzed by approximately 39 meters of limestone and shale interbeds. The limestones are predominantly wackestones and occasionally packstones. They are mostly tan to grey, and are occasionally argillaceous and chalky. The lower part is generally shales which are dark grey, fissile, calcareous and pyritic.

The fossil assemblages of this formation resemble very much those described from the Zelten Formation. Hence, the environment of deposition was probably also shallow to open marine.

6) Kheir Formation

The lowermost part of this formation is considered to be Landenian in age and it marks the end of the Paleocene system. In the study area, this part is characterized by light grey to grey argillaceous wackestones which

become marly at the base. The fossil assemblages of this part represent a continuation from the underlying Harash Formation.

CHAPTER TWO
LITHOFACIES AND ENVIRONMENT OF DEPOSITION

This chapter documents the description of the different depositional facies of the studied interval of the Beda Formation, and their inferred environments of deposition. These were revealed from a detailed study of approximately 30 metres of cores from five wells in the study area, ranging between approximately 3 to 33 kilometres apart, and from the study of more than 130 thin-sections.

2.1 Methods and Technique

2.1.1 Microscopy

The cores were slabbed and the samples were examined in detail under a binocular microscope. After this initial examination, samples were then selected from which thin-sections were made. All thin-sections were impregnated with blue colored resin, left uncovered and polished. One-half of each section was stained with Alazrin red-S and Potassium ferricyanide ARS/PF dual stain. This staining differentiates calcite, dolomite, and ferroan varieties of each. As a result of this stain, calcite accepts a pink colouration, ferroan dolomite accepts blue colouration and non-ferroan dolomite remains colourless (Dickson,1966; Friedman,1959). The thin-sections were then studied using conventional microscopy and cathodoluminescence. The scanning electron microscope (SEM) was used

on number of samples to provide detailed information on the pore geometry and on the smaller components present. The energy dispersive X-ray (EDX) allowed qualitative analysis and hence identification of clays.

2.1.2 X-Ray Diffraction (XRD)

The total calcite and dolomite contents of samples in this interval were obtained using x-ray diffraction analysis. The use of XRD specifically for this purpose has been carried out by several workers (e.g., Tennant and Berger, 1957; Royse et al., 1971; etc.).

In this study, samples were selected at approximately one-foot intervals and prepared by grinding a few fragments of the sample for a few minutes. Enough acetone was then added to the powder to form paste and the mixture spread on one-half of one surface of a petrographic glass slide. The prepared slides were then analyzed in a highly stabilized x-ray unit using Iron filtered Cobalt K-alpha radiation. The intensities for the 3.03 Å calcite line, and the 2.88 Å dolomite line were measured at 34.31^{o} 2 θ Co K-alpha position and at 36.14^{o} 2 θ Co K-alpha position, respectively.

The maximum heights of the calcite and dolomite peaks at these two 2 θ positions were read off the x-ray produced chart and the peak height ratios were determined and plotted on the experimentally determined graph of Tennant and Berger (1957, Fig. 1) to determine the composition of each sample in term of %dolomite. The use of this graph to estimate dolomite percentages has been confirmed by Royse et al (1971) and they

suggested that the graph can be used to estimate a composition within ± 6% dolomite with 95% confidence level.

Thus, using the obtained dolomite percentages, with the information obtained from samples and thin-sections descriptions, the intervals studied were classified into a number of distinct types of lithofacies.

2.2 Lithofacies

Six lithofacies are recognized within the cored portion of the Beda Formation in the study area. They include (1) foraminiferal wackestone, (2) argillaceous foraminiferal wackestone, (3) dolomite mudstone, (4) Peloidal-foraminiferal wackestone, (5) evaporite (gypsum-anhydrite) and (6) argillaceous dolomite mudstone. The characteristics inherent to each lithofacies are summarized in Table (2.1).

1) Foraminiferal Wackestone Lithofacies (F1)

This facies is characterized by tan to light grey limestones, dominated by an abundance of benthonic foraminifera, including Miliolids (e.g. Quinqueloculina sp.) and smaller rotaliids such as Discorbis sp. and common dasycladacean algae such as Acetabularia (Acicularia). The foraminifera and the dasycladacean algae make up the bulk of the fossils (Plate 2.1, B-D). Other grains consist of echinoderm fragments and rare peloids (Plate 2.1, E) are also present. The facies is typically stylolitic. The

	Lithofacies F1			lithofacies F2			Lithofacies F3			Lithofacies F4			Lithofacies F6		
	A	C	R	A	C	R	A	C	R	A	C	R	A	C	R
Forams	x			x					x	x					x
Gastropods									x			x			
Echinoids			x			x					x				x
Ostracods									x			x			x
Mollusc fragments						x									
Algae		x													
Peloids			x			x			x		x				
Intraclasts			x		x				x						
Color	tan-light grey			grey-dark grey			tan-brown			tan-brown			dark grey		
Sed. Structs.				burrow mottling			fenestrae, thinly laminated			stromato-lites					
Other features	stylolitic			pyritic, stylolitic			pressure dissolution						pyritic		

Table 2.1, summarizing the characteristics inherent to each lithofacies; (F1) foraminiferal wackestone lithofacies, (F2) argillaceous foraminiferal wackestone, (F3) dolomite mudstone, (F4) peloidal-foraminiferal wackestone, (F6) argillaceous dolomite mudstone. Abundant (A); common (C); rare (R).

stylolites are horizontally oriented, generally irregular, serrated having both high and low amplitude seams which interpenetrate the rock matrix. The lower part of this facies is off-white in color and chalky. Samples of this were studied under the SEM but no fragments of coccoliths were found. However, it shows high intergranular porosity.

Interpretation

Living dasycadacean algae inhibit mainly shallow marine waters and occur most often in tropical and subtropical waters. As a group they seem to prefer normal marine salinities, but the Acetabulariae, for example, tolerate salinities ranging from hypersaline to brackish, and wide variations of temperature. They are mostly found only in low-energy regimes, either below wave base or in protected situations and are typical of the algal flora in marine lagoons (Wray, 1977). The depth of water can be inferred from the presence of the dasycladacean algae. The maximum abundance of living dasycladacean algae is in a depth down to about 5 meters, but they exist in diminishing numbers down to 10 meters with rare occurrences to several tens of meters. Elliott (1968) concluded that the ecological reguirements of fossil dasycladaceans were essentially the same as those of living descendants. They are capable of providing a more than adequate supply of aragonite to form the mud present in the lithofacies.

Miliolid foraminifera are also important as indicators of past environmental conditions. Modern representatives appear to be markedly restricted to certain habitats and flourish particularly in warm shallow waters.

Thus, considering all this evidence, the presence of benthonic foraminifera (i.e. miliolids), and the presence of dasycladacean algae together with the relative rarity of echinoderms and the lack of brachiopods, common bryozoans, and red algae, indicative of fully open marine conditions, this facies was deposited in a shallow, warm, low-energy, and in some way restricted marine environment. The restricted conditions invoke the existence of barriers to form a lagoon. Such barriers may be shelf-edge reefs, coastal irregularities of the inner shelf, or simply an excessive shelf width inhibiting adequate water circulation. In epeiric seas, low-order slopes, great width of shelves, and shallow depth of water are sufficient in themselves to restrict or eliminate water circulation (Irwin, 1965).

2) Argillaceous foraminiferal Wackestone Lithofacies (F2)

This facies is generally grey-dark grey in color. The allochems are again dominated by abundant foraminifera, including miliolids and smaller rotaliids (more rotaliids than miliolids), rare echinoderm fragments, rare large mollusc (bivalve) fragments, and some intraclasts. The upper part of this facies in well E2 is brecciated showing centimeter-size clasts (Plate 2.2, A).

Generally, this facies is argillaceous and pyritic but the sediments display mottled structures, probably as a result of bioturbation (Plate 2.2, B). The pyrite crystals are scattered and mostly associated with gypsum crystals, pressure dissolution seams and low amplitude stylolites (or microstylolites). The pressure dissolution seams and microstylolites,

generally occur with dark brown to black insoluble residues (probably organic matter) concentrated along their surfaces (Plate 2.2, C,D).

Interpretation

This facies probably represents the subtidal deposits of the lagoon formed under reducing conditions. The dark grey color is due primarily to the presensce of organic matter, argillaceous material, and pyrite (iron sulfide). The environment in which this facies was deposited was probably calm or with little agitation. It is likely that during calm periods the water within the sediment became stagnant and eventually reducing and hence pyritic. The overlying water was sufficiently oxygen-rich for faunal and floral growth which is indicated by the different types of fossils present.

3) Dolomite Mudstone Lithofacies (F3)

This facies is represented by dolomite mudstones to wackestones and forms approximately 60-70% of the studied interval. The dolomite is generally microcrystalline to finely crystalline (i.e. crystals less than .03 mm in diameter), and tan to brown in colour. It may be laminated on a millimetre scale (Plate 2.3, A,B) or massive with abundant sulfate (i.e. gypsum and anhydrite) replacement. The laminations are generally present in the western part of the study area (e.g. in wells F1 and D2). The allochems found in this facies are rare forams, gastropods, ostracods, peloids, and intraclasts. The intraclasts here include clasts believed to have been ripped up from the same sediment eroded from nearby exposed areas,

and mud lumps (Plate 2.3, C,D). Sedimentary structures such as fenestrae (birdseyes) are also found, particularly in the upper part of this facies in well D2. The fenestrae (Plate 2.3, E,F) are generally planar and the fenestral pores are filled with either sulfates (mostly gypsum) or calcite.

Interpretation

The characteristic set of depositional features (e.g. laminations and fenestrae) present and the general paucity of fossils provide important clues to the depositional environment of this facies. Laminations, whether thick or thin, are one of the most characteristic features of peritidal carbonates, and are restricted to supratidal and upper intertidal conditions in modern tidal flats. They are found in similar positions in late Paleozoic through Cenozoic sedimentary rocks (Shinn, 1982). The areas under tidal margin conditions are more frequently exposed, and so are unsuitable for marine burrowers, thus there is little destruction of lamination. In subtidal and lower intertidal areas the laminations may not be preserved because of bioturbation.

Fenestral (birdseye) structures are most commonly associated with peritidal environments. Folk (1959) and Laporte (1967) suggested that fenestrae are associated with rocks deposited in very shallow water or in areas intermittently exposed at the time of deposition. Shinn (1968a,1982) noted that these features form in supratidal, intertidal, and even subtidal sediments, but that they are not preserved in the lower intertidal and subtidal environments. They are commonly preserved in the upper part of

the intertidal and increase in abundance through the transition to the supratidal.

The paucity of fossils can also be used as a supporting indicator of the environment of deposition. Of course, on the basis of paucity of fossils alone, one might object that paucity of marine fauna could also be found in a subtidal environment. But if all the evidence (fenestrae, laminations, paucity of fossils) is taken collectively it is highly probable that this facies is of intertidal (probably high intertidal) to supratidal origin.

4) Peloidal-Foraminiferal Wackestone Lithofacies (F4)

This facies is characterized by tan-brown wackestones and occasionally grainstones, locally dolomitic and becoming calcareous dolomite in well G41 and dolomite in its upper part of well F1. The allochems of this facies are predominantly foraminifers and peloids with common echinoderm fragments, rare gastropods and occasionally large bivalve fragments and ostracods. The forams are dominated by Miliolids but agglutinating forams and rotaliids are also present. The peloids present in this facies (Plate 2.4, A,B) are of two types; (1) small, ranging between 0.05-0.1 mm, and rounded or ovoid in shape: these are probably invertebrate fecal pellets, and (2) sand-sized grains with an average size of 0.34-0.85 mm, rounded to ellipsoidal in shape: these are too big to be fecal pellets as defined by Folk (1962). The term peloid, coined by Mckee and Gutschik (1969), is collectively used here as a purely descriptive term for both types.

Other sedimentary features such as stromatolites (Plate 2.4, C-F), are also present locally, particularly in the upper part of this facies, below the lower sulfate unit in well F1. Although, they appear to have been disrupted by the formation of sulfate, gypsum and anhydrite, their general morphology resembles the LLH (laterally linked hemispheroids) variety of Logan et al. (1964), which characteristically wrinkle into a series of small domes or hemispheroids linked laterally to each other (Logan, 1961). Pressure dissolution seams are developed locally and these are generally non-sutured and show pervasive horse-tail dissolution features. Abundant sulfates (mostly gypsum), are present through most of this facies both as a replacement of the original matrix and as a pore filling.

Interpretation

The presence of foraminifers and echinoderm fragments indicate a shallow marine environment and suggest that deposition was either in or close to essentially marine salinities. This may have been as a result of subsidence or a change in sea level that gave rise to the development of marine sediments above the dolomite mudstone lithofacies. Peloids are again important in shallow-marine sediments and are typical of shallow, low-energy, protected marine situations.

The presence of stromatolites is also an indicator of the depositional environment. In present day environments Mat growth is mostly precluded by the grazing activities of Cerithid gastropods. However, these gastropods cannot tolerate high salinities, so where these occur, small domal stromatolites form, in waters up to 3 meters deep (Tucker and

Wright, 1990). Recent stromatolites are essentially dominant in the shallow water realm and occur principally in supratidal, intertidal and shallow subtidal environments.

Logan et al (1964) classified stromatolites into three main types. These are, laterally linked hemispheroids (LLH), discrete, vertically stacked hemispheroids (SH), and discrete spheroids (SS). They concluded that modern stromatolites are features of intertidal or near intertidal zones and, based on their form arrangement, one can say that a certain arrangement is characteristic of a general intertidal location; protected intertidal, exposed intertidal, or agitated lower intertidal. For example, the LLH type are developed on protected intertidal mudflats, the SH type are developed on exposed intertidal headlands, and the SS type are developed in the agitated lower intertidal conditions. Kinsman and Park (1976) described small domal stromatolites formed in slightly more restricted reaches in the lower intertidal zones.

In the present rocks, stromatolites were affected by the formation and growth of sulfate minerals; gypsum and anhydrite, and only patches of small domal and laterally linked stromatolites are still preserved. This type of stromatolites, generally suggests, following Logan et al. (1964), protected intertidal settings. However, their association with calcium sulfates would indicate that they were probably formed in the upper intertidal to lower supratidal parts of the lagoon.

5) Evaporite Lithofacies (F5)

Beds of anhydrite (with gypsum), occur at three levels within the studied section. The lower two levels are represented by thin sulfate units and are mostly present in the western part of the area (e.g. wells E2 and F1), but a thin sulfate unit is also present in well G41 in the eastern area. The upper level is represented by a relatively thick and widespread unit, covering the whole area. The maximum thickness of these beds is approximately 3.0 meters whereas the thinnest beds are less than 1.0 meter thick. In all this lithofacies occupies 16% of the whole section and its upper contact is locally erosional (e.g. in well F1).

In general, the evaporite units of this facies exhibit several morphologies. These include thin interlaminations of anhydite-gypsum alternating with dolomite mudstone, centimetre size nodular masses (Plate 2.5, A-D), and also vertically oriented crystals growing upward from a depositional suface (Plate 2.5, E,F). Vertically oriented sulfate crystals are only observed in samples from the widespread sulfate unit (e.g. in well G4). The anhydrite nodules are partly enclosed by dark brown dolomite mudstones forming a texture which resembles the familiar "chickenwire" texture. They are composed, as seen in thin-sections, of masses of lath-shaped elongated crystals, up to 1.0 mm in length, and arranged as clusters in which the crystals diverge into radiating sprays or may form bundles with crystals stacked subparallel to one another and locally enclosing patches of dolomite mudstone (Plate 2.6).

Interpretation

Evaporites, gypsum and its dehydrated form anhydrite are relatively common in marine rocks of various ages, especially Paleozoic and younger deposits. In general, the origin of these sulfate minerals is attributed to some form of evaporation process and nearly all authors discussing their origin suggest an arid to semiarid climate and high evaporation rates (Watson,1985; Bain,1990). In addition, if evaporites are to form, some type of circulation restriction must prevent marine water, concentrated by evaporation, from returning to the open sea and remixing (Peterson and Hite, 1969).

Thinly interlaminated and interbedded sulfate and nodular sulfate, generally forms through the evaporation of extremely shallow water on extensive tidal flats. Examples of vertically oriented gypsum crystals from the Miocene gypsum of the Mediterranean (Hardie & Eugster, 1971; Schreiber et al, 1982) have been interpreted as forming in shallow, hypersaline waters by the mechanism of competitive growth from a depositional surface. Studies of modern gypsum deposition support this interpretation (Schreiber & Kinsman, 1975; Schreiber and Schreiber, 1977). The hypersaline lagoon interpretation confines the precipitation of the primary gypsum to a lagoon in which the deposition of carbonate sediment was reduced due to gradually increasing restriction and concomitant elevation of salinity. The crystals of gypsum then grew on the floor of the lagoon when the waters reached gypsum saturation. In this study, the sulfates were probably precipitated in a shallow hypersaline lagoon. In this the lower sulfate units associated with peritidal deposits represent the supratidal landward area of the lagoon, while the widespread sulfate unit at

at the top of the succession, was probably precipitated as the lagoon as a whole became more restricted and isolated and consequently the water became hypersaline and eventually reached gypsum saturation.

6) Argillaceous Dolomite Mudstone Lithofacies (F6)

This facies is represented by argillaceous dark grey mudstones and dolomite mudstones interbedded with thin streaks, approximately 0.5 m thick, of calcareous, pyritic and subfissile shales. The dolomites of this facies are generally very finely to finely crystalline with scattered pyrite crystals and very rare forams, ostracods and echinoderm fragments. The facies overlies an irregular surface on facies 5 in well F1 and on facies 3 in well D2 (Plate 2.7, A,B). EDX analysis of samples of this facies shows the samples consisting of Ca and Mg with Si, Al, K and Fe, which represent the clay present in this facies. The flaky and filamentous morphology shown in the photomicrographs (Plate 2.7, C,D) supported by the EDX spectra (Fig. 2.1) suggest that the clay minerals present are illite-smectite.

Interpretation

This facies is laterally extensive and readily correlatable throughout the study area. In general this facies was deposited in a relatively deep marine environment and reflects a rapid change in the conditions of deposition. The irregular surface between this facies and the underlying facies 5 of well F1 and facies 3 of well D2, indicates subaerial exposure and a period of erosion followed by a marine incursion covering the whole area.

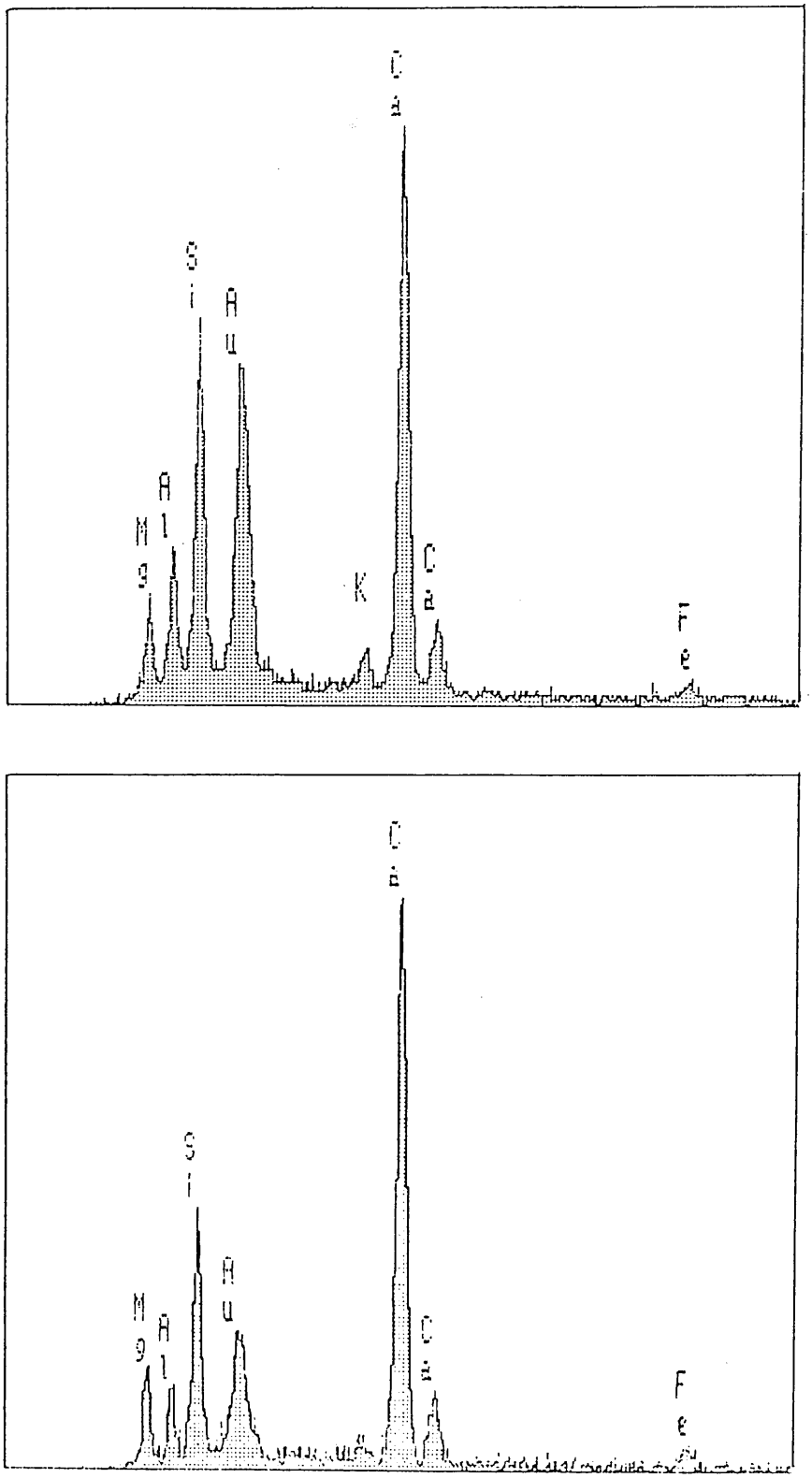

Fig. 2.1, EDX analysis of the clayey sediments of facies 6. Upper spectrum is from the analysis of the clay sediment shown in PLate 2.7, C and the lower spectrum is from the analysis of the clay sediment shown in PLate 2.7, D.

2.3 Lithofacies Sequences

In attempting to construct a depositional model for this part of the Beda Formation, it is necessary to know the associations of the different lithofacies. Their association, specifically the vertical succession in which they are ordered, is far more diagnostic than individual lithofacies. In this study the vertical association of the different lithofacies has revealed a sequence of sediments which can be related to three small-scale shallowing-upward cycles, ranging from 8 to 12 meters in thickness and spread over the study area. Stratigraphic cross-sections (Figs. 2.2, 2.3) were constructed to show the vertical sequence as well as the lateral distribution of these cycles.

A lithofacies relationship diagram (Fig. 2.4) was constructed to show the number of times the different lithofacies are in vertical contact with each other. This simple visual method was used by de Raaf, Reading and Walker (1965). From the model, it is clear that an idealized section contains facies 1 to 5 which represent an accreting sequence from deeper marine to lagoonal through intertidal to supratidal sediments. This model provides a useful generalization. However, in the sequences studied, the succession begins in the lagoonal part of a cycle and ends with a new marine transgression. Three cycles are represented, but these are not all complete.

The first cycle begins with foraminiferal wackestone lithofacies (F1) overlain by reduced grey subtidal deposits of the argillaceous foraminiferal wackestone lithofacies (F2). The shallower portion of this cycle is the dolomite mudstone lithofacies (F3). The basal unit of the overlying cycle (cycle 2) is represented by peloidal-foraminiferal wackestone lithofacies (F4), and the shallower part, over most of the study area (e.g. wells D2 and G41),

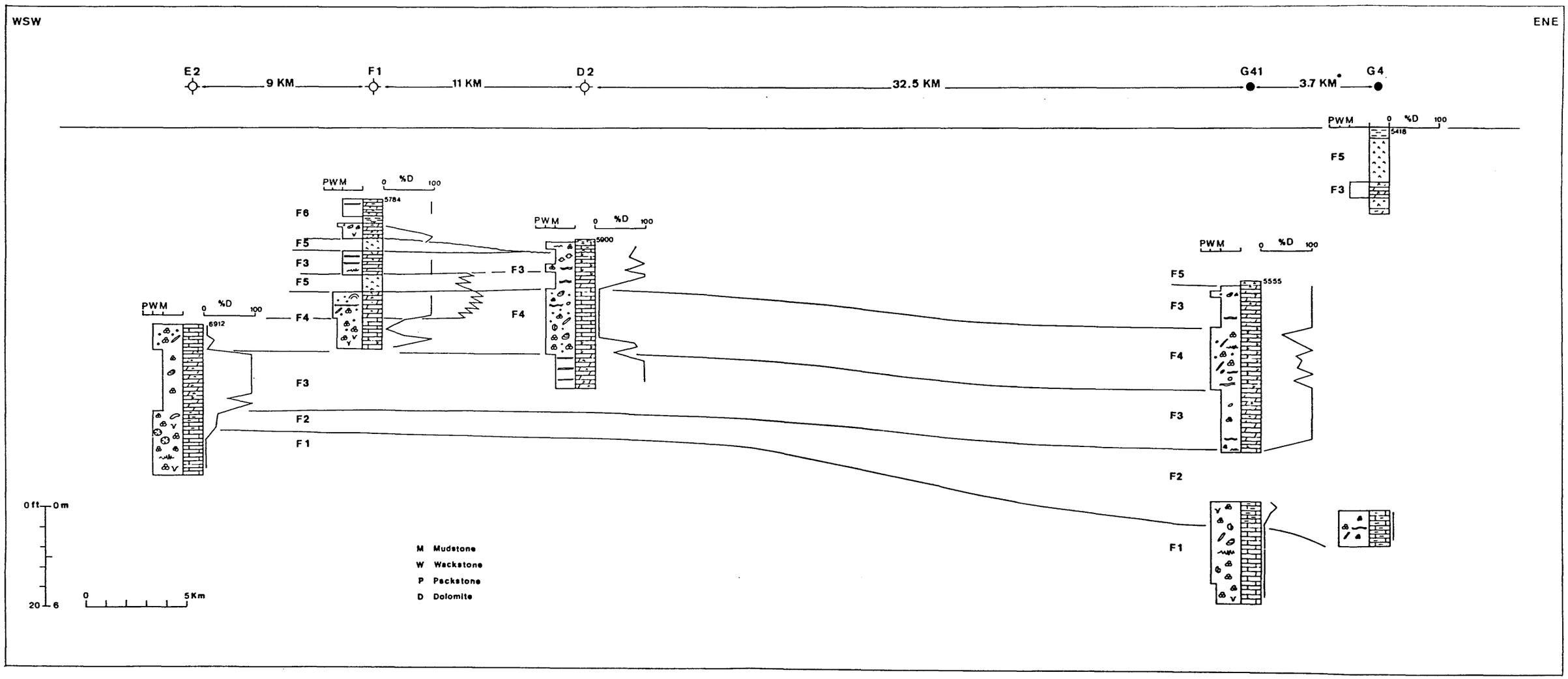

Fig. 2.2, Stratigraphic core section, showing the different lithofacies as recognized from the studied part of the Beda Formation. (*) distance between wells G41 and G4 is not to scale.

Fig. 2.2, Continued.

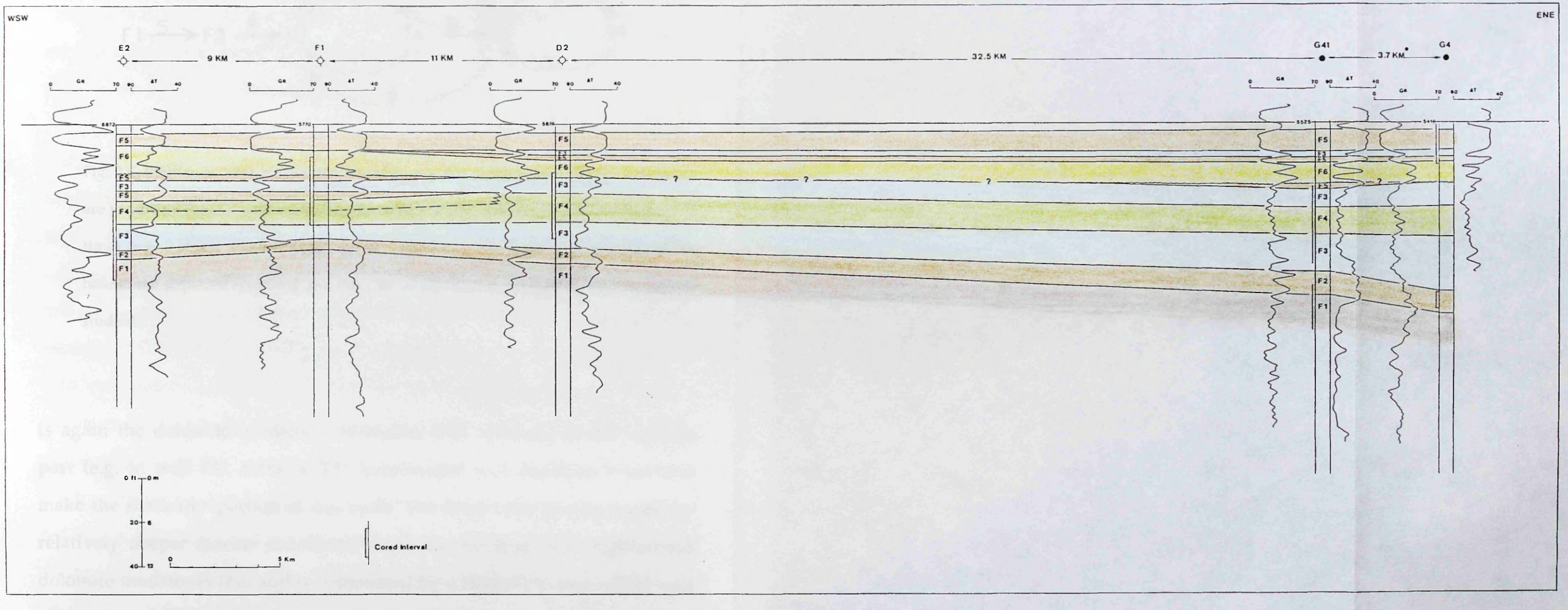

Fig. 2.3, Stratigraphic log section (GR and Sonic logs), showing the lithofacies sequences and their lateral distribution across the study area. (*) distance between wells G41 and G4 is not to scale.

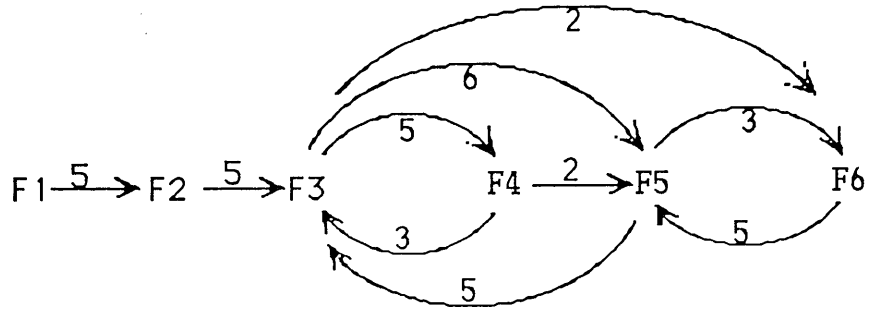

Fig. 2.4, lithofacies relationship diagram showing the number of times the lithofacies are in vertical contact with each other. Numbers on the arrows indicate the number of times (e.g. 5 means the lithofacies are in contact five times). Note F1 represents the base of the sequence examined and this part of the cycle is not repeated in the interval studied.

is again the dolomite mudstone lithofacies (F3), whereas, in the western part (e.g. in well F1), sulfates (F5) interbedded with dolomite mudstone make the shallower portion of this cycle. The third cycle is represented by relatively deeper marine sediments, shales interbedded with argillaceous dolomite mudstones (F6) and is culminated by a laterally extent sulfate unit of the evaporite facies (F5).

Considerable attention has been devoted to shallowing-upward sequences deposited on carbonate shelves and platforms (e.g. Laporte,1967; Ginsburg,1975; Wilson,1975; Enos,1983; Hardie,1986a,b etc.). Small-scale shallowing-upward cycles are common in carbonate sediments. The two main types of sedimentary explanation are currently in vogue for shallowing-upward cycles, generally taken as acting against a background of

continuous subsidence and/or sea-level rise. The first is the autocyclic model of R. N. Ginsburg (e.g. reviewed in Hardie,1986b) and the second is the tidal island model of Pratt and James (1986). The other depositional process that leads to the formation of shallowing-upward cycles is the vertical accretion of subtidal sediments into shallow depths which can take place when sediment production rates are high.

The first model calls on continuous steady basinal subsidence coupled with carbonate sediment supply rates that are self-regulated by the extent of progradation. The basic point of the model lies in the recognition that the carbonate sediment production rate will fall behind the subsidence rate as progradation drastically reduces the size of the subtidal carbonate factory until the sediment supply is choked off over the entire platform. With renewed subsidence, a new cycle begins as the subtidal area once again becomes deep enough to re-establish the subtidal carbonate factory and allow efficient carbonate production. This factor introduces an automatic lag time in deposition so that subtidal sediments lie directly on supratidal sediments. The time scale for cycle generation predicted by this model is of the order of tens of thousands to a few hundred thousand years, depending on the size of the platform and the rates of subsidence and progradation.

In the tidal island model, the platform is never completely exposed or submerged, but is dotted with tidal islands which accrete and migrate laterally with time at variable rates, but keeping pace with sea level rising through eustacy or subsidence. The rate of accretion of each island will inherently decrease once the depositional surface has reached the supratidal zone. Lateral progradation of these islands will take place until it is prevented when neighbouring sediment-generating subtidal regions have

been reduced in area and consequently, the supply of sediments to maintain island growth ceases. Hydrographic forces will then shift the site of sediment accretion to a nearby area. After the former area subsides below sea-level, the focus of sedimentation shifts back again to this area and another cycle is deposited above the underlying one.

Although shallowing-upward sequences are the typical product in both models, it is difficult to relate either to this part of the Beda Formation. The main evidence for the tidal island model is the lateral impersistence of facies and the cycles produced are of local rather than regional extent. It is equally difficult to equate the shallowing-upward cycles of the Beda Formation with the autocyclic model of Ginsburg because of the formation of laterally extentive sulfate units above the deeper marine sediments of the third cycle. This rapid change indicates some change in the depositional setting, rather than the typical development of shallowing-upward cycles, proposed by the model.

2.4 **Depositional Model**

On the basis of faunal content and sedimentary features, the sediments examined can be interpreted as the products of deposition in a shallow shelf-lagoon, dominated by intertidal to supratidal sediments. Some parts of this must have been relatively open while others were clearly restricted. The sequence of how the shallowing-upward units were produced is illustrated in figure 2.5, and will be discussed.

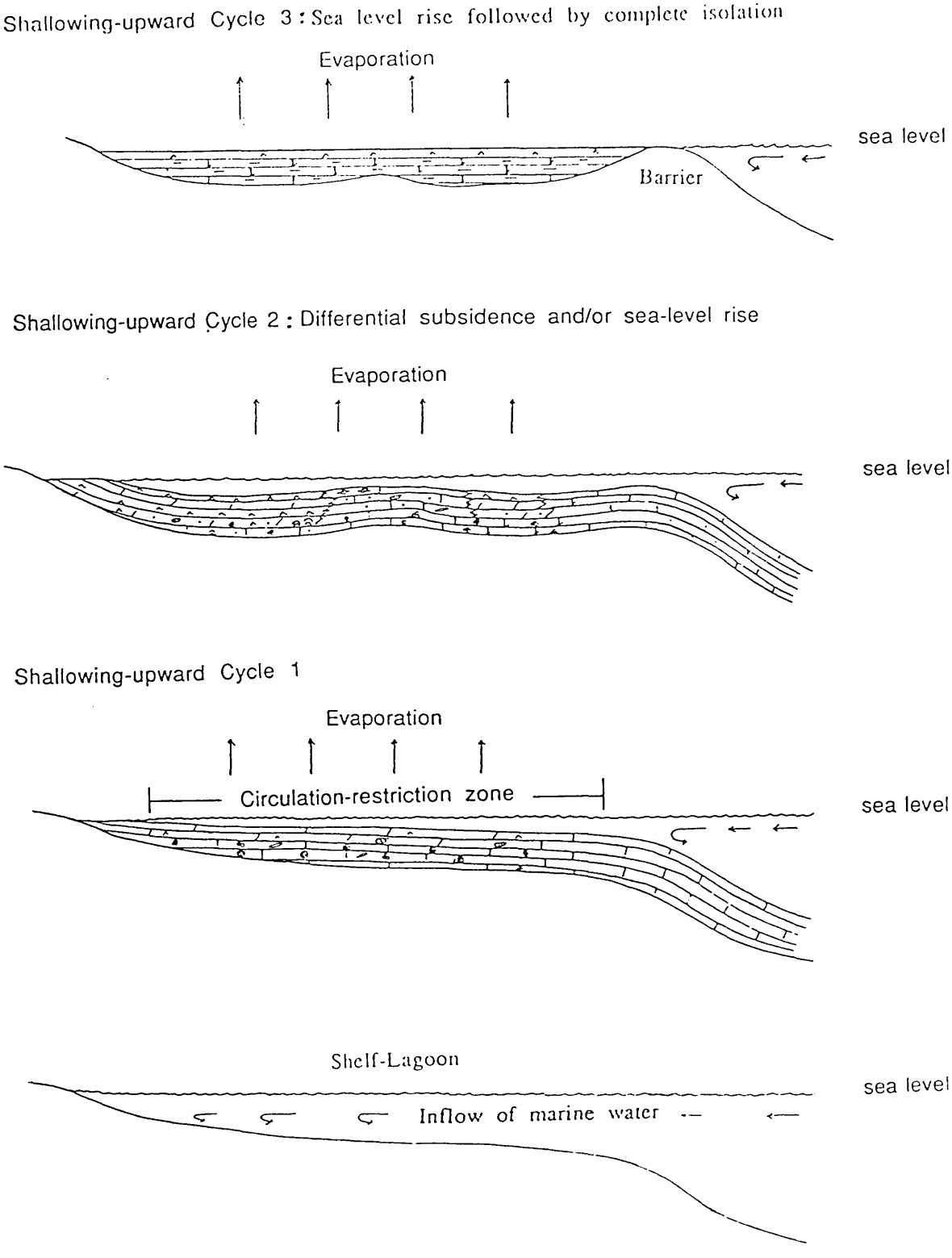

Fig. 2.5, WSW-ENE schematic cross-section, illustarting the depositional model of the three shallowing-upward cycles of the Beda Formation.

The basal unit of the first cycle was probably deposited on a wide, shallow shelf. The water may have been less than 10 meters deep, but it allowed free water circulation across the shelf-lagoon and provided a suitable environment for a benthonic marine fauna and flora to flourish. Since shallow water carbonate sedimentation is an extremely rapid process, a regressive outbuilding occurred and consequently, the water became much shallower. This shallowness was sufficient in itself to restrict water circulation and to promote the lower hydraulic energy conditions necessary for lime mud accumulation above the shallow marine deposits. As a result of circulation-restriction, salinity increased in the near shore zones due to evaporation and this led to the precipitation of calcium sulfates (Irwin,1965) and consequently extensive dolomitization of the lime mud.

The onset of the second cycle is also represented by shallow water lime wackestones, reflecting an increase in the depth of water following, probably, a relative rise in sea level and/or a relative subsidence of the shelf-lagoon. The depth of water became sufficient for faunal growth and the area was probably more protected than it was during the deposition of the lower cycle. As in the lower cycle, this basal unit of shallow marine deposits is overlain by extensively dolomitized lime mudstone and by calcium sulfates as regressive outbuilding of the sediments occurred. The precipitation of sulfate units above the shallow marine sediments in the western portion of the study area (e.g. wells E2 and F1), where peloids (including faecal pellets) and stromatolites are present, indicates slightly more protected and restricted reaches, probably in landward areas of the lagoon, while the relative absence of sulfates and absence of peritidal deposits to the east suggest slightly deeper areas within the lagoon,

reflecting differential subsidence and/or differential accumulation of sediments which resulted in lagoon surface irregularities.

The third cycle of this interval reflects an incursion of the sea which flooded the shelf-lagoon following some period of subaerial exposure and evaporation. Dark grey lime mudstones and shales were deposited throughout the area and were capped by a laterally extensive sulfate unit. This widespread evaporite is clearly different from those in the two cycles below. The rapid change from deeper marine sediments into evaporite implies some type of barrier development which was high enough to check any free water circulation into the lagoon. The rapid development of this circulation-restricting barrier led to a general salinity increase and consequently, to the formation of a shelf-wide evaporite lagoon.

Plate 2.1

A) Slabbed core sample of facies 1 showing abundant fossil fragments. Scale bar = 2 cm.

B-E) Photomicrographs of this facies show foraminifera (B), dasycladacean algae (C), foraminifera and algae (D), and rare peloids cemented by calcite (arrow, in E). Scale bar = 1 mm. PPL.

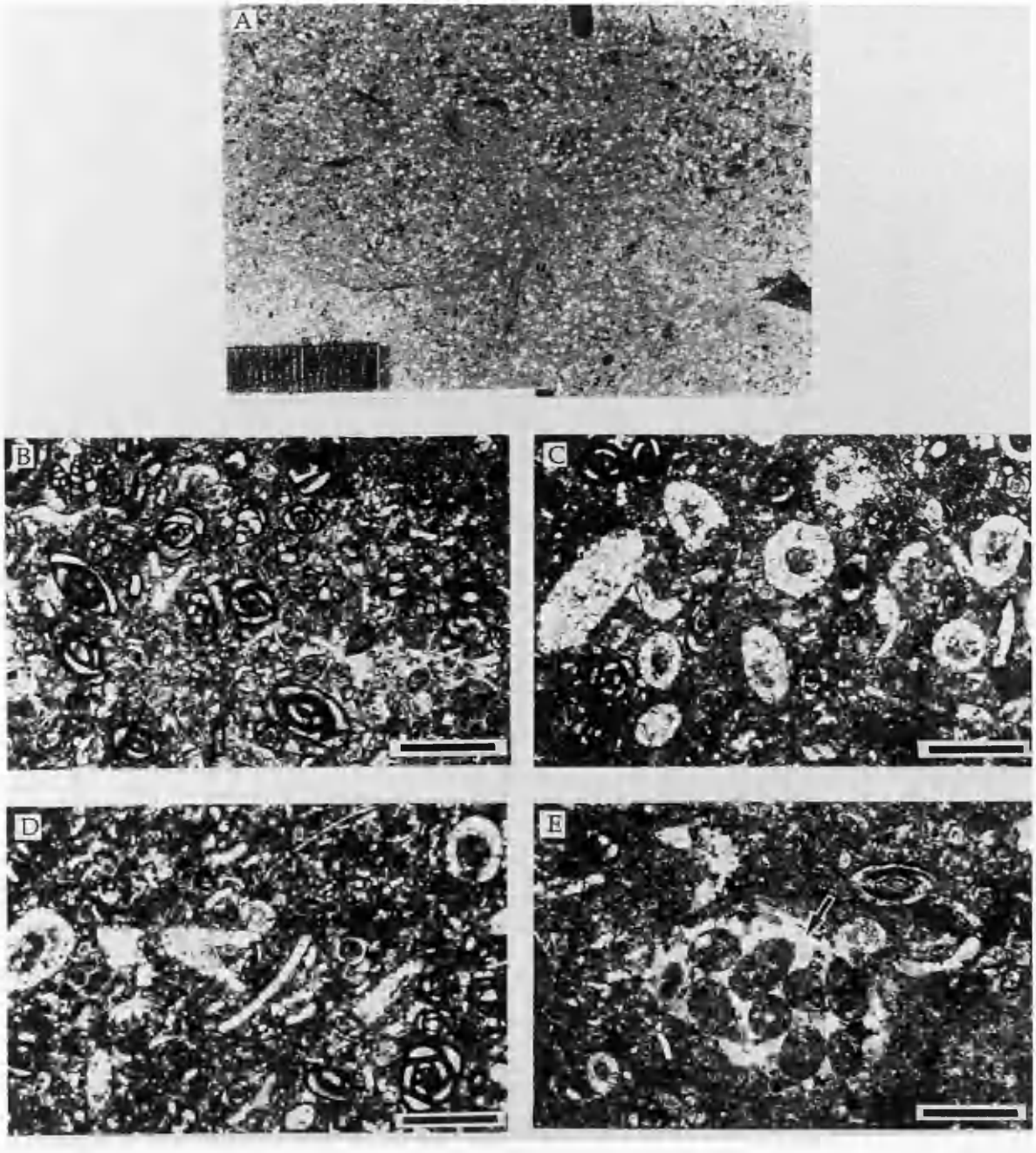
A
B
C
D
E

Palte 2.2

A) Slabbed core sample of facies 2 showing centimeter-scale clasts (a) surrounded by dark brown mud(b). Scale bar = 2 cm.

B) Slabbed core sample showing the argillaceous nature and mottled structure of this facies. Scale bar = 2 cm.

C,D) Photomicrographs showing rotaliids foraminifera (a), and dissolution seams (arrow). Scale bar = 1 mm. PPL.

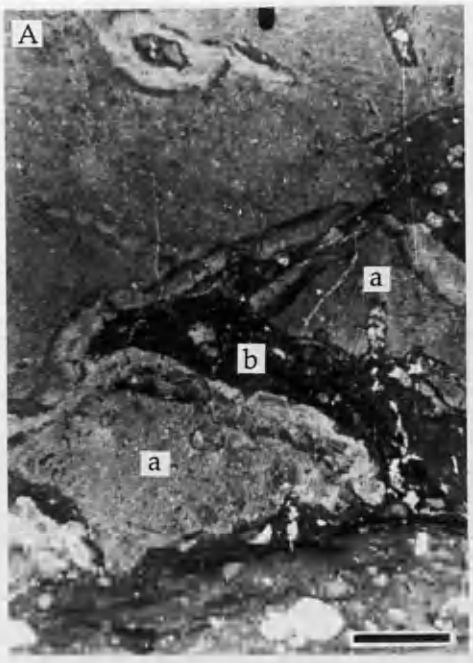
A
a
b
a


B
C-3-2

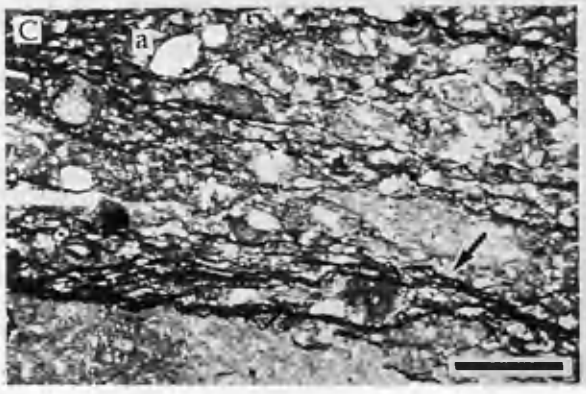
C
a

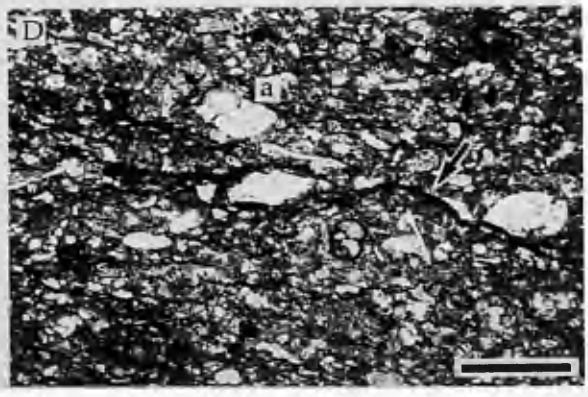
D
a

Plate 2.3

A,B) Slabbed core samples of facies 3 showing finely laminated dolomite. A) Scale bar = 2 cm. B) Scale bar = 1 cm.

C, D) Photomicrographs showing scattered rip-up clasts (arrow). Scale bar = 1 mm. PPL.

E,F) Slabbed core samples showing fenestral structure. The fenestrae are filled with sulfates and calcite cements. Scale bar = 2 cm.

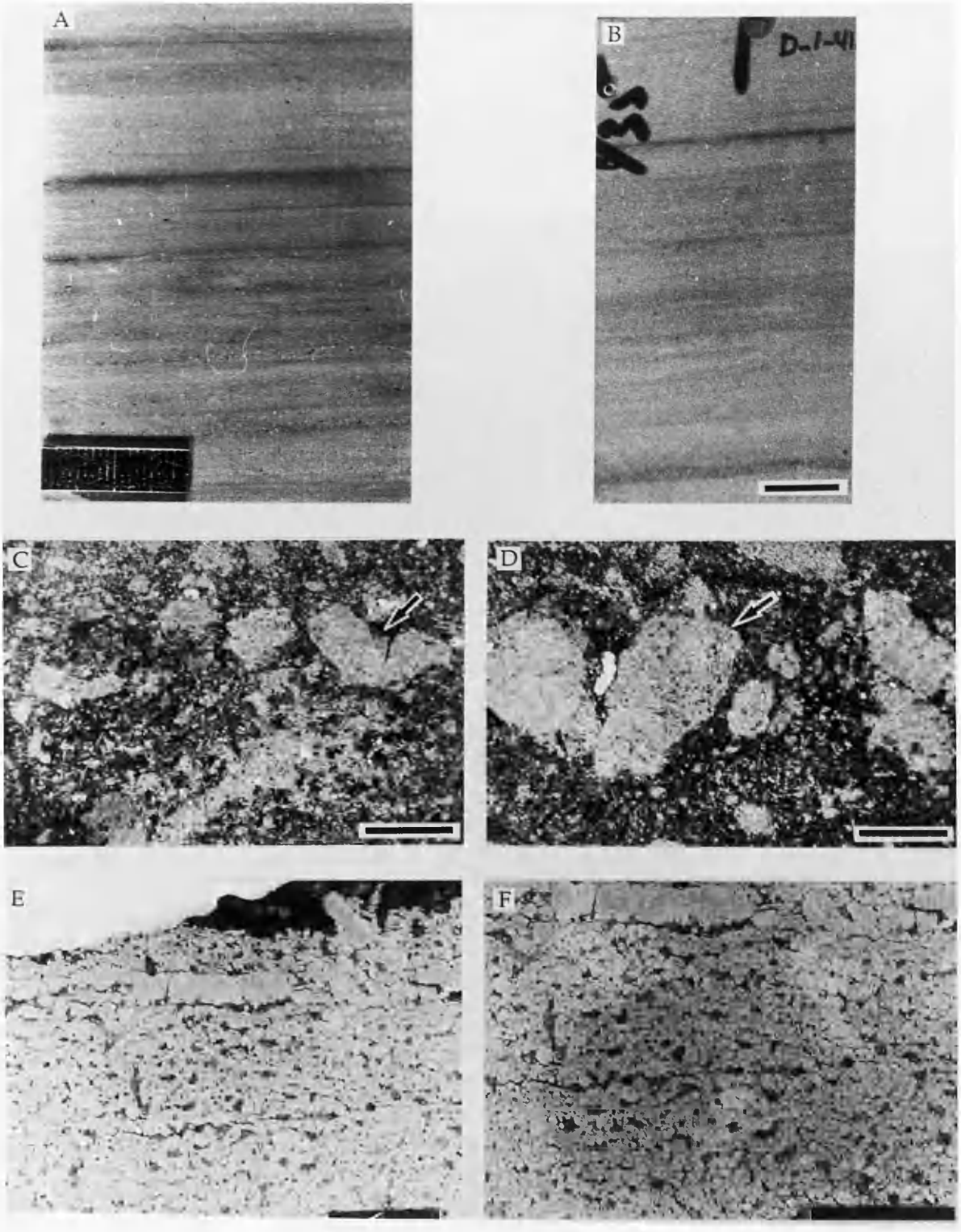
A
B
D-1-41
C
D
E
F

Plate 2.4

A,B) Photomicrographs of peloids of facies 4 showing the different sizes of peloids. A) Shows sand size pellets. B) Shows smaller size (or fecal) pellets (arrow). Scale bar = 1 mm. XPL.

C) Slabbed core sample of this facies showing domes (arrows) of laterally linked hemispheroids. Scale bar = 1 cm.

D-F) Photomicrographs of these stromatolites showing sulfates (white areas in the photograph) deposited within and between domes. Scale bar = 1 mm. PPL.

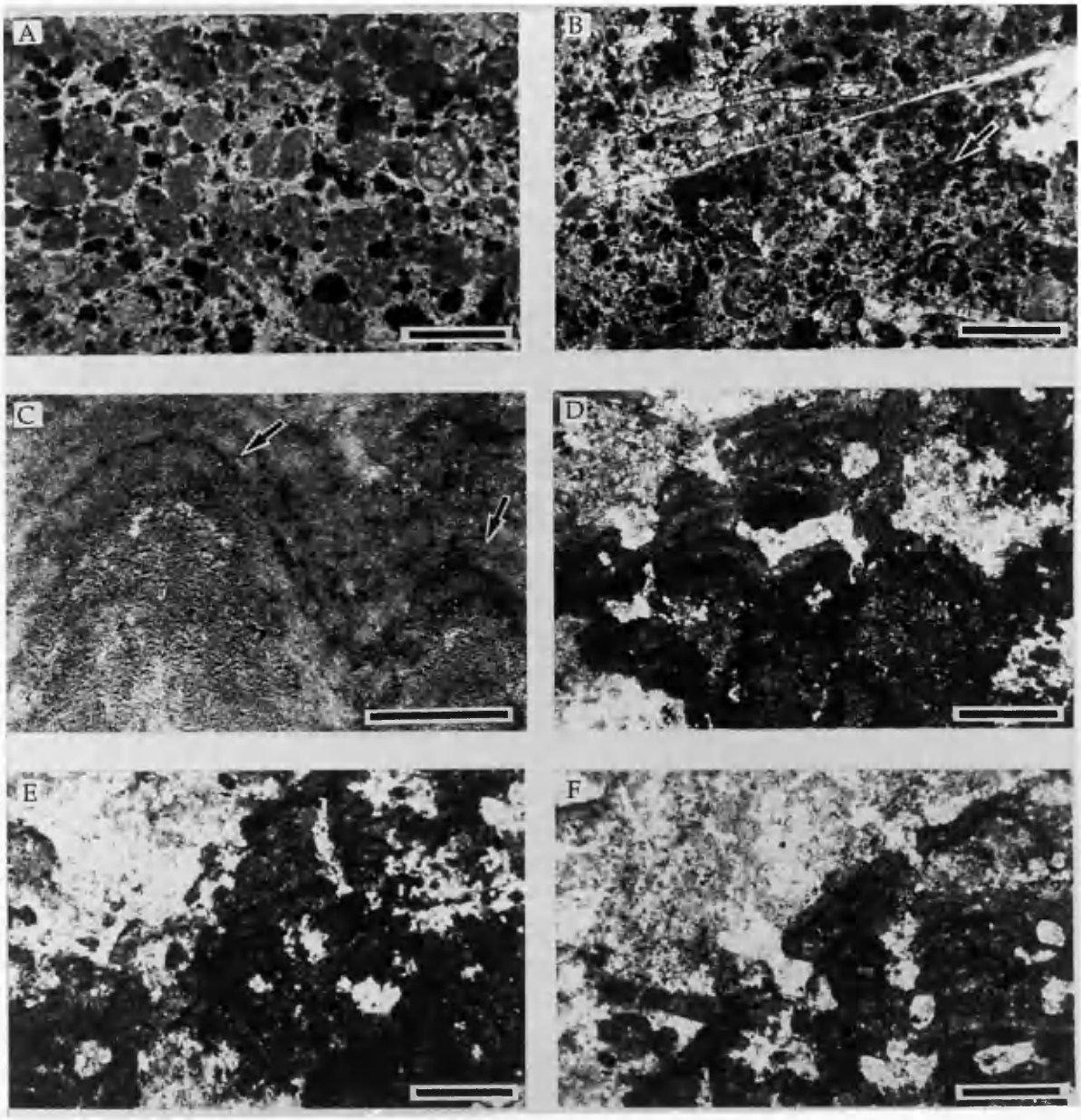
A
B
C
D
E
F

Plate 2.5

A-D) Slabbed core samples of facies 5, showing the nodular form of this evaporite facies. The nodules are partly enclosed by dark brown surfaces of dolomite mudstone. Scale bar = 2 cm.

E,F) Slabbed core samples showing vertically oriented sulfate crystals (arrow) growing on a dark brown surface of dolomite mudstone. Scale bar = 2 cm.

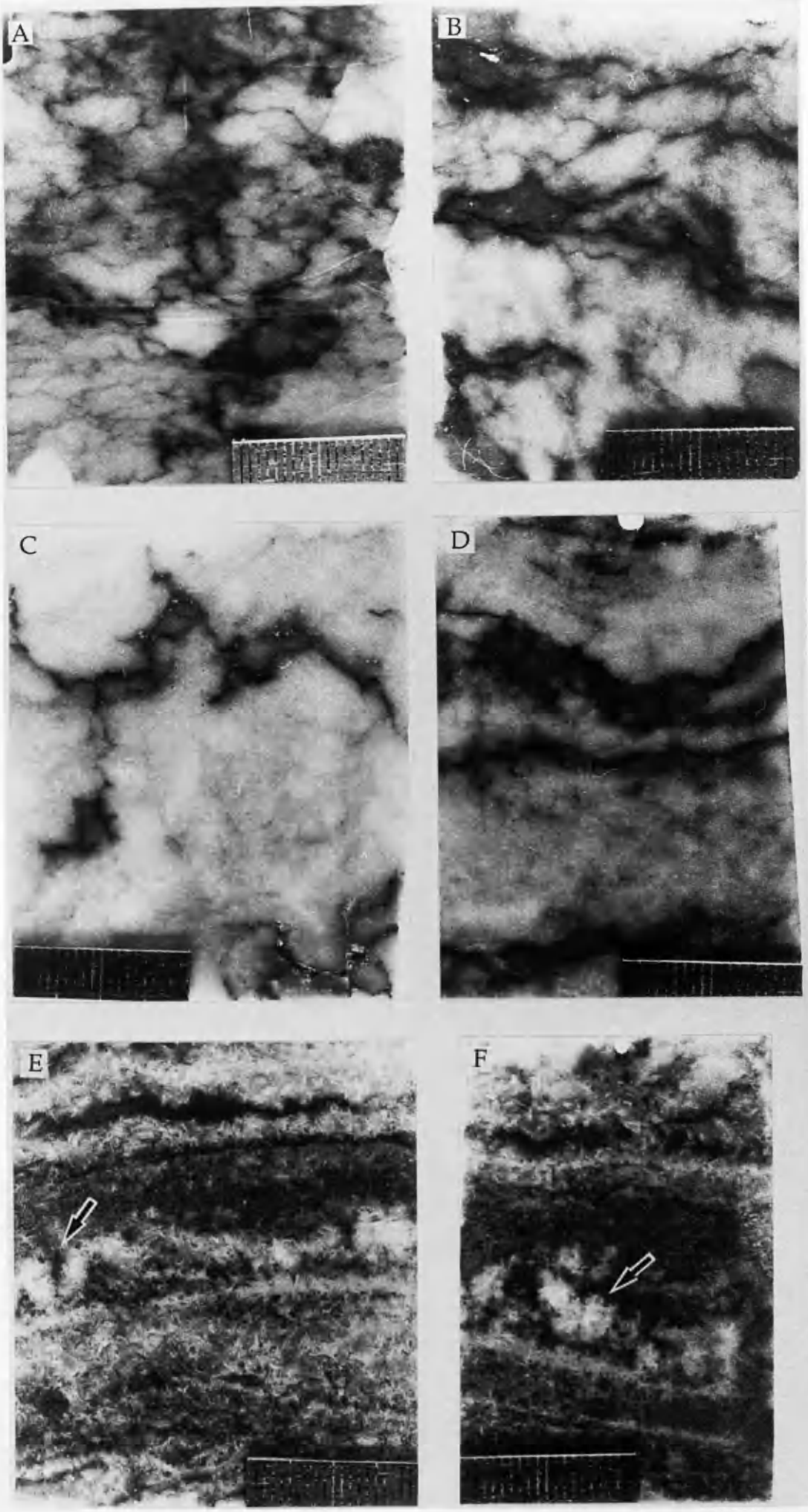
A
B
C
D
E
F

Plate 2.6

A,B) Photomicrographs of facies 5 showing elongated laths of crystals of gypsum and anhydrite. Scale bar = 0.2 mm. XPL.

C,D) Photomicrographs showing gypsum and anhydrite with thin streaks and patches of dolomite (a). C) Scale bar = 1 mm. D) Scale bar = 0.2 mm. XPL.

E,F) Photomicrographs showing rosettes of anhydrite. Scale bar = 1 mm. XPL.

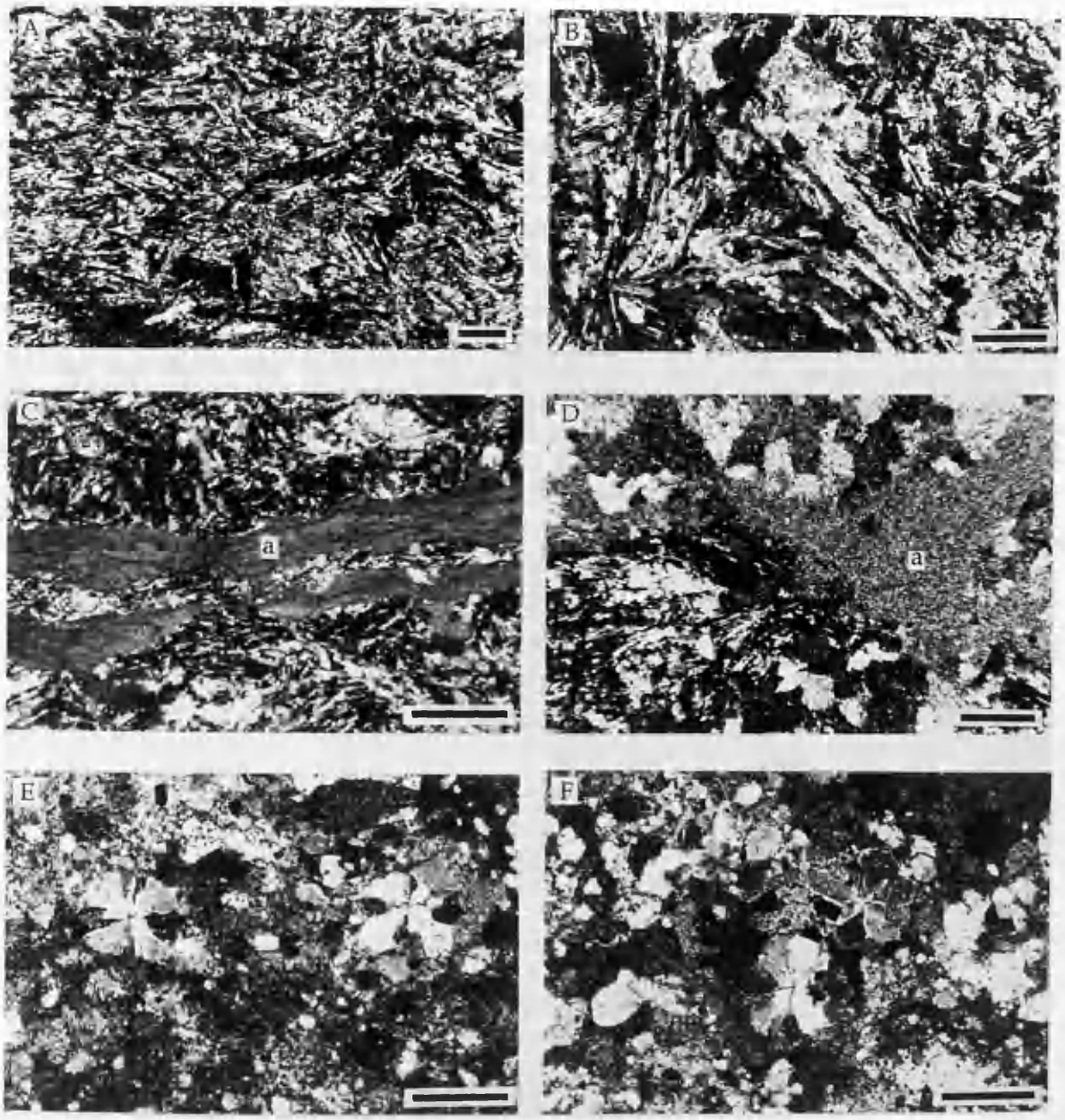
A
B
C
a
D
a
E
F

Plate 2.7

A,B) Slabbed core samples of facies 6 showing the argillaceous nature of this facies (a). They also show the erosional surface (arrow) between this facies and the underlying facies 5 in well F1 (A) and facies 3 in well D2 (B). Scale bar = 2 cm.

C,D) SEM-photomicrographs showing the filamentous and flaky morphology of the clay of this facies.

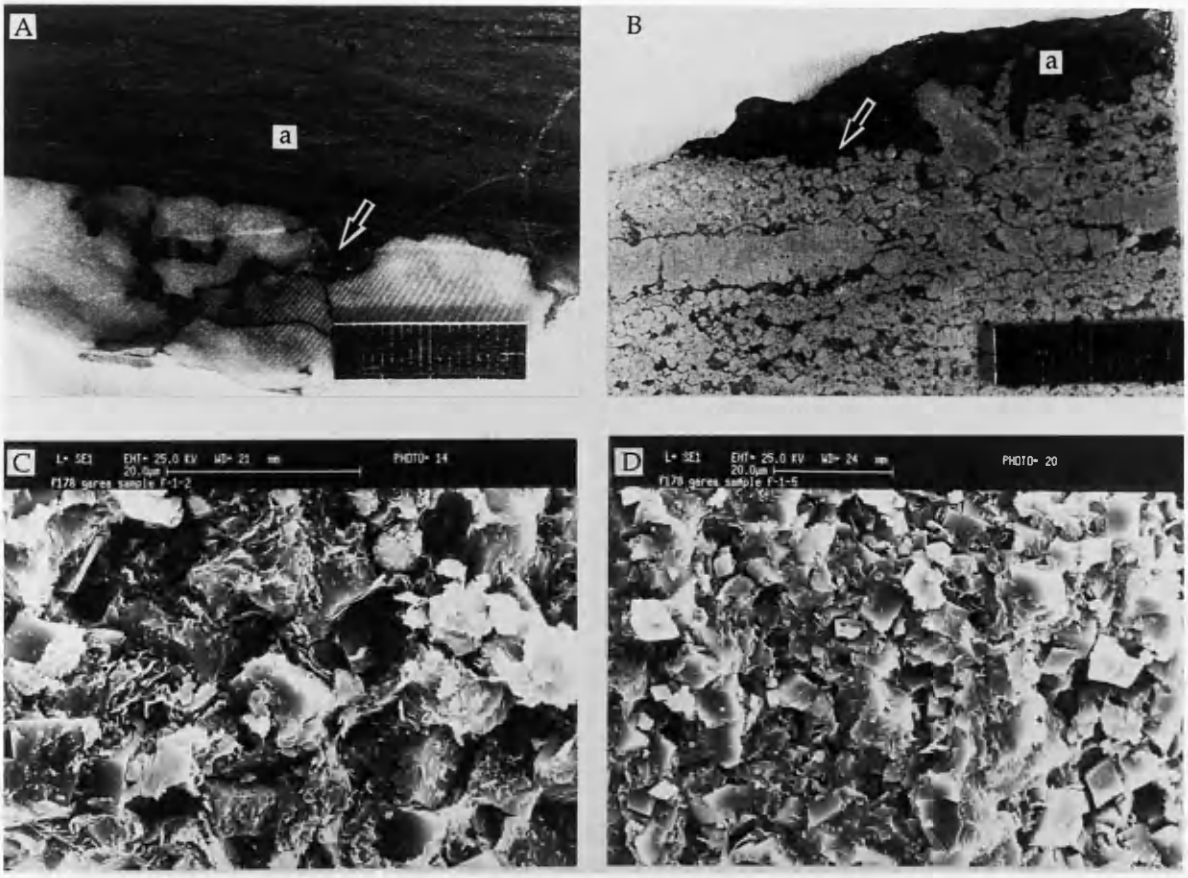
A
a
B
a
C
L= SE1 EHT= 25.0 KV WD= 21 mm
20.0µm
PHOTO= 14
F178 gares sample F-1-2
D
L= SE1 EHT= 25.0 KV WD= 24 mm
20.0µm
PHOTO= 20
F178 gares sample F-1-5

CHAPTER THREE

GEOCHEMISTRY

This chapter summarizes the results of the geochemical investigations carried out on the sediments of the Beda Formation for this study. These include, the analyses of the elemental and compound composition and concentrations, and the analyses of carbon, oxygen, and sulfur isotopes of these sediments. Carbonate samples were analyzed by X-ray diffraction (discussed in Chapter 2) for calcite and dolomite contents. More than 70 samples were prepared to determine the trace element contents, and about 40 of these samples, mostly those from the dolomite intervals, were prepared to determine the major and minor compounds (oxides) of the sediments. Stable isotope analyses of carbon and oxygen isotopes, and sulfur isotopes were also made on 16 dolomite samples and 10 calcium sulfate samples, respectively.

The aim of this geochemical investigation was to determine the bulk composition of the Beda sediments, and to obtain some information, using the abundance of trace elements like stronium, iron and manganese, on the origin of the dolomitizing fluid and the constraints on the dolomitization model for this formation. The stable isotope analyses of $\delta^{13}C$ and $\delta^{18}O$ were also used to determine the conditions of the origin of this dolomite and the source of the dolomitizing fluids, and to attempt to discriminate between dolomites. This, was necessary because some dolomites are seen to be related to probable downward movement of evaporite-derived waters (derived from the overlying evaporite sulfate units) whereas others show

no comparable pattern. The purpose of stable isotopic analyses of sulfur $\delta^{34}S$ was to obtain information on the evaporite units.

3.1 Methods and Technique

3.1.1 X-Ray Fluorescence (XRFS) Analyses

A total of 16 trace elements (i.e. Zr, Y, Sr, Rb, etc.) and 10 major oxides (i.e. SiO_2, Al_2O_3, MgO, CaO, Fe_2O_3, MnO, etc.) were determined using a Phillips PW 1450/20 sequential automatic X-ray spectrometer, following the technique described by Leake et al. (1969). This method was chosen in preference to microprobe analysis becaused optical examination suggested a general chemical uniformity. The detection limits are generally low, .165% for MgO, .006% for CaO, .045% for Fe_2O_3, .012% for MnO, and 1.5 ppm for Sr. However, the accuracy of the results is generally dependent upon the accuracy of calibrations used and the effect of mineralogical variations within the samples analysed. The analyses of major oxides were performed on fused glass beads made of 0.375 g of 100 mesh rock powder and 2.0 g of spectroflux (Lithium tetraborate). For precision, the beads were prepared in duplicate. The trace element analyses were performed on pressed pellets, made of 6.0 g of 250 mesh rock powder and 1.0 g of thermal binder (phenol formaldehyde). All major oxides are reported in weight percent (wt.%), whereas, the trace element data are reported in parts per million (ppm). The elemental and compound compositions and concentrations obtained are given in Tables 3.1-3.4.

	E-1-2 6912'	E-1-3 6913'	E-1-6 6914'	E-1-9 6916'	E-1-12 6918'	E-1-16 6921'	E-1-22 6925'	E-1-25 6926'	E-1-27 6928'	E-1-29 6929'
Y	4	b.d.l.	4	b.d.l.	1	b.d.l.	b.d.l.	3	b.d.1.	4
Sr	1079	14292	587	34846	5488	38212	22275	4903	20514	7000
U	3	b.d.l.	9	b.d.l.	b.d.l.	b.d.l.	b.d.l.	b.d.l.	b.d.l.	b.d.l.
Rb	3	b.d.l.	6	b.d.l.	3	b.d.l.	b.d.l.	5	b.d.l.	4
Th	3	2	5	b.d.l.	0	b.d.l.	b.d.l.	3	b.d.l.	7
Pb	b.d.l.	1	b.d.l.	b.d.l.	b.d.l.	b.d.l.	b.d.l.	b.d.l.	b.d.l.	b.d.l.
Ga	1	20	2	76	7	117	45	5	40	8
Zn	2	2	0	15	2	43	8	5	6	3
Cu	0	29	b.d.l.	114	5	162	67	4	58	8
Ni	b.d.l.	3	0	25	4	33	14	0	11	3
Co	b.d.l.	b.d.l.	2	b.d.l.	1	0	b.d.l.	b.d.l.	1	b.d.l.
Cr	1	1	3	8	b.d.l.	7	7	17	14	8
Ce	8	58	2	251	21	373	142	23	120	35
Ba	86	0	24	b.d.l.	45	23	3	25	b.d.l.	b.d.l.
La	b.d.l.	b.d.l.	b.d.l.	b.d.l	b.d.l.	b.d.l.	b.d.l.	b.d.l.	b.d.l.	b.d.l.

	E-1-32 6931'	E-1-34 6933'	E-1-37 6935'	E-1-39 6936'	E-1-40 6937'	E-1-43 6940'	E-1-45 6942'
Y	8	5	2	6	3	4	4
Sr	476	428	5809	303	286	344	225
U	3	7	b.d.l.	8	4	5	6
Rb	9	16	2	3	4	3	3
Th	7	10	5	8	6	7	5
Pb	1	3	b.d.l.	1	2	5	1
Ga	3	2	6	0	1	b.d.l.	0
Zn	11	4	0	b.d.l.	1	2	2
Cu	2	b.d.l.	8	b.d.l.	0	0	b.d.l.
Ni	4	7	b.d.l.	1	2	0	b.d.l.
Co	0	1	0	0	1	1	b.d.l.
Cr	20	26	3	2	4	2	2
Ce	8	12	20	0	0	b.d.l.	2
Ba	15	6	6	22	8	52	50
La	5	6	b.d.l.	3	6	b.d.l.	1

	E-1-3 6913'	E-1-9 6916'	E-1-12 6918'	E-1-16 6921'	E-1-27 6928'	E-1-29 6929'	E-1-34 6933'	E-1-39 6936'	E-1-45 6942'
SiO2	-	-	-	-	1.06	1.14	4.68	-	-
TiO2	.02	.01	.01	.01	.45	.04	.09	.01	.02
Al2O3	.21	.34	.22	.25	1.09	1.0	2.51	.24	.29
Fe (tot)	.09	.19	.06	.24	.60	.38	.85	.04	.24
MnO	.02	.01	-	.01	.07	.02	.02	.04	.06
MgO	.83	15.85	8.49	17.56	17.36	8.51	2.01	.95	12.78
CaO	53.70	24.50	44.64	23.65	29.47	43.27	48.87	54.92	39.30
Na2O	.23	.12	.40	.17	.11	.04	.04	.16	-
K2O	.04	.05	.06	.04	.15	.16	.44	.05	.05
P2O5	.01	.01	.01	.01	.01	.01	.02	.01	.01
$CO2_{cal}$	43.05	36.53	44.30	37.73	42.08	43.25	40.32	44.14	44.79
Total	98.20	77.61	98.19	79.67	92.45	97.82	99.85	100.56	97.54

Table 3.1, the chemical analyses of the Beda sediments measured from the cored interval of well E2. (b.d.l) below detection limit. (-) values are less than zero on the calibration chart. Equations for CO_2 calculation are listed in Appendix B.

	F-1-2 5785'	F-1-3 5786'	F-1-5 5787'	F-1-8 5789'	F-1-9 5790'	F-1-12 5792'	F-1-16 5795'	F-1-18 5798'	F-1-21 5803'	F-1-24 5804'
Y	10	6	5	6	6	7	0	4	b.d.l.	5
Sr	720	1309	7130	931	1368	732	9071	226	69978	485
U	3	1	b.d.l.	2	2	4	b.d.l.	5	b.d.l.	4
Rb	20	3	10	2	10	10	b.d.l.	2	b.d.l.	b.d.l.
Th	1	0	10	b.d.l.	1	9	b.d.l.	1	b.d.l.	8
Pb	2	3	2	1	4	2	2	3	b.d.l.	0
Ga	6	1	12	0	4	4	11	0	353	b.d.l.
Zn	17	35	78	1	14	40	9	9	76	6
Cu	6	3	11	5	1	3	30	b.d.l.	861	b.d.l.
Ni	7	1	6	b.d.l.	4	1	4	b.d.l.	111	b.d.l.
Co	3	0	4	b.d.l.	1	2	b.d.l.	0	b.d.l.	b.d.l.
Cr	30	5	26	2	24	20	2	7	28	2
Ce	24	15	50	15	19	16	36	6	1016	3
Ba	37	7	41	10	27	13	30	28	155	10
La	12	3	5	b.d.l.	7	12	b.d.l.	b.d.l.	b.d.l.	b.d.l.

	F-1-27 5806'	F-1-30 5808'	F-1-32 5809'	F-1-35 5811'	F-1-38 5813'	F-1-40 5814'
Y	b.d.l.	b.d.l.	b.d.l.	0	5	b.d.l.
Sr	57282	20999	24301	7471	3431	17198
U	b.d.l.	b.d.l.	b.d.l.	b.d.l.	0	b.d.l.
Rb	b.d.l.	b.d.l.	b.d.l.	2	b.d.l.	b.d.l.
Th	b.d.l.	b.d.l.	0	b.d.l.	6	4
Pb	b.d.l.	b.d.l.	b.d.l.	b.d.l.	1	b.d.l.
Ga	254	31	42	8	4	26
Zn	56	12	8	17	7	20
Cu	601	83	63	25	3	36
Ni	99	15	17	4	b.d.l.	8
Co	4	b.d.l.	4	1	b.d.l.	b.d.l.
Cr	19	7	4	11	4	11
Ce	726	92	134	24	15	83
Ba	b.d.l.	b.d.l.	b.d.l.	293	0	b.d.l.
La	b.d.l.	b.d.l.	b.d.l.	b.d.l.	b.d.l.	b.d.l.

	F-1-2 5785'	F-1-3 5786'	F-1-8 5789'	F-1-9 5790'	F-1-16 5795'	F-1-18 5798'	F-1-21 5803'	F-1-27 5806'	F-1-30 5808'	F-1-35 5811'
SiO2	12.30	2.13	.75	5.90	-	.22	7.70	-	.13	1.38
TiO2	.19	.03	.03	.11	.02	.03	.02	.02	.02	.05
Al2O3	4.10	.42	.18	2.32	-	.23	-	.04	.12	1.02
Fe (tot)	1.49	.73	.21	1.33	.08	.21	.06	.12	.16	.58
MnO	.03	.01	-	.03	.02	-	.01	-	0	.01
MgO	16.53	16.17	1.64	15.05	14.77	20.74	8.46	11.84	6.56	19.85
CaO	25.81	31.66	49.80	31.50	30.68	29.07	10.01	15.47	40.86	29.38
Na2O	.40	1.58	1.47	.13	.82	.41	.63	.13	1.35	.25
K2O	.54	.06	.03	.22	.02	-	0	-	.01	.12
P2O5	.05	.01	.02	.02	.02	.01	.01	.01	.01	.01
$CO2_{cal}$	38.3	47.25	40.87	41.15	40.2	45.45	17.09	25.06	39.23	44.72
Total	99.74	100.05	95.0	97.76	86.63	96.37	43.99	52.69	88.45	97.37

Table 3.2, the chemical analyses of the Beda sediments measured from the cored interval of well F1. (b.d.l) below detection limit. (-) values are less than zero on the calibration chart. Equations for CO_2 calculation are listed in Appendix B.

	D-1-1 5900'	D-1-3 5901'	D-1-6 5903'	D-1-7 5904'	D-1-8 5905'	D-1-10 5906'	D-1-12 5907'	D-1-16 5910'	D-1-20 5912'	D-1-21 5913'
Y	4	b.d.l.	7	5	1	3	b.d.l.	b.d.l.	b.d.l.	b.d.l.
Sr	320	45081	2008	243	4500	203	26875	28794	30043	52766
U	8	b.d.l.	4	6	b.d.l.	4	b.d.l.	b.d.l.	b.d.l.	b.d.l.
Rb	22	b.d.l.	16	7	5	4	b.d.l.	b.d.l.	b.d.l.	b.d.l.
Th	3	b.d.l.	9	3	2	3	b.d.l.	b.d.l.	b.d.l.	b.d.l.
Pb	b.d.l.	b.d.l.	3	b.d.l.	1	0	b.d.l.	b.d.l.	b.d.l.	b.d.l.
Ga	5	163	8	1	7	0	69	60	67	185
Zn	13	39	5	15	0	11	17	9	257	219
Cu	b.d.l.	276	1	b.d.l.	4	b.d.l.	113	99	111	318
Ni	5	41	3	b.d.l.	b.d.l.	b.d.l.	12	13	12	45
Co	1	b.d.l.	2	b.d.l.	0	b.d.l.	b.d.l.	b.d.l.	b.d.l.	b.d.l.
Cr	25	15	27	8	8	4	10	8	9	5
Ce	16	479	24	1	21	4	200	182	190	566
Ba	36	b.d.l.	27	10	b.d.l.	28	b.d.l.	b.d.l.	b.d.l.	b.d.l.
La	3	b.d.l.	5	4	b.d.l.	b.d.l.	b.d.l.	b.d.l.	b.d.l.	b.d.l.

	D-1-22 5914'	D-1-23 5915'	D-1-26 5916'	D-1-28 5917'	D-1-30 5919'	D-1-34 5921'	D-1-39 5924'	D-1-42 5925'	D-1-45 5927'	D-1-47 5928'
Y	1	b.d.l.	0	b.d.l.	2	4	4	b.d.l.	b.d.l.	4
Sr	5463	7971	4804	28573	357	304	724	12749	60364	293
U	b.d.l.	b.d.l.	b.d.l.	b.d.l.	1	b.d.l.	13	b.d.l.	b.d.l.	2
Rb	4	2	4	b.d.l.	3	3	0	b.d.l.	b.d.l.	b.d.l.
Th	2	0	b.d.l.	b.d.l.	b.d.l.	b.d.l.	7	1	b.d.l.	6
Pb	b.d.l.	b.d.l.	b.d.l.	b.d.l.	b.d.l.	b.d.l.	1	0	b.d.l.	2
Ga	6	12	6	65	1	0	1	19	328	1
Zn	8	20	3	8	10	3	13	21	49	6
Cu	9	13	7	94	b.d.l.	b.d.l.	b.d.l.	31	544	b.d.l.
Ni	2	0	b.d.l.	10	b.d.l.	b.d.l.	b.d.l.	6	96	b.d.l.
Co	b.d.l.	b.d.l.	b.d.l.	6	b.d.l.	b.d.l.	b.d.l.	b.d.l.	b.d.l.	b.d.l.
Cr	3	1	3	1	1	3	3	4	24	5
Ce	19	29	13	187	b.d.l.	5	6	57	993	6
Ba	b.d.l.	b.d.l.	b.d.l.	b.d.l.	b.d.l.	7	2	b.d.l.	b.d.l.	15
La	3	b.d.l.	b.d.l.	b.d.l.	b.d.l.	b.d.l.	b.d.l.	b.d.l.	b.d.l.	1

	D-1-3 5901'	D-1-8 5905'	D-1-10 5906'	D-1-12 5907'	D-1-16 5910'	D-1-20 5912'	D-1-28 5917'	D-1-39 5924'	D-1-42 5925'	D-1-45 5927'
SiO2	-	.52	-	-	-	-	-	-	-	-
TiO2	.03	.03	.02	.01	.02	.03	.02	.01	.01	.01
Al2O3	.55	.81	.59	.30	.30	.22	.29	.28	.20	.13
Fe (tot)	.23	.28	.25	.24	.07	.05	.08	.32	.23	.10
MnO	.02	.05	.01	.03	.07	.03	.04	-	.04	.02
MgO	12.71	11.52	17.17	16.22	1.36	1.1	.89	17.39	14.13	11.37
CaO	24.54	39.0	29.91	26.83	46.46	47.19	47.62	30.94	30.49	16.45
Na2O	.14	.06	.29	.31	.27	-	.16	.24	-	-
K2O	.09	.10	.07	.05	.04	.04	.04	.05	.04	.04
P2O5	.01	.01	.01	0	0	.01	-	.01	.01	-
$CO2_{cal}$	33.13	43.18	42.21	38.76	37.95	38.23	38.34	43.26	39.35	25.32
Total	71.45	95.59	90.53	82.75	86.54	86.90	87.48	92.50	84.50	53.44

Table 3.3, the chemical analyses of the Beda sediments measured from the cored interval of well D2. (b.d.l) below detection limit. (-) values are less than zero on the calibration chart. Equations for CO_2 calculation are listed in Appendix B.

	C-1-3 5556'	C-1-5 5558'	C-1-7 5560'	C-1-11 5562'	C-1-16 5565'	C-1-18 5568'	C-1-20 5570'	C-1-21 5572'	C-1-24 5573'	C-1-26 5576'
Y	1	4	b.d.l.	b.d.l.	b.d.l.	1	4	5	b.d.l.	b.d.l.
Sr	8026	3592	20501	15446	15030	8734	558	432	26305	28249
U	b.d.l.	b.d.l.	b.d.l.	b.d.l.	b.d.l.	b.d.l.	3	5	b.d.l.	b.d.l.
Rb	0	0	b.d.l.	b.d.l.	b.d.l.	b.d.l.	4	1	b.d.l.	b.d.l.
Th	1	4	b.d.l.	b.d.l.	0	3	6	5	b.d.l.	b.d.l.
Pb	b.d.l.	2	b.d.l.	b.d.l.	b.d.l.	b.d.l.	0	b.d.l.	b.d.l.	b.d.l.
Ga	11	5	45	27	23	12	0	0	66	72
Zn	2	b.d.l.	5	1	b.d.l.	0	b.d.l.	b.d.l.	8	47
Cu	11	b.d.l.	67	40	33	14	b.d.l.	b.d.l.	102	111
Ni	1	b.d.l.	14	1	6	1	b.d.l.	b.d.l.	16	20
Co	b.d.l.	1	b.d.l.	0	b.d.l.	1	2	b.d.l.	b.d.l.	b.d.l.
Cr	7	6	8	3	6	2	6	3	10	8
Ce	32	17	130	79	69	36	1	6	191	226
Ba	b.d.l.	1	b.d.l.	b.d.l.	b.d.l.	b.d.l.	11	6	b.d.l.	b.d.l.
La	b.d.l.	b.d.l.	b.d.l.	b.d.l.	b.d.l.	b.d.l.	1	1	b.d.l.	b.d.l.

	C-2-1 5577'	C-2-4 5579'	C-2-7 5580'	C-2-10 5582'	C-2-13 5584'	C-2-15 5586'	C-2-19 5589'	C-3-1 5599'	C-3-3 5600'	C-3-5 5601'
Y	3	b.d.l.	3	4	b.d.l.	b.d.l.	4	5	0	6
Sr	2874	26506	573	216	36083	27705	4554	981	13850	1482
U	b.d.l.	b.d.l.	2	0	b.d.l.	b.d.l.	b.d.l.	6	b.d.l.	2
Rb	1	b.d.l.	1	1	b.d.l.	b.d.l.	6	12	5	10
Th	4	b.d.l.	4	4	b.d.l.	b.d.l.	6	5	2	2
Pb	0	b.d.l.	b.d.l.	0	b.d.l.	b.d.l.	1	3	1	0
Ga	3	66	b.d.l.	b.d.l.	115	74	8	4	23	3
Zn	0	116	b.d.l.	9	14	11	4	68	10	6
Cu	b.d.l.	106	b.d.l.	b.d.l.	186	111	6	b.d.l.	33	1
Ni	b.d.l.	16	b.d.l.	b.d.l.	30	12	2	1	13	6
Co	b.d.l.	b.d.l.	0	b.d.l.	2	1	1	0	0	1
Cr	3	5	5	11	7	13	20	22	34	17
Ce	8	193	0	2	345	219	27	18	81	19
Ba	b.d.l.	b.d.l.	10	10	b.d.l.	15	b.d.l.	9	2	9
La	b.d.l.	b.d.l.	3	b.d.l.	b.d.l.	b.d.l.	b.d.l.	1	b.d.l.	8

	C-3-10 5604'	C-3-13 5607'	C-3-19 5614'	C-3-22 5618'
Y	4	4	4	3
Sr	373	4875	333	391
U	7	b.d.l.	6	6
Rb	5	4	2	2
Th	5	6	2	5
Pb	3	1	b.d.l.	b.d.l.
Ga	2	7	1	b.d.l.
Zn	0	1	1	3708
Cu	b.d.l.	11	b.d.l.	b.d.l.
Ni	3	5	b.d.l.	1
Co	b.d.l.	b.d.l.	0	0
Cr	17	10	4	7
Ce	1	18	4	6
Ba	8	12	b.d.l.	b.d.l.
La	b.d.l.	b.d.l.	1	3

Table 3.4, the chemical analyses of the Beda sediments measured from the cored interval of well G41. (b.d.l) below detection limit.

	C-1-3 5556'	C-1-7 5560'	C-1-11 5562'	C-1-16 5565'	C-1-24 5573'	C-1-26 5576'	C-2-4 5579'	C-2-13 5584'	C-2-15 5586'	C-2-19 5589'
SiO2	.02	-	-	-	-	-	-	-	-	2.39
TiO2	.02	.02	.01	.01	0	.01	.01	.01	.01	.07
Al2O3	.71	.34	.18	.15	.24	.21	.23	.24	.24	1.81
Fe (tot)	.31	.17	.25	.10	.1	.12	.10	.14	.24	.49
MnO	.01	.05	.06	.05	.02	.03	.03	.04	.02	.01
MgO	16.31	16.14	15.43	5.05	15.91	16.31	15.43	15.39	17.74	3.03
CaO	26.83	25.81	25.58	47.32	25.37	26.16	23.94	23.72	26.19	48.65
Na2O	-	.02	.01	-	.07	-	-	-	-	-
K2O	.08	.08	.04	.03	.04	.03	.03	.03	.04	.22
P2O5	.01	.01	.01	.01	.01	0	.01	-	.01	.01
$CO2_{cal}$	38.86	37.86	36.92	42.65	37.28	38.33	35.63	35.41	39.97	41.49
Total	83.16	80.50	78.49	95.38	79.03	81.20	75.41	74.98	84.41	98.20

	C-3-3 5600'	C-3-22 5618'
SiO2	4.50	-
TiO2	.12	.02
Al2O3	2.85	.19
Fe (tot)	.89	.03
MnO	.02	-
MgO	6.17	1.04
CaO	40.90	55.83
Na2O	-	.06
K2O	.35	.04
P2O5	.02	.01
$CO2_{cal}$	38.83	44.95
Total	94.65	102.17

Table 3.4, Continued. (-) values are less than zero on the calibration chart. Equations for CO_2 calculation are listed in Appendix B.

3.1.2 Stable Isotope Analyses

The isotopic analyses of dolomite and sulfates were carried out at the Isotope Laboratory of the Isotope Geology Unit at the Scottish Universities Research Reactor Center (SURRC). The isotope analyses of ($\delta^{13}C$) and ($\delta^{18}O$) were made by a VG Isotech Sira 10 mass-spectrometer and the acid reaction of carbonates part was based on the procedure described by McCrae (1950). For precision, the isotopic analyses of oxygen and carbon were made in duplicate. The isotope analyses of $\delta^{34}S$, were made by a VG Isotech Sira 2 mass-spectrometer and the extraction of SO_2 part of the analysis was based on the technique described by Coleman and Moore (1978).

In the case of the dolomite, all the samples were analyzed by X-ray diffraction before the carbon ($\delta^{13}C$) and oxygen ($\delta^{18}O$) isotopic analyses were made. This was basically to check the impurities of these dolomite samples. A few samples were found to contain minor amounts of calcium sulfates, anhydrite-gypsum, and minor traces of celestite ($SrSO_4$). Since the dolomite samples are very fine grained and hence did not permit physical separation of the dolomite from celestite or anhydrite, a chemical separation technique was used. Following this, the carbon dioxide (CO_2) gas was extracted for mass spectrometer analyses. The extraction of CO_2 gas was obtained by reacting the powdered dolomite samples with 100% phosphoric acid at 25°C for three days. After three days, the CO_2 gas was collected and then analyzed, by the mass spectrometer, for carbon ($\delta^{13}C$) and oxygen ($\delta^{18}O$) isotopes, and the data (Table 3.5) are reported as per mil deviation relative to the Chicago CO_2 standard PDB. The oxygen data are also reported in SMOW standard. However, for carbonate oxygen, the PDB standard is more commonly used than SMOW. The conversion between the two scales

can be made using the equations given by Coplen et. al. (1983) and listed in Appendix B, but for convenience both scales are given in listing results (see Table 3.5).

In the case of the sulfur isotope analyses, the calcium sulfate samples were analyzed for $\delta^{34}S$ isotopes by heating a mixture, consisting of about 15-20 mg of powdered calcium sulfate sample, 600 mg of fine silica, and 200 mg fine copper (Cu_2O) to 1120^{o}C. The liberated gases other than SO_2 were vacumed out, and the extracted SO_2 gases were then analyzed for $\delta^{34}S$ isotopes. The $\delta^{34}S$ data (Table 3.6) are reported as per mil relative to troilite of the Canon Diablo meteorite (CDT).

3.2 Results and Discussion

3.2 1 Trace elements

The most striking feature of the trace element contents of Beda sediments in this study, are the anomalously very high values of Sr and Zr, whereas, the Fe, Mn, Si, and Al contents (presented in oxide form) are generally low. These elements will be discussed below and the vertical distribution of their concentrations are plotted in figures 3.1-3.4.

1- Strontium (Sr)

Strontium is an important constituent of the precursor carbonate sediments and is usually used as an indicator of precursor carbonate

Well No.	Depth (ft)	$\delta^{13}C$ (PDB)	$\delta^{18}O$ (PDB)	$\delta^{18}O$ (SMOW)
E2	6912	3.24	-3.83	26.96
	6921	3.11	-5.23	25.52
F1	5795	2.97	-1.5	29.36
	5796	2.99	-1.78	29.08
	5801	3.64	-2.84	27.95
	5804	3.13	-4.99	25.77
D2	5905	3.52	-2.16	28.69
	5908	3.75	-3.26	27.55
	5925	3.15	-5.73	25.01
G41	5558	3.28	-2.22	28.62
	5561	3.39	-1.86	28.99
	5570	3.49	-2.68	28.14
	5572	3.28	-4.29	26.49
	5583	3.71	-5.48	25.26
	5587	3.73	-5.28	25.46
G4	5408	2.05	-5.41	25.33

Table 3.5, the results of carbon and oxygen isotope analyses of dolomite, results are expressed in parts per mil.

Well No	Depth (ft)	$\delta^{34}S$ (CDT)
E2	6908	21.86
	6914	22.88
F1	5792	20.87
	5793	20.99
	5797	20.61
	5811	21.96
G41	5555	22.24
G4	5413	20.59
	5422	20.32
	5433	19.82

Table 3.6, the results of sulfur isotope analyses of calcium sulfates, results are expressed in parts per mil.

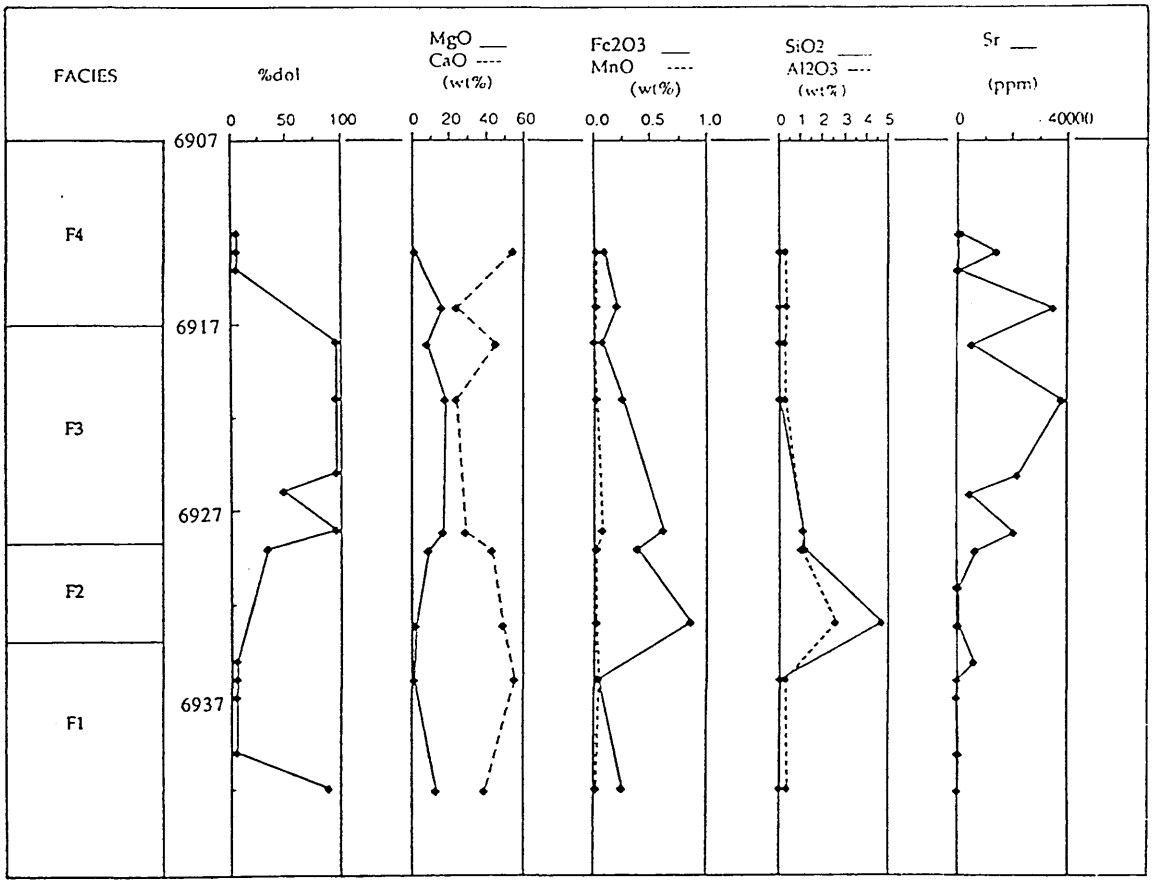

Fig. 3.1, Shows the vertical distribution of major and trace element concentrations of the cored interval of Well E2.

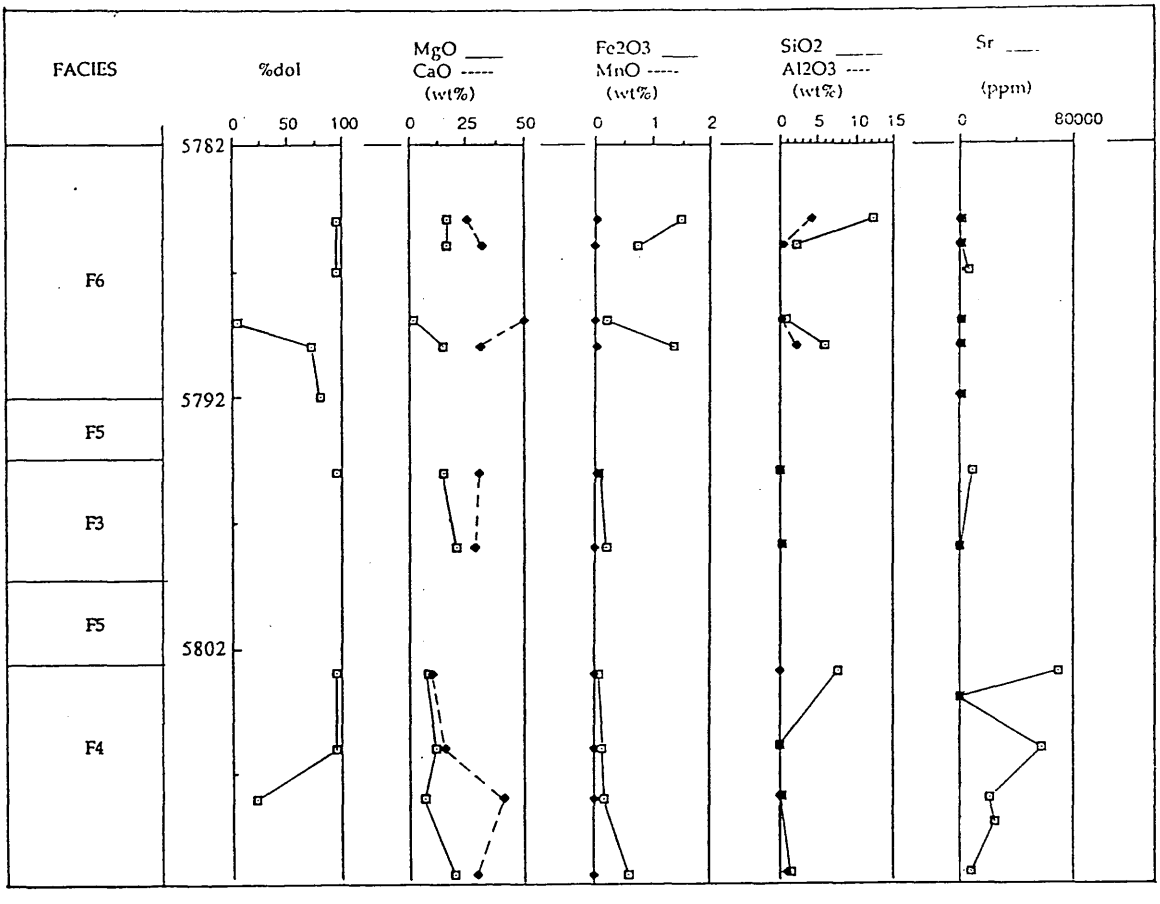

Fig. 3.2, Shows the vertical distribution of major and trace element concentrations of the cored interval of Well F1.

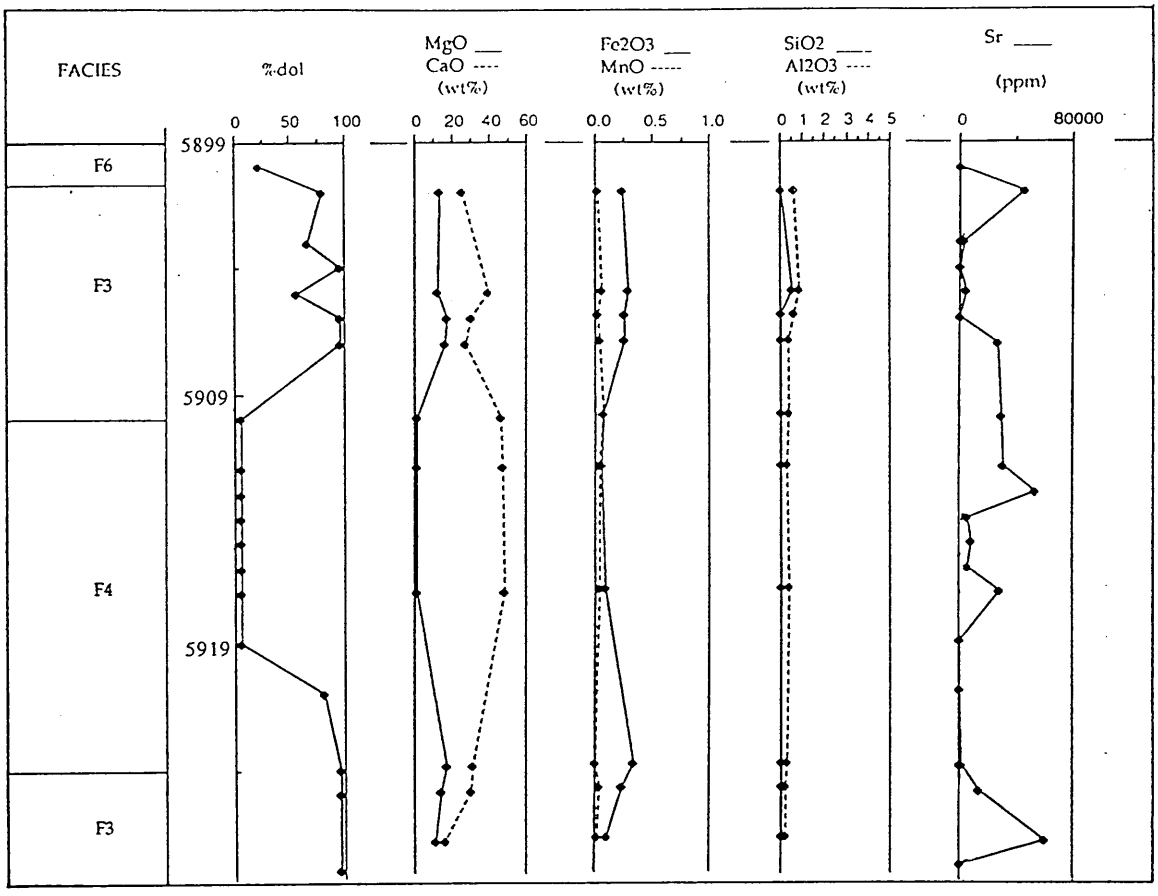

Fig. 3.3, Shows the vertical distribution of major and trace element concentrations of the cored interval of Well D2.

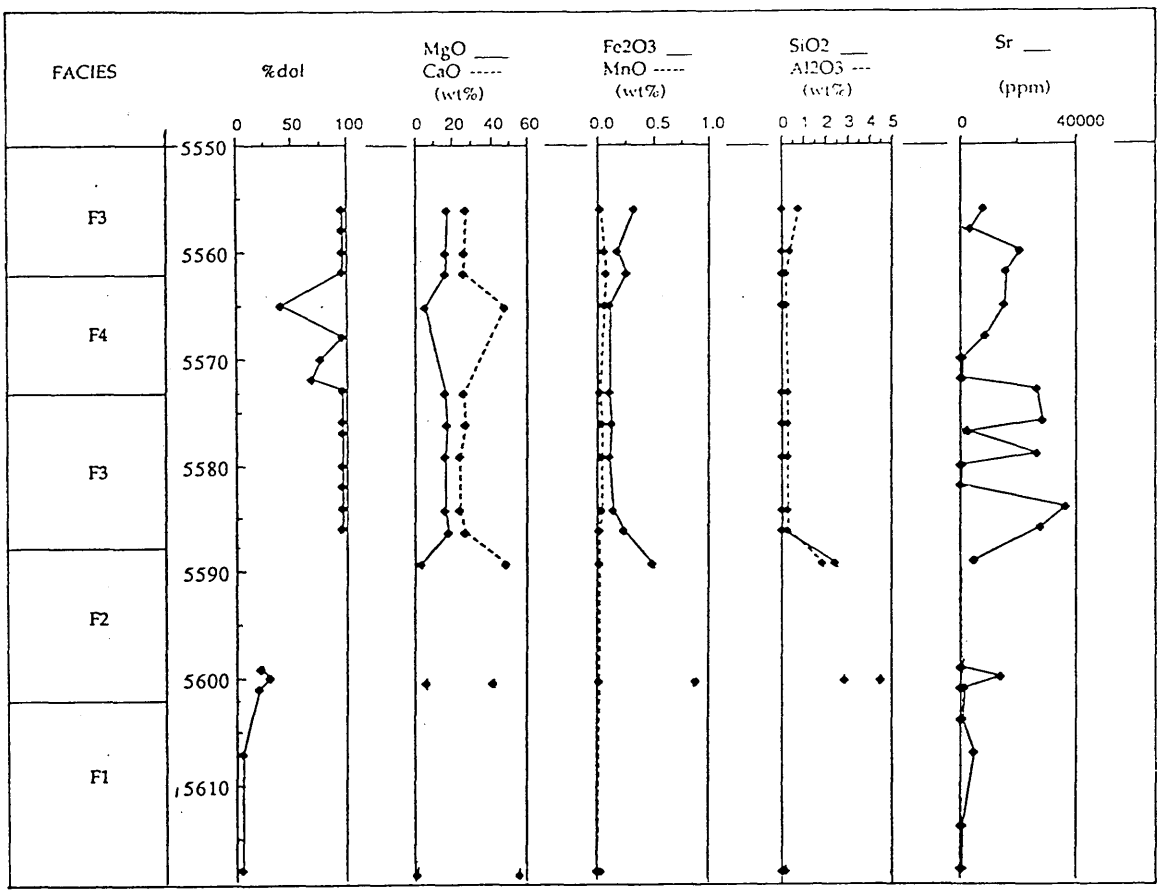

Fig. 3.4, Shows the vertical distribution of major and trace element concentrations of the cored interval of Well G41.

mineralogy, being enriched in marine aragonite with an average Sr content of about 9800 ppm (Kinsman, 1969) relative to high-Mg calcite with Sr contents ranging from 400-1000 ppm (Land and Goreau, 1970) to typically less than 4000 ppm (Land and Hoops, 1973). In the case of dolomite, the Sr content has been used to place constraints on the composition of the dolomitizing fluids and on the dolomitization model (Veizer, 1983a). Dolomites believed to have precipitated from a mixture with more than 20% seawater could have a typical marine Sr content of around 550 ppm while those which formed from hypersaline solutions would have much more Sr than this. This is because (1) when the salinity of the seawater rises so that calcium sulfates, gypsum-anhydrite, are precipitated, the Sr/Ca ratio rises slightly (Kinsman, 1966, 1969), and (2) a decrease in the precipitation ratio of gypsum to celestite will increase the Sr/Ca ratio. The other important factor in determining the dolomite Sr content, is the time of dolomitization. As a generalization, early diagenetic finely crystalline dolomites have higher Sr contents than later diagenetic coarse dolomites (Veizer et. al., 1978).

The Sr concentrations of the Beda sediments in this study are generally high. In most of the samples analyzed, the Sr content ranges from around 200 to 9000 ppm, and about 22 samples have anomalously very high Sr contents, ranging, approximately, from 13000 to 70000 ppm. In this study, the Sr/Ca ratios were plotted (Fig. 3.5) against the Mg/Ca ratios. The relationship between Sr/Ca and Mg/Ca ratios, as revealed from this plot, is that the Sr/Ca ratio increases as the Mg/Ca ratio increases, indicating a positive relationship between Sr and Mg content. However, this is unusual, because it has been suggested that because of relative ionic sizes, Sr would substitute primarily for Ca rather than for Mg in the dolomite crystal

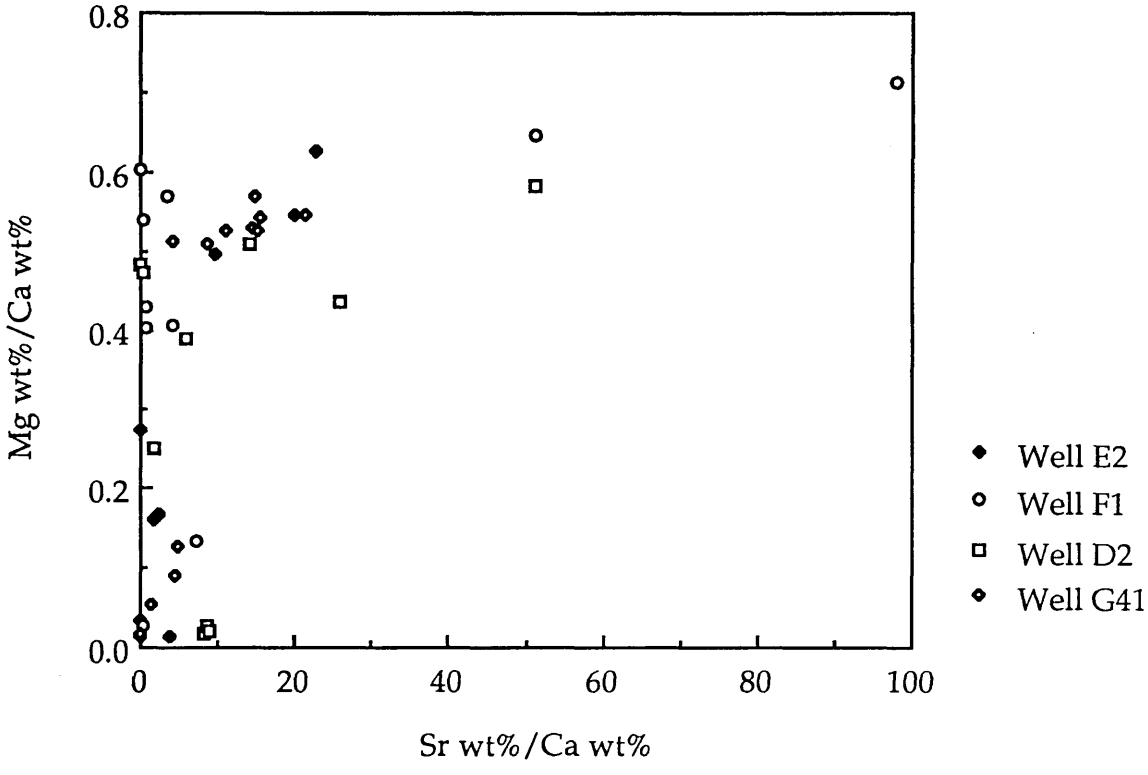

Fig. 3.5, Mg/Ca ratio versus Sr/Ca (x10-2) ratio plot, showing a positive relationship between increasing Mg/Ca ratio and Sr/Ca ratio (i.e. Sr is richer in dolomite).

structure and therefore, Sr is usually depleted in dolomite relative to calcite (Behrens & Land, 1972; Kretz, 1982; Andrews, et. al., 1987). This unusual relationship is probably caused by the presence of minor amounts of celestite ($SrSO_4$) in the sediments, detected by XRD (Fig. 3.6, 3.7). Therefore, these high Sr contents are probably the result of celestite precipitation.

The sedimentological observations discussed in Chapter 2 suggest that periodically hypersaline conditions were prevailing during deposition. Additional support for such ideas is given by the high Sr contents and by the presence of celestite. Celestite precipitation commonly, occurs as an early diagenetic phase in hypersaline sequences (Braitsch, 1971), and is especially abundant in areas of intense dolomitization, being largely a by product of replacement of aragonite by dolomite. Analogous Holocene hypersaline environments contain ubiquitous aragonitic muds. For example, along the Trucial Coast of the Arabian (Persian) Gulf, aragonite is the dominating mineral in hypersaline lagoonal facies (e.g. Bathurst, 1975; Veize and Rudolf, 1974; Veizer et. al., 1978). Thus, the Sr in these sediments was derived from dolomitization and dissolution of a Sr-rich aragonite precursor.

2- Zirconium (Zr)

Zirconium is generally scarce in carbonate and evaporite rocks but, very high Zr contents (up to 3500 ppm) have been measured from the studied carbonate sediments of the Beda Formation. These anomalously high values show a positive relationship with the Sr content. Where the Sr content increases, the Zr content also increases (Fig. 3.8). A similar

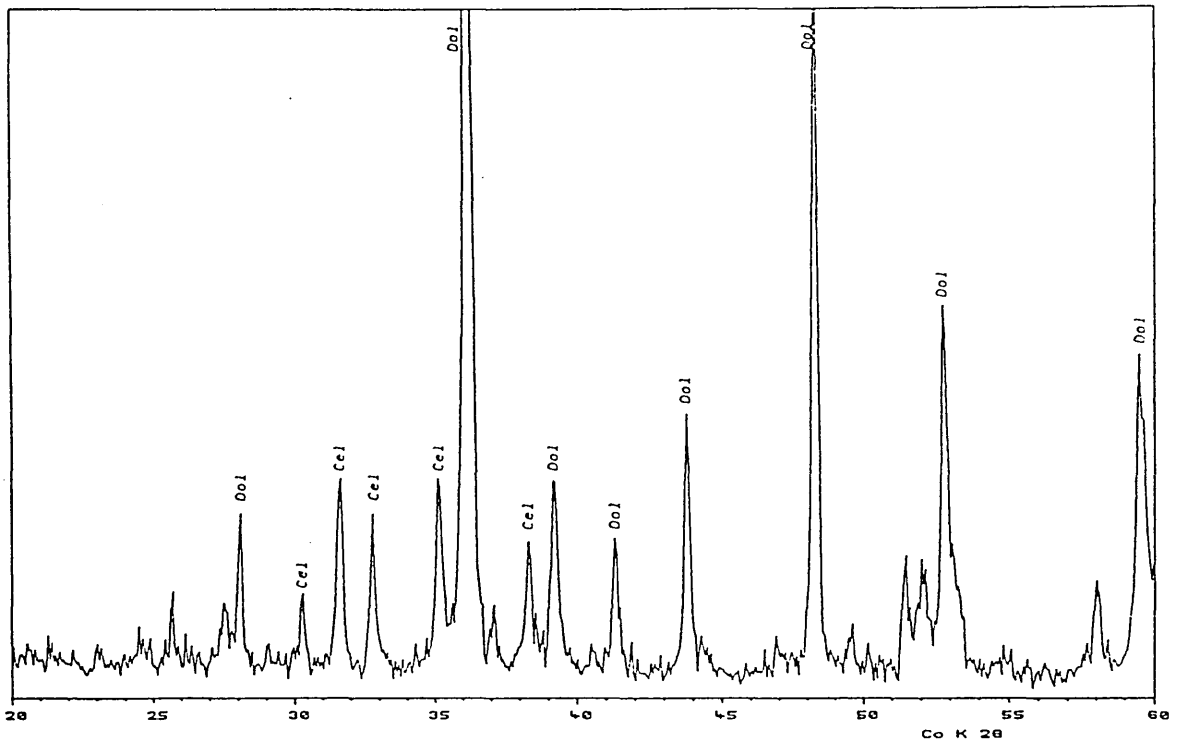

Fig. 3.6, X-ray diffraction pattern, showing the presence of celestite (Cel) with the dolomite (Dol). Sample E-1-16, well E2 (Sr=38212 ppm, determined by XRF).

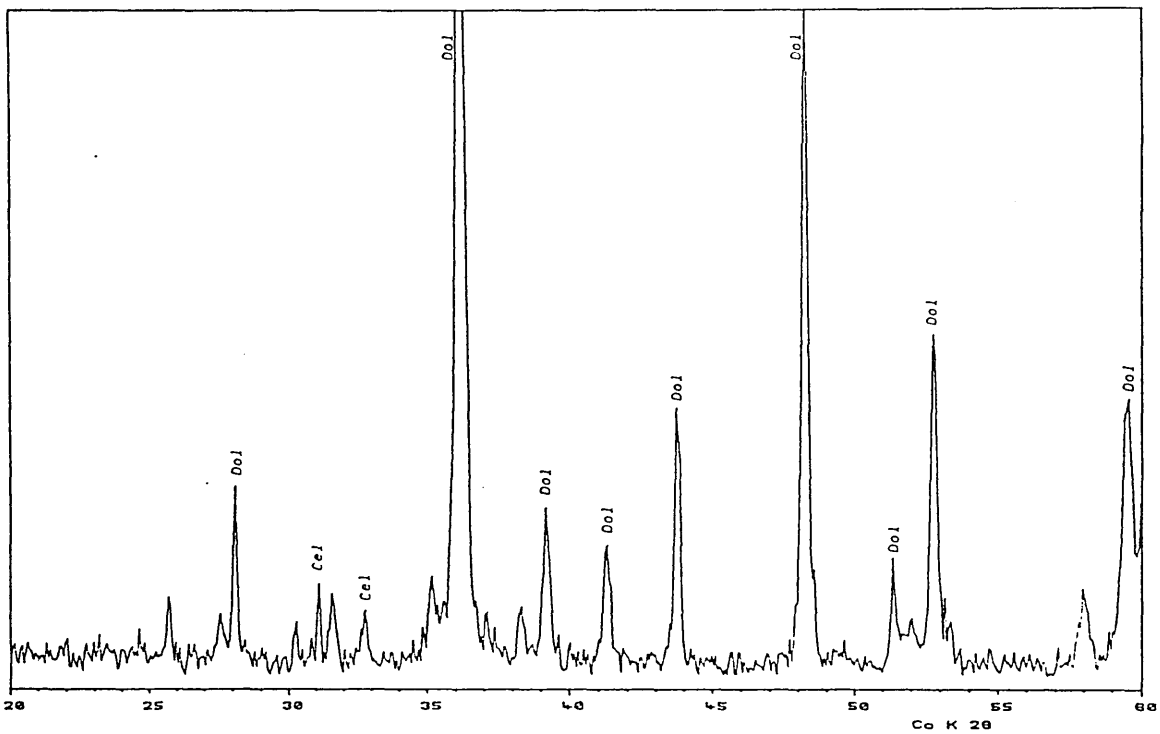

Fig. 3.7, X-ray diffraction pattern, showing the presence of celestite (Cel) with the dolomite (Dol). Sample E-1-27, well E2 (Sr=20514 ppm, determined by XRF).

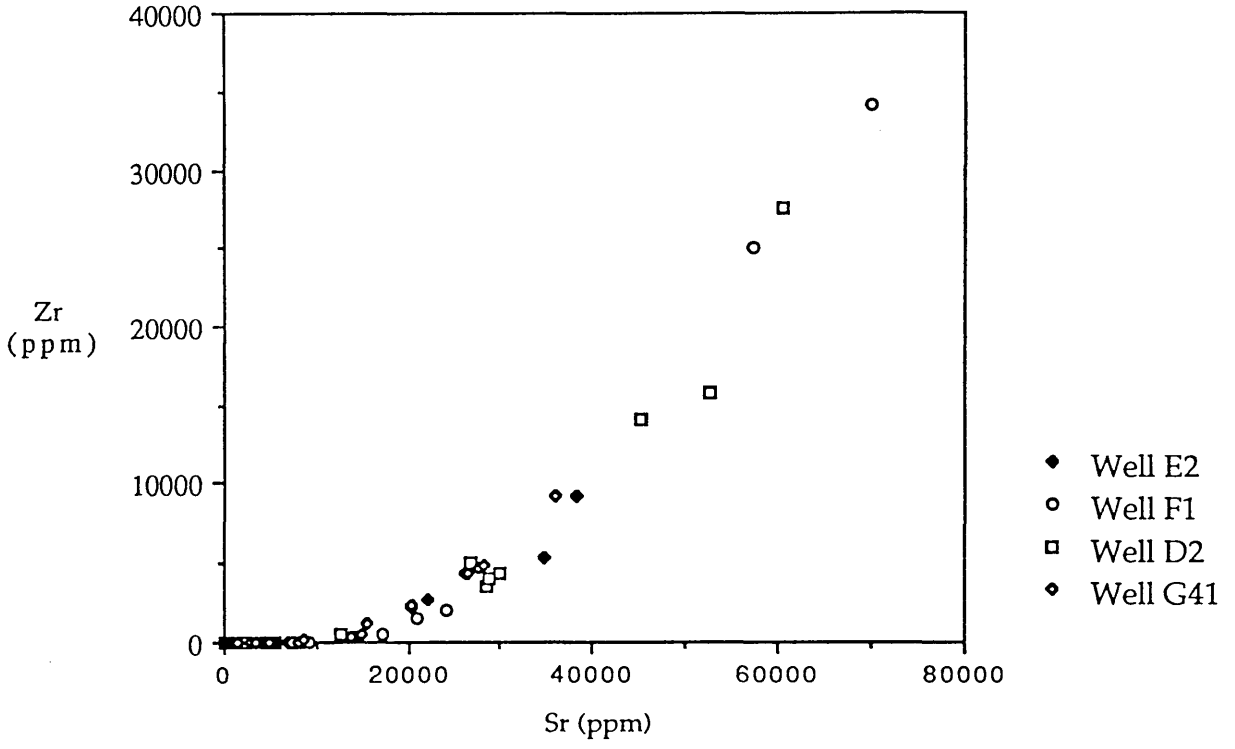

Fig 3.8, Sr versus Zr concentrations plot. Note there is a positive relationship. The Zr content increase with the increase of Sr content.

relationship between Sr and Zr has been observed by Leake et al. (1969). They found that when about 1000 ppm Sr was added to Zr, the Zr concentration was increased by about 46 ppm Zr above the mean Zr value of 76 ppm (the mean value was determined from four measurments , not considered to be affected by added trace elements). Their interpretation is that Zr suffers interference from the SrKß1 peak where the Zr and Sr peaks overlap. Since, Zr is generally scarce in carbonate rocks and also since such very high concentrations are uncommon, the Zr values are not considered reliable here. They probably only represent interference from the SrKß1 peak.

3- Iron and Manganese

Iron (Fe) and Manganese (Mn) are generally present in very low concentrations in seawaters, relative to fresh waters. Fresh waters contain more soluble Fe and Mn than do seawaters (Freidman, 1969). The two elements tend to be picked up by carbonate precipitates during diagenesis and are preferentially incorporated in the dolomite lattice, relative to Ca.

In this study, the Fe and Mn contents of the Beda dolomite are generally very low. The Fe concentrations, given as total Fe in the form of Fe_2O_3 include both the ferric (Fe_2O_3) and ferrous (FeO) iron, and range from .03 to approximately 0.9 wt%. Because of the low Fe concentrations, no attempt was made to distinguish between the two oxidation states. The Mn contents, given as Mn oxides (MnO), range from <.01 to .07 wt%. These very low Fe and Mn concentrations of the Beda dolomites are in line with those expected from early near-surface dolomites, which tend to have low

Fe and Mn contents, contrasting with later, burial dolomites, which may have high contents of Fe and Mn (Land, 1985). For example, the early diagenetic fine-grained dolomite of the Trenton Formation in the Michigan Basin has .06-.34 mol% Fe (≈.05-.29 wt%) (Taylor & Sibely, 1986). This is because, most early near-surface dolomites are formed under the oxidizing conditions characteristic of shallow water carbonate shelves. A slight increase in iron concentration (>1.0 wt%) has been recorded from facies 6 in well F1 (Fig. 3.2), while the Mn contents remain low. This is probably due to the presence of clay materials and pyrite.

4- Si, Al, and K

The Si, Al, and K elements, given in their oxides; SiO_2, Al_2O_3, and K_2O are present in very low concentrations, generally less than 1 wt%. These low concentrations are due to the general absence of clay materials. However, samples from facies 2 in wells E2 and G41, and facies 6 in well F1, show concentrations greater than 1 wt% for SiO_2 and Al_2O_3 (Figs. 3.1, 3.2, and 3.4), while the K_2O contents show only a slight increase and remain less than 1 wt%. The increase of these elements across these facies is due to the presence of argillaceous (clay) materials represented particularly by the clay mineral illite-smectite (see Chapter 2, Plate 2.7).

3.2.2 Oxygen and Carbon isotopes

Analyses of stable isotopes of oxygen and carbon have become increasingly used in the interpretation of dolomites and, when combined

with trace elements and petrography, can help to give clarifying explanation on the origins of these rocks. Several workers (e.g. Epstein et al., 1964; Degens and Epstein, 1964; Land, 1980; etc) have used these isotopes in dealing with this problem.

The isotopic analyses of oxygen and carbon made on the dolomite of this study, show that this dolomite is generally depleted in ^{18}O isotopes, having quite negative $\delta^{18}O$ values. These $\delta^{18}O$ values tend to be lighter (more negative) with depth (Table 3.5), and range between -1.5 to -5.7 per mil (PDB). The $\delta^{13}C$ values range between +2.05 to +3.64 per mil with an average of +3.27 per mil (PDB), and are within the range of $\delta^{13}C$ isotope values characteristic of marine water isotopic signature ($\delta^{13}C$=0 to +4 per mil). Generally, the $\delta^{18}O$ and $\delta^{13}C$ results showed no discrimination between the dolomites of this study. Plot of the carbon-oxygen isotope data (Fig. 3.9), shows a wide range of distribution in the $\delta^{18}O$ data, whereas, the $\delta^{13}C$ values show much less variation and hence have a narrow range of distribution. An equilibrium relationship between the $\delta^{18}O$ of dolomite, the $\delta^{18}O$ of water, and temperature was constructed (Fig. 3.10) to predict the precipitating temperature of the Beda dolomite. Given a constant range of $\delta^{18}O$ values (25, 28, and 30 per mil vs SMOW), which represent the range of $\delta^{18}O$ values measured from the Beda dolomite of this study, the $\delta^{18}O$ values of the water were calculated for each value, over a temperature range of 20 to 100°C, using the dolomite-water fractionation equation given by Fritz and Smith (1970) (see Appendix B). This figure suggests that precipitation from marine water ($\delta^{18}O$=0 per mil), of dolomites with such an isotopic range ($\delta^{18}O$=25-30 per mil) would have to have taken place at a temperature, which varied between 30 and 60°C. If, however, salinities were higher then the temperature derived from $\delta^{18}O$

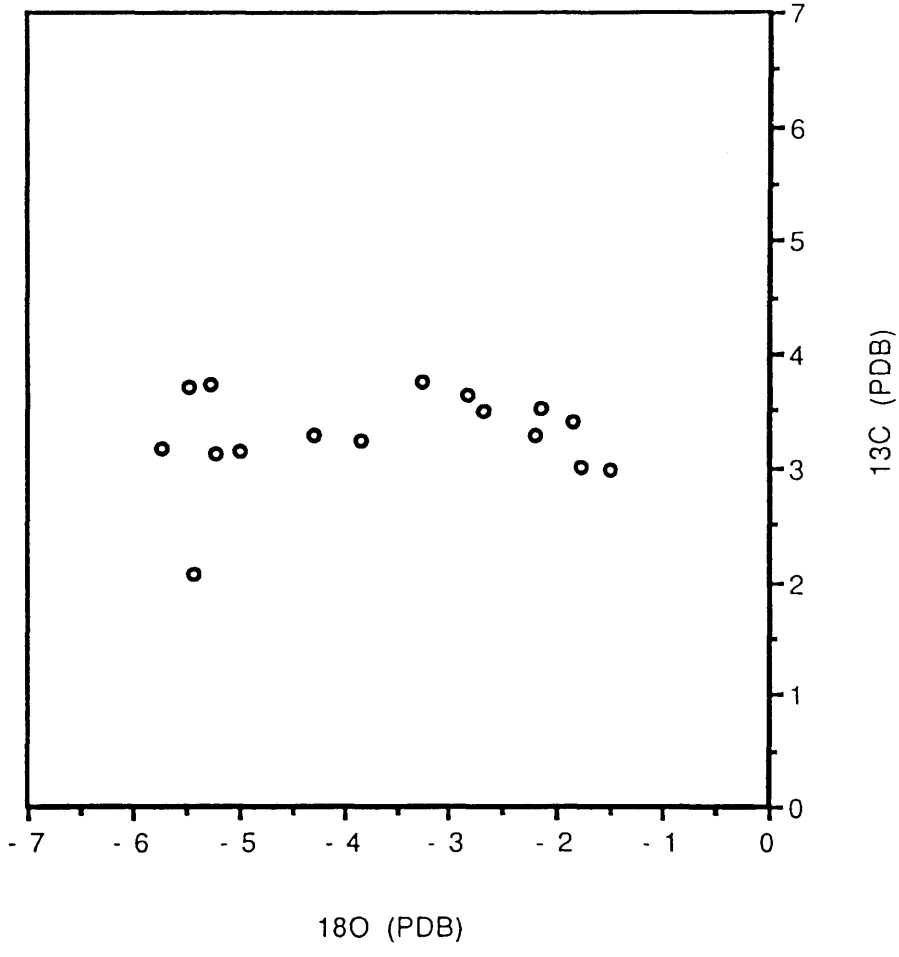

Fig. 3.9, Carbon-oxygen isotopic composition of the Beda dolomite. There is a trend toward more depleted ^{18}O isotopes, whereas, the $\delta^{13}C$ isotopes show only little variations.

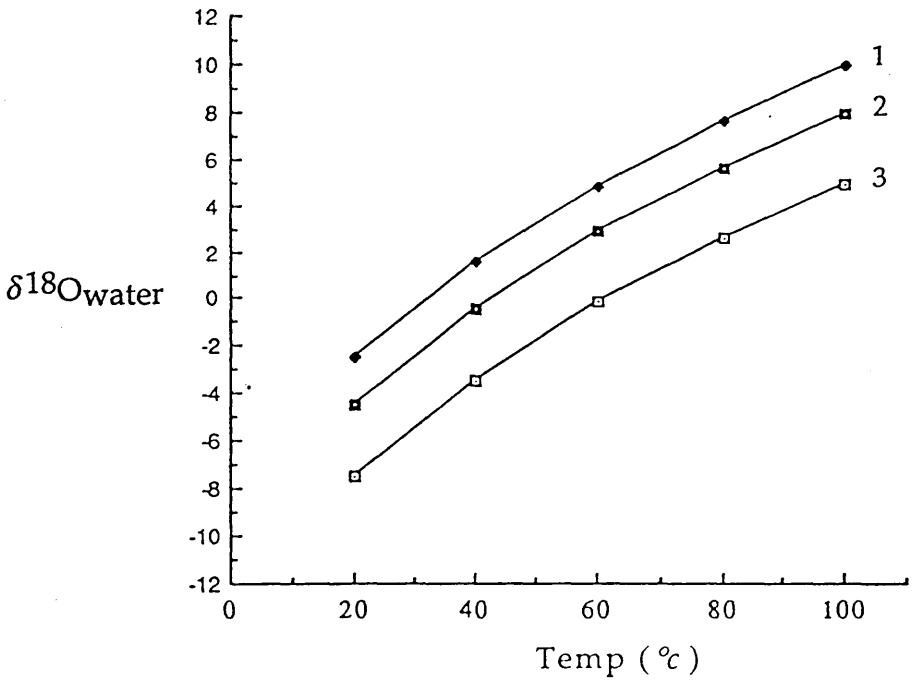

Fig 3.10, Equilibrium relationship between the measured $\delta^{18}O$ of the dolomite (curved lines), temperature, and calculated $\delta^{18}O$ of water. The curved lines represent constant $\delta^{18}O$ (SMOW); (1) $\delta^{18}O$=30 per mil, (2) $\delta^{18}O$=28 per mil, and (3) $\delta^{18}O$=25 per mil.

would also be higher.

In general, the oxygen isotopic composition of dolomite mainly reflects the temperature of precipitation and the isotopic composition of the dolomitizing fluids. It has been suggested by Land (1985, Fig. 7) that dolomites more depleted than about -2 per mil must have either formed from or been affected by either water depleted in ^{18}O with respect to seawater, or by elevated temperatures. For example, meteoric waters are normally depleted in ^{18}O, whereas, waters which have undergone evaporation tend to be isotopically enriched in ^{18}O. This is because during the early phases of evaporation the lighter oxygen isotopes are preferentially removed and the residual fluid becomes enriched in the heavier ^{18}O isotopes. However, in the case of extreme evaporation to halite facies and beyond, the progressive enrichment of ^{18}O does not continue indefinitely and the $\delta^{18}O$ starts to decrease (Fallick, 1991; Holser, 1979; Knauth and Beaunas, 1985, Fig. 4). The other factor that might affect the isotopic composition of the dolomitizing fluids is the water/rock ratio, where in low water/rock ratio the isotopic composition may be influenced by the isotopic composition of the $CaCO_3$ minerals (aragonite or calcite) being replaced. However, this is unlikely since dolomitization requires substantial amounts of water.

In this study, the most likely reason for the negative $\delta^{18}O$ values would be elevated temperatures rather than meteoric water. This is because, on the basis of the other evidence, such as the precipitation of sulfates; gypsum and anhydrite (chapter 2), and the high Sr contents and the low Fe and Mn concentrations (section 3.2.1), meteoric water influence would be the least expected, since the addition of meteoric water normally

results in Sr depletion (Bein and Land, 1983) and such water tends to contain more soluble Fe and Mn than seawater (Freidman, 1969). Also, no halite precipitation, except for less than 2.0 wt% (determined by XRFS) was found in these sediments. There is no independent evidence to suggest that an extreme evaporation to halite facies might be responsible for these negative $\delta^{18}O$ values, positive values would be expected from evaporated seawater. However, the study area was affected by volcanic activity during the Quaternary and probably very recently (chapter 1). This supports the idea that elevated temperatures were the main factor resposible for the change of the isotopic composition of the studied dolomite, towards negative $\delta^{18}O$ values. These $\delta^{18}O$ values represent the modification of original ^{18}O by lighter ^{18}O derived by hotter water.

The $\delta^{13}C$ value of dolomite is generally strongly influenced by the isotopic composition of the precursor $CaCO_3$ (aragonite or calcite) rather than by temperature or the isotopic composition of the pore-fluids. This is because so much more carbon resides in the carbonate precursor minerals than in the pore fluids and, in contrast to oxygen isotopes, the equilibrium fractionation of carbon isotopes is less temperature sensitive. Thus, the $\delta^{13}C$ value of the $CaCO_3$ mineral being dolomitized is commonly retained by the dolomite.

3.2.3 Sulfur isotope

The sulfur $\delta^{34}S$ isotope data measured from the evaporite facies of this study, vary from 19.8 to 22.28 per mil (CDT) with an average of approximately 21.21 per mil. These values are generally within the range of

$\delta^{34}S$ isotope values characteristic for marine evaporites of Tertiary age which give a $\delta^{34}S$ range between 19 to 22 per mil (Claypool et al., 1980, Fig. 4). It has also been suggested by Thode and Monster (1965) that ancient evaporites would reflect the isotopic composition of their contemporary seas. Thus, the $\delta^{34}S$ values of sulfate evaporites are directly related to the $\delta^{34}S$ values of the aqueous sulfate reservoir where crystallization occurred.

CHAPTER FOUR
DIAGENESIS

The rocks studied vary in general from mudstones to wackestones. Diagenetic alterations have in parts modified and locally obscured the depositional textures of these rocks, which makes the interpretation of the original texture sometimes quite difficult. However, the remaining and less affected intervals, are predominantly wackestones and vary from sparse biomicrite to packed biomicrite to packed bio-pelmicrite (following Folk, 1962), and are generally fine-grained.

Thin-section petrography, cathodoluminescence (CL), and SEM were used to investigate the possible diagenetic processes that took place in these sediments and which were probably responsible for these changes. A number of diagenetic events are inferred from this study which vary from early fibrous calcite cement growth through dissolution and the growth of blocky calcite to dolomitization and the growth of sulfates cements to late diagenetic changes such as compaction, development of baroque dolomite cement, and Pb-mineralization. The relative timing of each diagenetic event is presented in Figure 4.1.

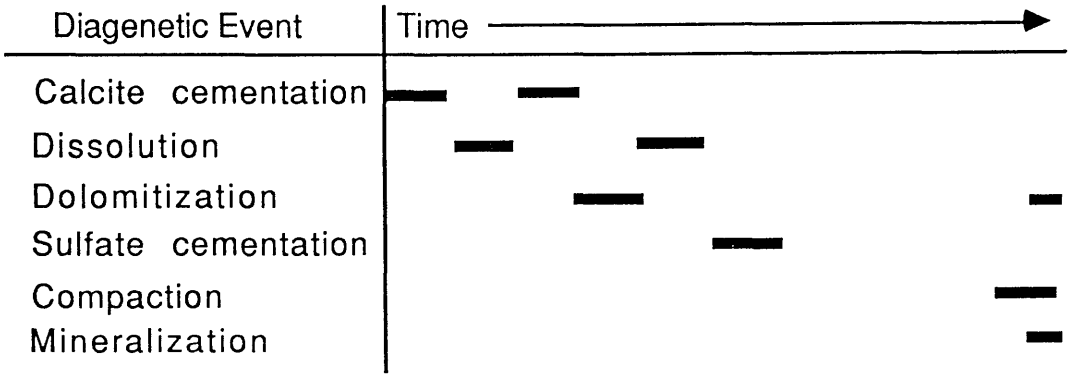

Fig. 4.1 , summary of the observed diagenetic events and their relative timing.

4.1 Diagenetic Events

4.1.1 Cementation

Two main types of cement were found to affect the sediments of the Beda Formation and to lead to porosity reduction, . These are (1) calcite and (2) calcium sulfates, dominated by gypsum.

1- Calcite cement

From thin-section petrography two possible generations of calcite cements can be inferred from the sediments studied, and are particularly common in facies 1 and facies 4. The first generation of cement is represented by fibrous calcite cement, seen to be growing on the walls of foraminifera (e.g. Miliolids) and ostracods. Crystals in this fibrous calcite cement tend to increase in size, both inwards and outwards, away from the surface of the test, occluding the primary intergranular and intragranular

porosity (Plate 4.1, A-C). In general these calcite crystals are fine grained and the crystal size seems to be controlled by the original size of the pore spaces, which they occupy. The fact that the fibrous cements were preserved while aragonite shells were dissolved suggests that these were calcite rather than aragonite. Early marine cements are commonly high-Mg calcite. The second generation of calcite cement is represented by the formation of large, blocky calcite crystals. These crystals are mostly found filling residual primary pores, molds of dissolved molluscan shell fragments (commonly aragonitic shells), and vugs, developed after the precipitation of the first calcite cement (Plate 4.1, D,E).

Calcite also occurs as syntaxial calcite overgrowths on echinoderm fragments (Plate 4.1, F). However, these are rare.

2- Calcium sulfate cement

Calcium sulfates (dominated by gypsum), occurring both as cements and as replacements, are common throughout most of the studied intervals, but are more abundant in facies 3 and facies 4. They fill intercrystalline pores, molds, and vugs, and form large poikilotopic crystals (commonly of gypsum), engulfing fossil fragments, peloids, calcite crystals, and dolomite rhombs (Plate 4.2, A-C). This suggests that the calcium sulfate cementation and replacement postdates calcite cementation and dolomitization. This is also indicated by the form of contact between the calcite crystals and gypsum crystals when they occur together. Plate 4.2, D-F, shows the contact relationship between the calcite crystals and the gypsum.

4.1.2 Dissolution

Petrographic investigation indicates that the sediments have been affected by probably two, or may be more, stages of dissolution. The first stage probably occurred after the precipitation of the first calcite cement (discussed above) and prior to dolomitization. This is indicated by the presence of molds of large bivalve fragments (which were probably aragonite) and vugs which are filled by large blocky calcite crystals, interpreted as representing a second generation of calcite cementation. The fact that dissolution was not caused by meteoric waters, is discussed in sections 3.2.2 and 4.2.1. The second stage of dissolution occurred after or may be during dolomitization, probably as a result of brine reflux through the sediments. This caused the dissolution of the undolomitized parts of the matrix and allochems including fossil fragments and peloids, creating high intercrystalline and moldic porosity. Some of these pores and molds were either partially or completely occluded by the precipitation of sulfates (mostly gypsum), but many pores and molds remained open. This was probably either because the amount of sulfate was not enough to occlude all the porosity, or because these open pores represent dissolution at relatively later times.

4.1.3 Dolomitization

Dolomitization was the most important diagenetic event in the Beda Formation. In the area studied, 60-70% of the formation has been dolomitized. Petrographic investigation reveals that the dolomite generally occurs as a replacement of the $CaCO_3$ matrix, this was probably aragonite-dominated, because the Sr contents are high (see Chapter 3) which suggests

a Sr-rich aragonite precursor and where calcite cement is also present, the dolomite also replaces this calcite. The dolomite crystals are euhedral to subhedral and very finely to finely crystalline, generally less than .03 mm in diameter. Scanning electron microscope (SEM) examination shows the well developed rhombohedral form of these crystals, having smooth surfaces, it also shows the well developed intercrystalline porosity (Plate 4.3, A,B). Coarser dolomite crystals (up to 0.35 mm in diameter) are also present. These are generally rare and mainly occur as a pore-filling cement in molds and vugs (Plate 4.3, C,D). They have curved crystal faces and show undulatory (sweeping) extinction (termed saddle or baroque dolomite).

Under cathodoluminescence, most of the dolomite crystals have a uniform dull to moderately bright orange luminescence with no zoning, but samples from well F1 close to the western margin show a few crystals with faint zones, darker centers and brighter rims (Plates 4.3, E,F). This generally homogenous cathodoluminescence and lack of compositional zoning of the dolomite crystals may reflect replacement by a solution which remained uniform for some time (Folk, 1965) or homogenization from neomorphism (Sommer, 1972). Staining with potassium-ferricynide did not reveal the presence of Fe in the dolomite structure. This is because the iron concentrations of these dolomites are too low (less than 1 wt%, determined by XRFS) and it has been suggested (Lindholm and Finkelman, 1972) that such concentrations in the dolomite structure are too low to be detected by the staining technique.

4.1.4 Compaction

Compaction is a common diagenetic process in carbonate rocks and compactional processes are generally divided into two catagories; mechanical and chemical processes. Mechanical compaction begins soon after deposition whereas chemical compaction mostly requires several hundred metres of burial. Shallow burial compaction of the Beda sediments was probably prevented by early cementation of these sediments. This is indicated by the presence of bioclasts, birdseye fenestrae and peloids, none of which show signs of compaction, retaining their original shapes. Chemical compaction and pressure dissolution are common in the Beda sediments and two styles of pressure dissolution response are recognized, stylolites, and dissolution seams. These are equivalent respectively, to the sutured-seam solution and the non-sutured seam solution of Wanless (1979).

Stylolites occur locally and are particularly present in the foraminiferal wackestone facies (F1) in wells E2 and G41 and also present in facies 3 in well F1 (see Chapter 2, Fig.). They are irregular with low-very high amplitude seams, interpenetrating the matrix and occasionally affecting skeletal grains (Plate 4.4, A-D). Dissolution of matrix and grains led to the accumulation of black insoluble residues, concentrated along stylolite surfaces. Dissolution seams are relatively more common in the studied intervals than stylolites. They are mostly unserrated except for some micro-stylolites, and form irregular seams of brown to black insoluble residue. They generally occur in swarms forming horsetail structures which mostly pass around and between skeletal grains, rather than cutting them, and locally, forming swarms wrapping over carbonate nodules (Plate 4.4, E,F).

Chemical compaction and pressure dissolution involve the reduction of the bulk volume of the sediments with a resultant loss in porosity (Rittenhouse, 1971), coupled with reprecipitation of the dissolved $CaCO_3$ as a cement either in the immediate vicinity or in a more distant site, carried away in an active pore-fluid system (Bathurst, 1984; Scholle and Halley, 1985). A number of authors have argued that this is a significant source of $CaCO_3$ for burial cementation.

4.1.5 Mineralization

A very late stage of burial diagenesis is represented locally by the occurrence of some Pb-mineralization in the molds of dissolved fossil fragments (Plate 4.5). Figure 4.2, shows the EDX analysis of this mineral. This mineralization was probably caused by the circulation of hydrothermal fluids through the sediments, since the area has been affected by some more recent volcanic activity (Chapter 1).

4.2 Dolomitization Model

There are two major considerations in the formation of dolomite (1) the source of the magnesium (Mg^{2+}) ions and (2) the process whereby the dolomitizing fluid is pumped through the carbonate sediments. These considerations will be discussed in the forthcoming sections, starting by discussing the source of magnesium and then the interpretation of the dolomitization model.

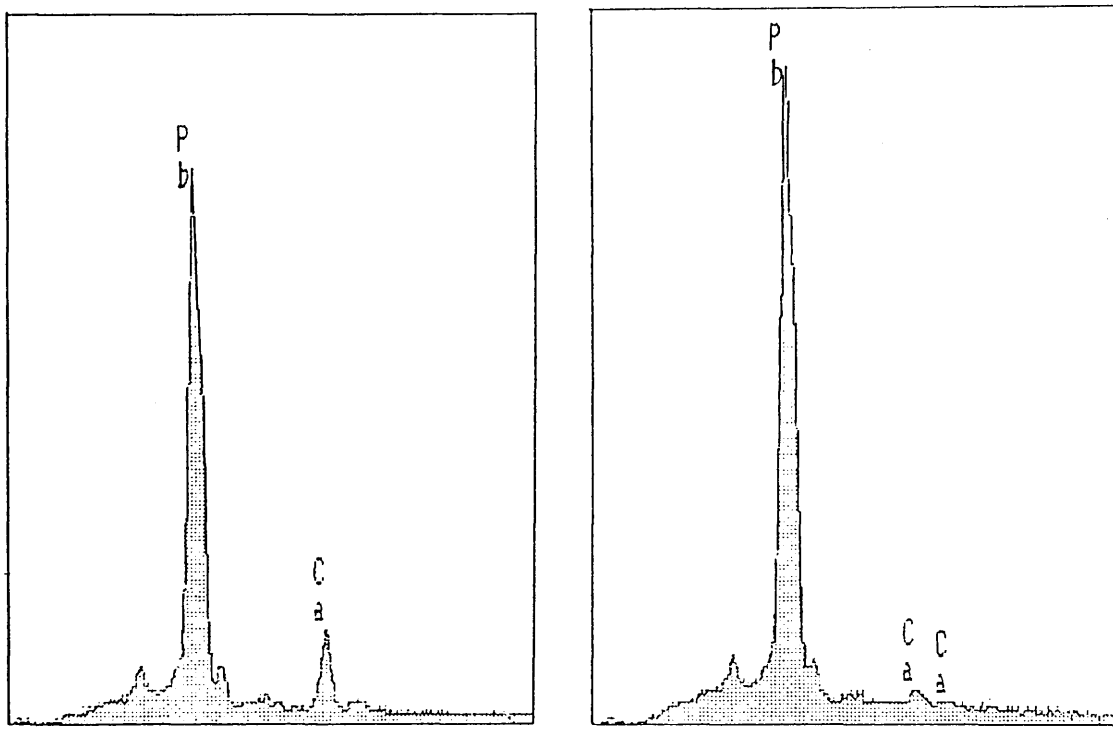

Fig. 4.2, EDX spectrum showing a lead peak. Left and right spectra are respectively, the result of the analysis of the bright areas shown by the arrow on the back-scattering photomicrographs A and B of Plate 4.5.

4.2.1 Magnesium Source

Potential magnesium sources were divided into static and non-static sources by Given and Wilkison (1987). Static sources comprise magnesium-enriched rocks, including shales and some carbonates (magnesian calcite), and nonstatic sources comprise earth surface fluids that are continually replenished in magnesium, including meteorically derived subsurface fluids, marine-derived subsurface fluids, and seawater.

1) Static Sources

Shales are considered the most magnesium-rich, noncarbonate sedimentary rock type which might serve as an important source of magnesium. One possible process that could liberate significant shale-related magnesium is the transition from smectite to illite, which may liberate enough magnesium to dolomitize adjacent carbonate (e.g. Morrow, 1982). The importance of this process as a source of magnesium for dolomitization was questioned by Land (1985), because the smectite-illite transition is accompanied by the release of more calcium than magnesium, and the magnesium released is consumed in the formation of chlorite, a common diagenetic mineral (Hower et al., 1976). However, this source cannot be important in this study because only thin shales (less than a metre thick) are observed in the studied interval of the Beda Formation, and apart from these, the only clay-minerals present occur as authigenic clays.

The other possible rock-reservoir source of magnesium for dolomite formation is the initial magnesium incorporated in magnesian calcite or Mg-calcite. With time, the Mg-calcite loses its Mg and is converted into calcite. The importance of this source depends both on the initial composition of the Mg-calcite and on the amount of this material in an average carbonate sediment. In general, the average shallow-marine carbonate contains approximately 30% $MgCO_3$ (e.g. Drever, 1974; Milliman, 1979). The sediments of the Beda Formation represent shallow-marine carbonates with dominant benthonic foraminifera which contain $MgCO_3$ in the range 0-15 mol% $MgCO_3$. These values indicate that little dolomite could originate through the release of magnesium from magnesian calcite.

2) Nonstatic Sources

The nonstatic sources of magnesium, mentioned above, are also variable and of these sources, seawater is considered the only abundant source of Mg^{2+} ions for early diagenetic surface and near-surface dolomitization. It contains 1290 ppm Mg and 411 ppm Ca, and by way of contrast, meteoric water, although variable, has much lower values of magnesium and calcium (e.g. average river water has 4 ppm Mg and 15 ppm Ca). However, dolomite rarely precipitates out of normal seawater, probably for kinetic reasons (Lippman, 1973; Morrow, 1982a), and most authors advocate somewhat modified seawater as being a more effective dolomitizing agent than unaltered seawater. Thus seawater, modified in the various dolomitization models in vogue, is considered the primary agent responsible for the formation of the vast quantities of dolomite in the rock record (Morrow, 1982; Land, 1983). In this study, the Beda dolomite has

a high Sr content, which is sufficient evidence for rejecting fresh water diagenesis and also negates the possibility of meteoric-marine water mixing which normally results in Sr depletion (Bein and Land, 1983). It suggests that the most likely source of magnesium for the formation of this dolomite was seawater and marine derived brines.

4.2.2 The Model

Different models of dolomitization have been proposed for carbonates physically and/or genetically related to evaporites. These include; an evaporitic (sabkha) origin (e.g. McKenzie, 1981; Patterson and Kinsman, 1982), deposition from precipitating brines (e.g. Friedman, 1980; Bein and Land, 1983), and the mixing zone of saline with meteoric water (e.g. Magaritz, 1980 and 1987).

The sedimentological, petrographic, and geochemical evidence from the Beda dolomite in this study, includes the fine grained nature of the rhombs, the high Sr content, the low Fe and Mn concentrations, and the association of this dolomite with fenestral structures, stromatolites and calcium sulfates (gypsum-anhydrite). These together indicate an early, near-surface dolomitization associated with a hypersaline setting, which was generated through the restriction of marine water circulation and the evaporation of the resulting lagoon water. This caused an increase in salinity and the precipitation of calcium sulfates and as a result raised the Mg/Ca ratio and increased the density of the evaporated water. Consequently, the dense Mg^{2+}-rich hypersaline brine infiltrated the

underlying aragonite muds, displacing less dense marine pore water and eventually dolomites were precipitated.

Dolomitization of $CaCO_3$ by reflux of hypersaline brines was first proposed by Adams and Rhodes (1960) to account for Permian reef dolomites associated with evaporative lagoonal deposits. Recently, Simms (1984) has demonstrated that even waters of slightly elevated salinity, such as those covering the Bahama Bank today, are capable of reflux. In modern settings, the model was applied by Deffeyes et al. (1965) to studies of a supratidal, gypsum-precipitating lake (the Pekelmeer) on Bonaire. However, later work by Lucia (1968) and Murray (1969) showed that there are no dolomites beneath the Pekelmeer. Although there seem to be no good modern analogues, the model has frequently been applied to ancient dolomites associated with evaporites.

Although one would expect the dolomites formed in such settings to be relatively enriched in ^{18}O isotopes as a result of precipitation from evaporated seawater, the $\delta^{18}O$ isotope data from the Beda dolomite are quite negative, and the $\delta^{13}C$ has a more normal marine value (see section 3.2.2). Similar isotopic values have been reported from the ancient dolomite in the Upper Devonian Miette Buildup (Mattes and Mountjoy, 1980). However, trace elements (e.g. Sr: 30-100 ppm) in the Miette dolomites are low and they have been interpreted as of burial origin. A second example from the Triassic Latemar dolomite (Wilson et al., 1990), has values for $\delta^{18}O$ which vary from -1.85 to -9.57 per mil (PDB) and the $\delta^{13}C$ vary from 1.57 to 4.1 per mil (PDB). Wilson et al. (1990) suggested that hydrothermal circulation of warm to hot seawater resulted in the production of the mushroom shaped dolomite body, and the oxygen

isotope values in particular indicate that a strong thermal gradient was present during dolomitization.

The study area has been affected during the Quaternary (and probably very recently) by volcanic activity represented by the Al Haruj Al Aswad formation. Thus, the baroque dolomite, together with the lead mineralization probably reflect higher (deeper burial) temperatures. In addition, the negative $\delta^{18}O$ isotope values of the Beda dolomite in general may indicate a late neomorphism of this dolomite by hydrothermal circulation of warm to hot connate water rather than deep burial dolomitization, since all other evidence mentioned above indicates an early, near-surface dolomitization. There is, however, no petrographic evidence of such replacement which may only be reflected in the diffusion of lighter ^{18}O.

Plate 4.1

A,B) Photomicrographs showing fibrous calcite cement growing on the walls of foraminifer in A, and ostracod in B. The crystal size increases away from the walls. Scale bar = 0.1 mm. A) PPL. B) XPL.

C) Photomicrograph showing intergranular porosity partially filled with calcite cement. The calcite crystals increase in size inward into the pore space (arrow). Scale bar = 0.1 mm. PPL.

D,E) Photomicrographs showing blocky calcite crystals (arrow) in vugs. Scale bar = 0.2 mm. D) XPL. E) PPL.

F) Photomicrograph showing calcite overgrowth (arrow) on echinoderm fragment (a). Scale bar = 1 mm. XPL.

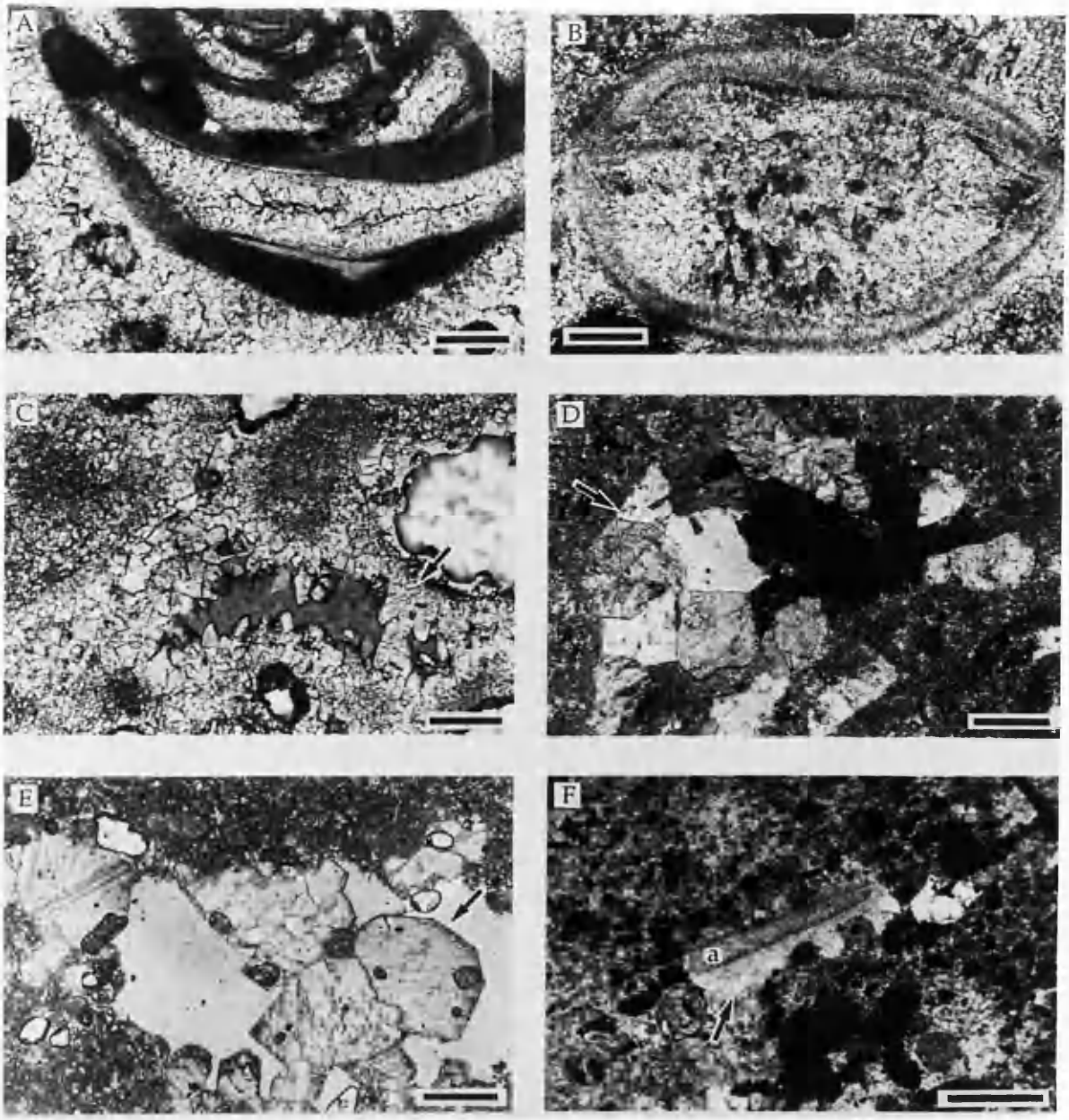
A
B
C
D
E
F
a

Plate 4.2

A) Photomicrograph showing poikilotopic gypsum crystal (white area in the middle of the photograph) engulfing the matrix. Scale bar = 0.2 mm. PPL.

B) Photomicrograph showing poikilotopic gypsum crystal (white areas) engulfing peloids (arrow). Scale bar = 1 mm. XPL.

C) Photomicrograph showing poikilotopic gypsum crystal (the whole field of view) engulfing bioclasts and filling large bivalve fragments (a). The black mold of foram (b) is also gypsum (different orientation of extinction). Scale bar = 1 mm. XPL.

D-E) Photomicrographs showing gypsum cement (a) postdates calcite cement (b). Note the shape of the contact (arrow) between the gypsum and calcite. D) Scale bar = 0.1 mm. E) Scale bar = 0.2 mm. XPL.

F) Photomicrograph showing mold of dissolved bioclast with calcite crystals (arrow) formed along the wall and residual pore filled with gypsum (a). Scale bar = 1 mm. XPL.

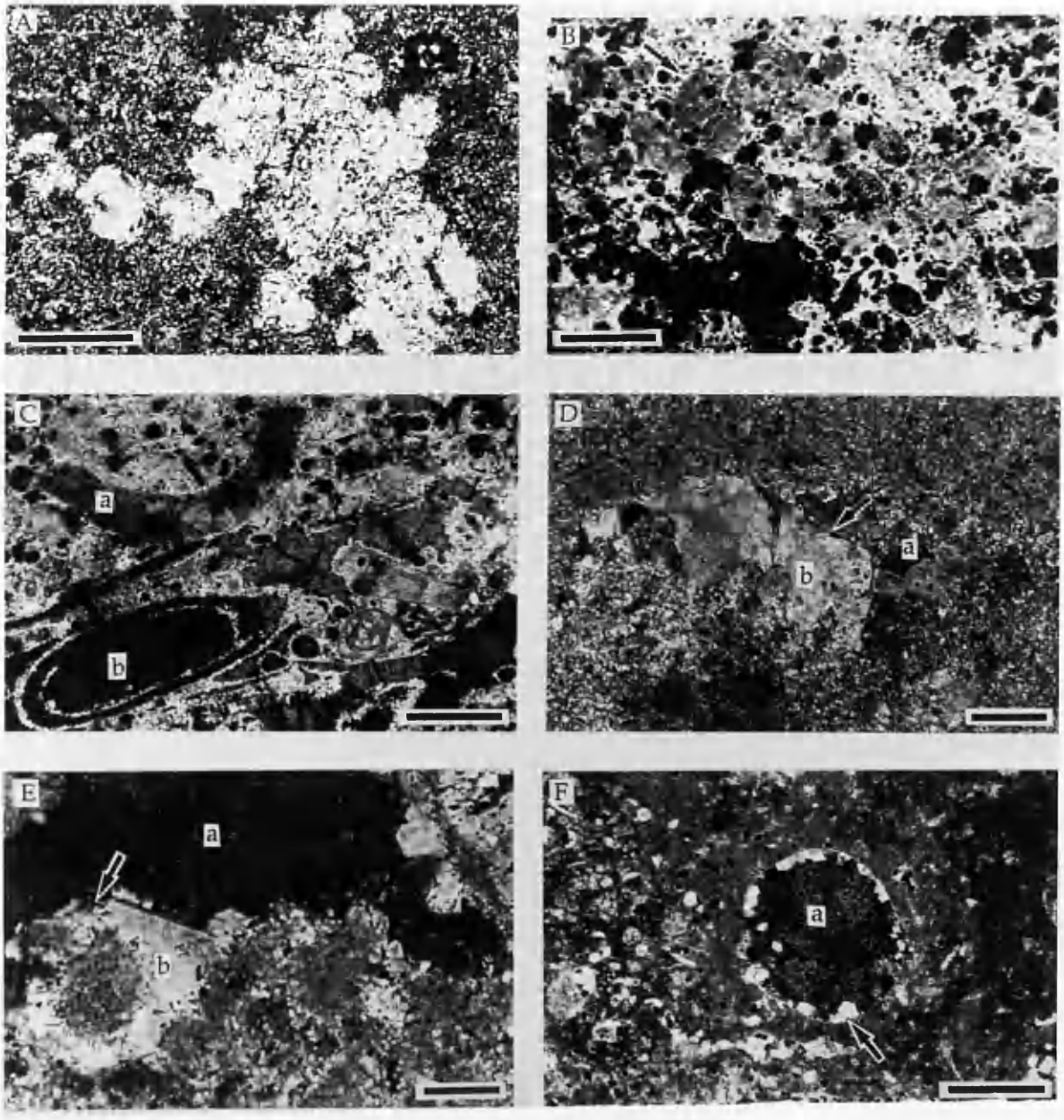
A
B
C
a
b
D
a
b
E
a
b
F
a

Plate 4.3

A,B) SEM photomicrographs showing euhedral dolomite crystals of facies 3. They also show good intercrystalline porosity.

C) Photomicrograph showing two coarse baroque dolomite crystals. Scale bar = 0.1 mm. XPL.

D) Back-scattered photomicrograph showing the same as C.

E,F) Photomicrograph of dolomite crystals under cathodoluminescence. The dolomite crystals generally have single zone with bright rim and dark center. Some crystals have two zones (arrow). E) Scale bar = 0.2 mm. F) scale bar = 0.1 mm.

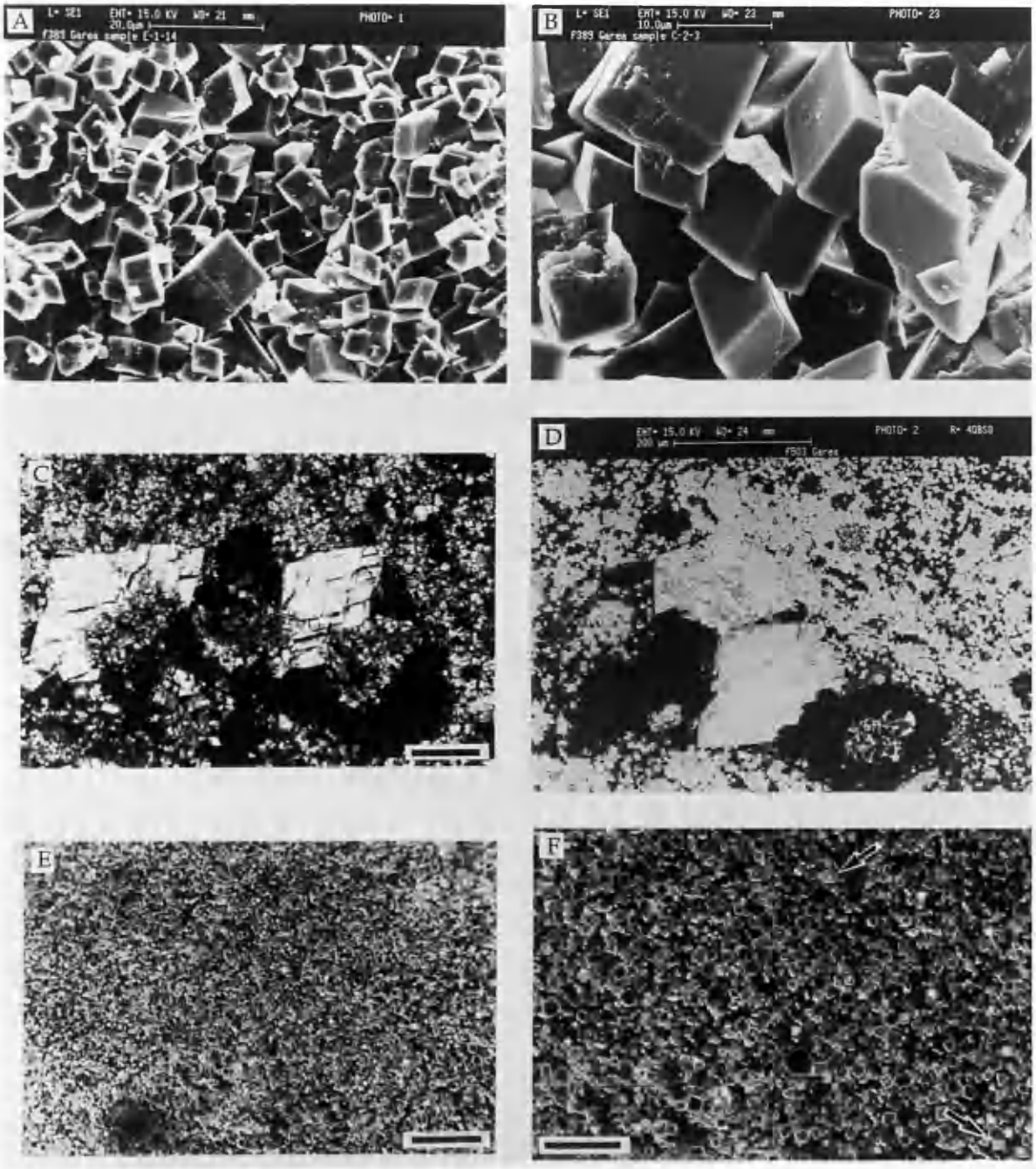
A
B
C
D
E
F

Plate 4.4

A) Slabbed core sample showing high and low amplitude stylolites with black insoluble residue (arrow) concentrated along their surfaces. Scale bar = 2 cm. PPL.

B) Photomicrograph showing the same as A. Scale bar = 1 mm. PPL.

C.D) Photomicrographs showing pressure dissolution and microstylolites penetrating the matrix and cutting through foraminiferan grain (arrow). Scale bar = 1 mm. PPL.

E) Slabbed core sample showing horsetail dissolution seams. Scale bar = 2 cm.

F) Slabbed core sample showing pressure dissolution (a) forming swarms wrapping over carbonate nodules (arrow). Scale bar = 2 cm.

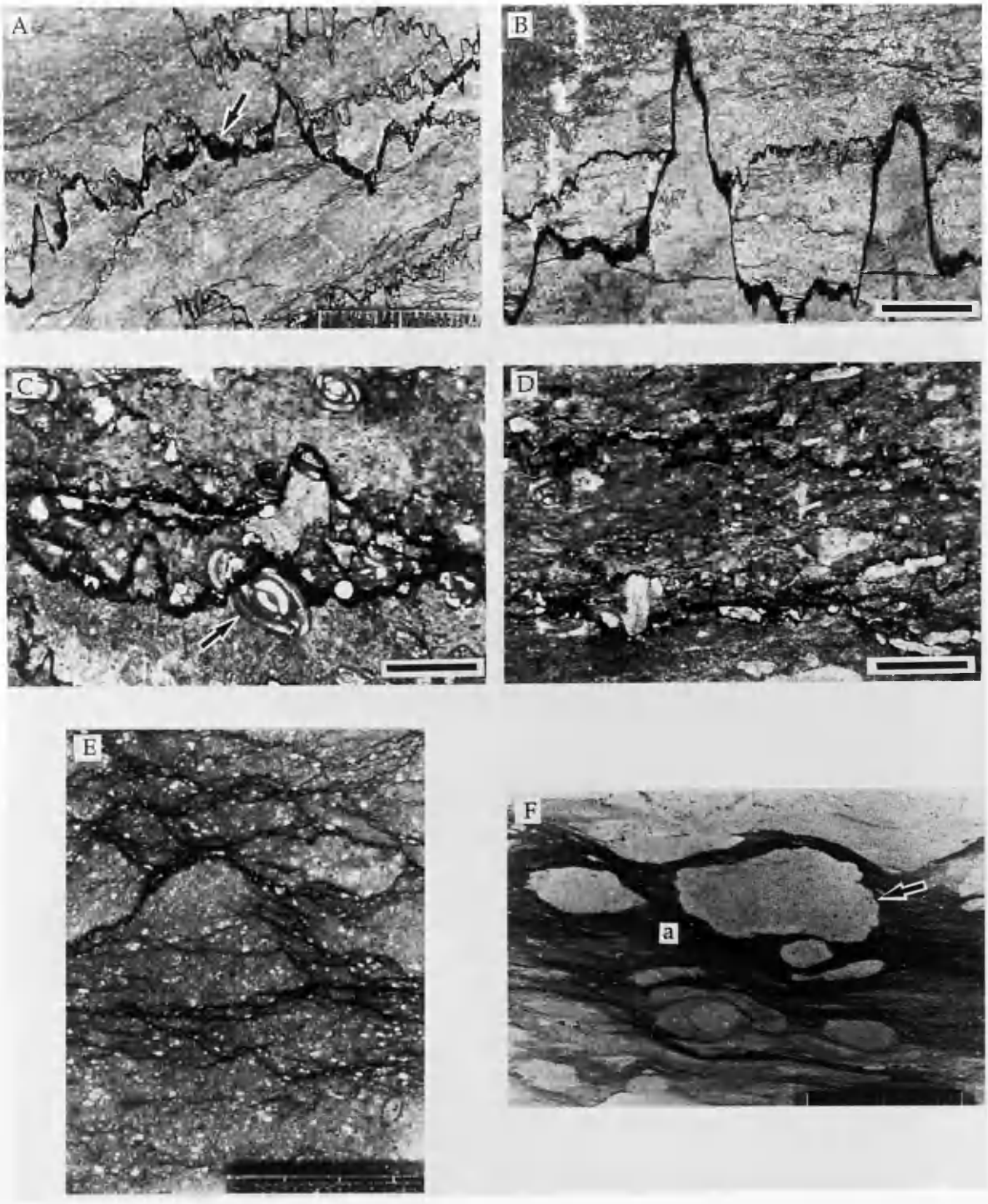
A
B
C
D
E
F
a

Plate 4.5

A,B) Back-scattered photomicrograph showing lead mineralization (bright areas of the photograph) in molds.

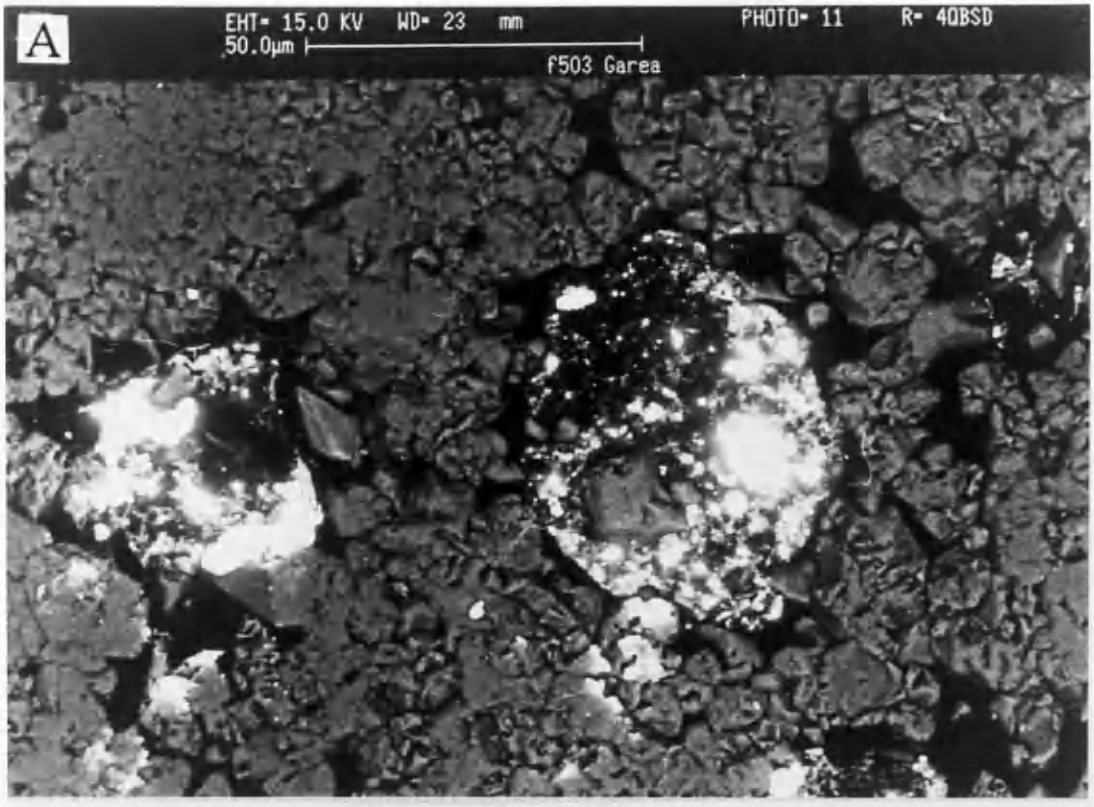
A
EHT= 15.0 KV WD= 23 mm
50.0µm
PHOTO= 11 R= 4QBSD
f503 Garea

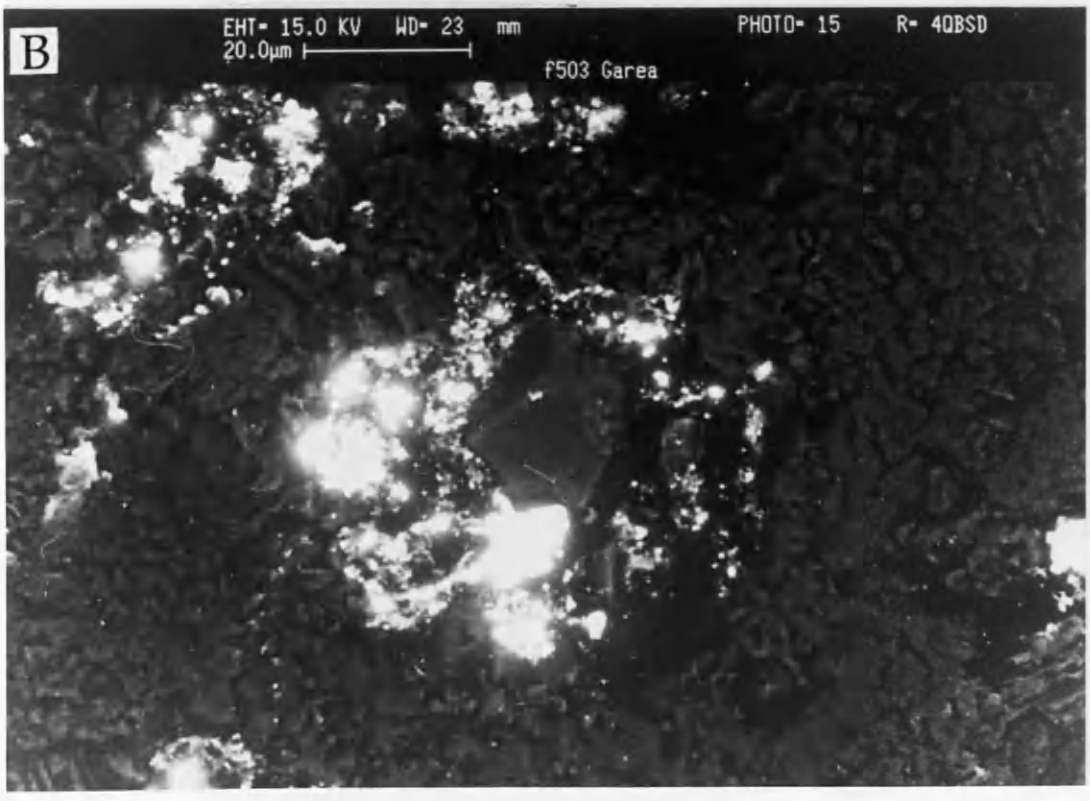
B
EHT= 15.0 KV WD= 23 mm
20.0µm
PHOTO= 15 R= 4QBSD
f503 Garea

CHAPTER FIVE
POROSITY ANALYSIS

From the previous chapter, it is clear that the porosity development in these rocks was the result of a number of diagenetic processes that can be divided in terms of their relative effect on porosity into those related to porosity enhancement, including dolomitization and dissolution, and those related to porosity destruction, including cementation and perhaps compaction. In this chapter quantitative analyses of this porosity will be made, using a number of porosity wireline logs, including density, neutron, and sonic logs.

Wireline logs have become increasingly important, in subsurface studies, as a complementary tool to the geological data obtained from core samples. They can give a nearly continuous analysis of the drilled formation and can also provide information on the petrophysical characteristics such as porosity and permeability, of a formation.

In the study area a number of porosity logs have been recorded through the Beda Formation, and these logs (from wells A1, E2, F1, D2, G41, and G4) were utilized to quantitatively determine the porosity percentages, including total porosity and the isolated pore spaces, of the studied intervals of this formation. However, no attempt has been made to measure the permeabilities of these intervals, because of the lack of core samples large enough to make the plugs necessary for such measurements.

5.1 Method of Analysis

A complete package of porosity logs, including neutron and density (LDL-CNL) logs, and sonic (LSS or BHC) logs has been recorded in the study area. The neutron log measures the hydrogen concentration in a formation and therefore indirectly measures liquid-filled porosity, whereas, the formation density log measures the electron density of the formation by use of a gamma source. Both neutron and density curves are normally recorded in limestone porosity units (e.g, porosity = 0 at limestone matrix = 2.71 g/cc). Besides being essential tools in measuring the total porosity of a formation, the neutron and density logs are also used in cross plots with sonic logs to determine the mineralogical composition of the rock.

Sonic logs, measure the interval transit time (ΔT) of a compressional sound wave travelling through one foot of formation and are often run combined with electrical logs (measuring resistivity). The interval transit time (ΔT) is dependent upon both lithology and porosity, and therefore the matrix interval transit time (ΔTma) of a formation must be determined to derive sonic porosity (Wyllie et. al., 1958). The sonic derived porosity represents the matrix (connected pore spaces) porosity rather than the isolated pores. Therefore, when used with neutron-density logs, the percentage of isolated pore spaces can be determined. Sonic logs, in addition to their value as a porosity tool, are also very useful in well to well correlation (see Fig. 2.3).

5.2 Log Correction

Before any analysis is undertaken, the recorded logs; neutron, density, interval transit time and gamma-ray curves, of each well are depth-matched with each other. Since most modern logs are borehole compensated devices, most of the corrections necessary because of borehole irregularities, have been automatically applied during the logging operation and the effects of borehole size variations are greatly reduced (Schlumberger,1972).

Generally, most of the calliper logs across the relevant part of the Beda Formation show no significant borehole size variations except in two wells, F1 and D2. In these wells the calliper logs show enlarged hole sizes across the intervals 1766 to 1772 m (5794-5812 ft) in F1 and 1802 to 1809 m (5912-5936 ft) in D2. However, no clear explanation can be made from these logs and the log readings from these intervals are probably affected by this hole enlargement. In addition, no corrections have been applied to the neutron log, for salinity, mud cake thickness or temperature, since the overall correction is usually quite small (Schlumber-ger,1972).

In general, the amount of error in porosity values is not of much concern here, because this study is concerned more with the presence and distribution of porosity rather than with specific values.

3.3 Procedure

Twelve porosity logs from six wells in the study area were analyzed for porosity determination. More than 30 meters (≈110 feet) of interval per log were read on a one-foot increment and the data from each well were analyzed using Cross-plotting techniques and mathematically solved equations (Appendix B). A computer programme is written to solve these equations (Appendix C).

All these porosity logs; neutron, density and sonic logs were used to quantitatively determine both total ($\emptyset_{ND}$) porosity and sonic derived porosity ($\emptyset_S$), and the secondary porosity index (SPI). Here the total porosity ($\emptyset_{ND}$) represents the matrix (connected pore spaces) porosity plus the isolated pores of the formation and the sonic porosity ($\emptyset_S$) represents the matrix porosity only. The secondary porosity index (SPI) represents isolated pore spaces.

The calculation of density porosity and sonic porosity requires that the matrix density (ρ ma) and the interval transit time of the matrix (ΔTma) of a formation be identified. The standard approach adopted to identify these matrix parameters is (1) by cross plotting the formation density and neutron points, read off respectively from the density log and the neutron log, on a neutron-density crossplot (Fig. 5.1), and (2) by cross plotting the interval transit time (ΔT) and neutron points, read off respectively from the sonic log and the neutron log, on a neutron-sonic crossplot (Fig. 5.2). These respectively, identify the (ρ ma) and (ΔTma) of a formation. The resulting matrix parameters of each well are listed in Table 5.1.

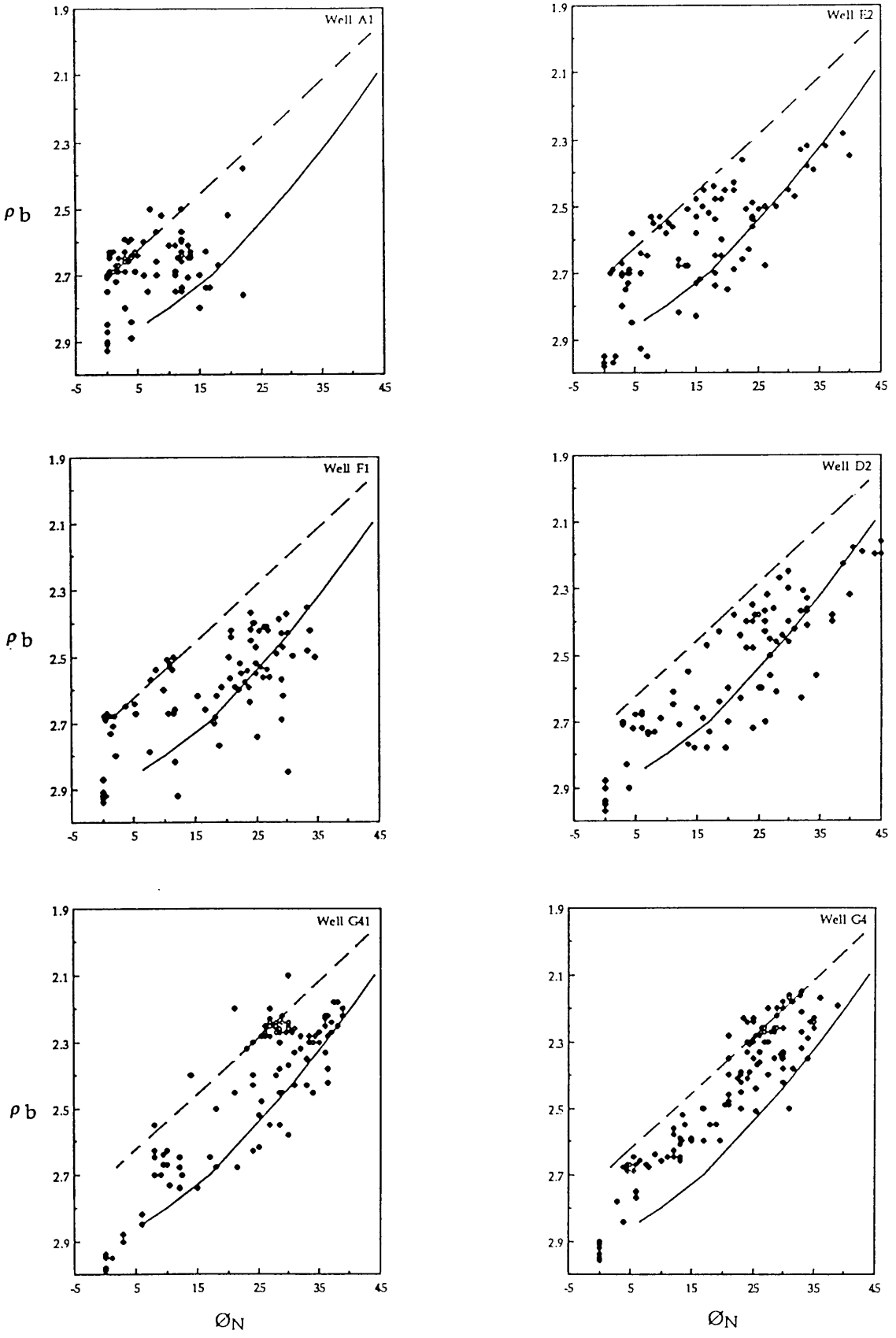

Fig. 5.1, Bulk density (ρ_b) versus neutron porosity ($\emptyset_N$) crossplots for determining the apparent (ρ_{ma}). Limestone line (dashed), dolomite line (solid).

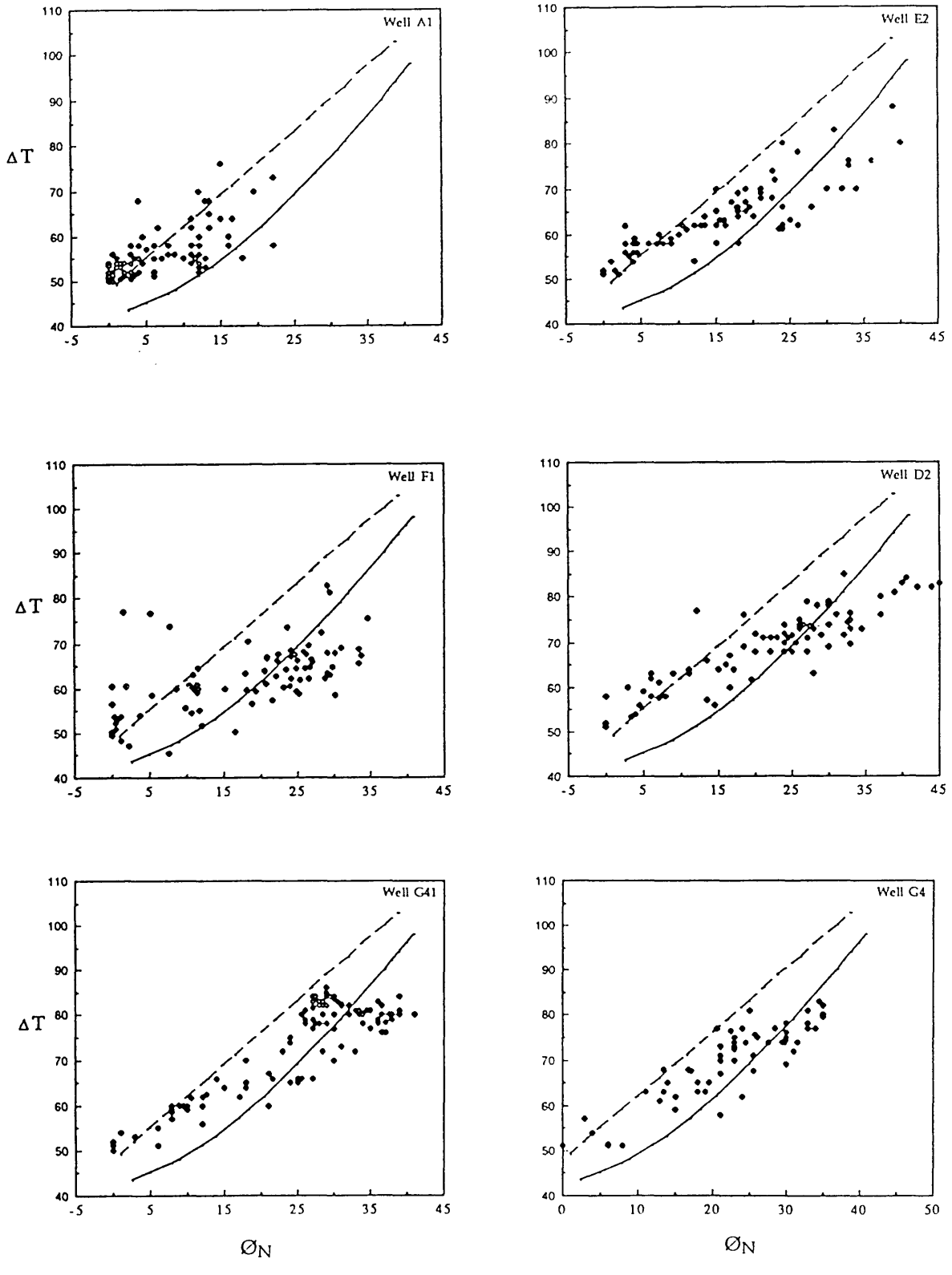

Fig. 5.2, Interval transit time (ΔT) versus neutron porosity ($Ø_N$) crossplots for determining the apparent (ΔTma). Limestone line (dashed), dolomite line (solid).

These matrix parameters; ρ ma and ΔTma are used with other parameters such as fluid density and interval transit time of the fluid to calculate the density, porosity ($\emptyset_D$) and the sonic porosity ($\emptyset_S$) respectively. The calculated density porosity values are then used to calculate the total porosity ($\emptyset_{ND}$) percentages. The secondary porosity (SPI) values are calculated by subtracting the sonic porosity ($\emptyset_S$) from the total porosity values (appendix B). Figures 5.3-5.5, illustrate the total ($\emptyset_{ND}$) and sonic ($\emptyset_S$) porosity percentages plotted at their respective depths .

Well Number	ρ ma	ΔTma
A1	2.71	47.6
E2	2.88	45.5
F1	2.88	43.5
D2	2.88	43.5
G41	2.86	45.0
G4	2.77	46.0

Table 5.1, values of matrix density and interval transit time of the matrix.

3.4 Results

The porosity plots show vertical changes in porosity development, subdividing the studied interval of the Beda Formation into two porous units; Unit 4 and Unit 2, separated by a low porosity unit; Unit 3. The uppermost unit, Unit 2, of this interval is capped by a further unit, unit 1,

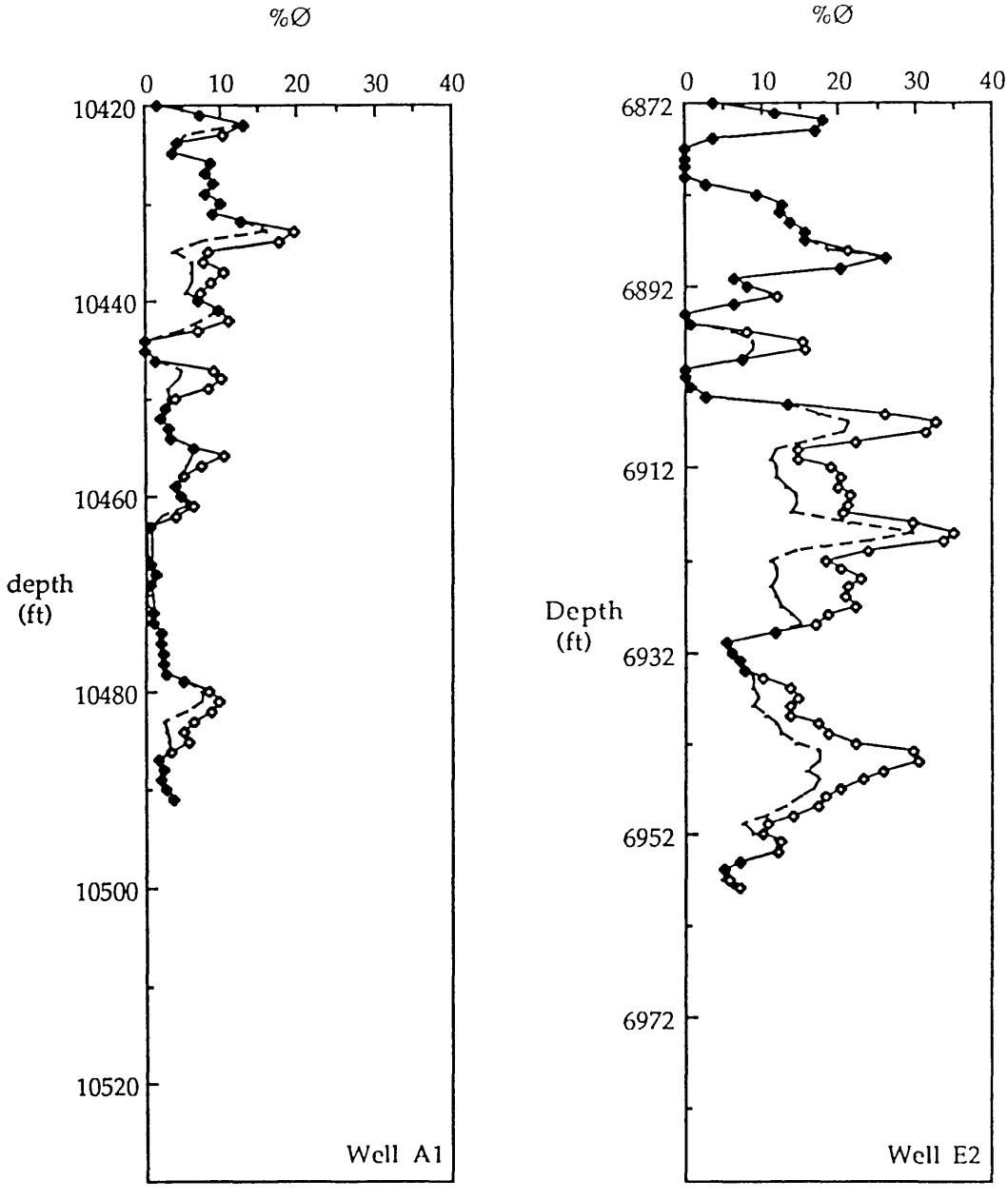

Fig. 5.3, Porosity distribution with depth, wells A1 and E2. It presents the total ($Ø_{ND}$) porosity (diamonds) and sonic ($Ø_S$) porosity (dashed).

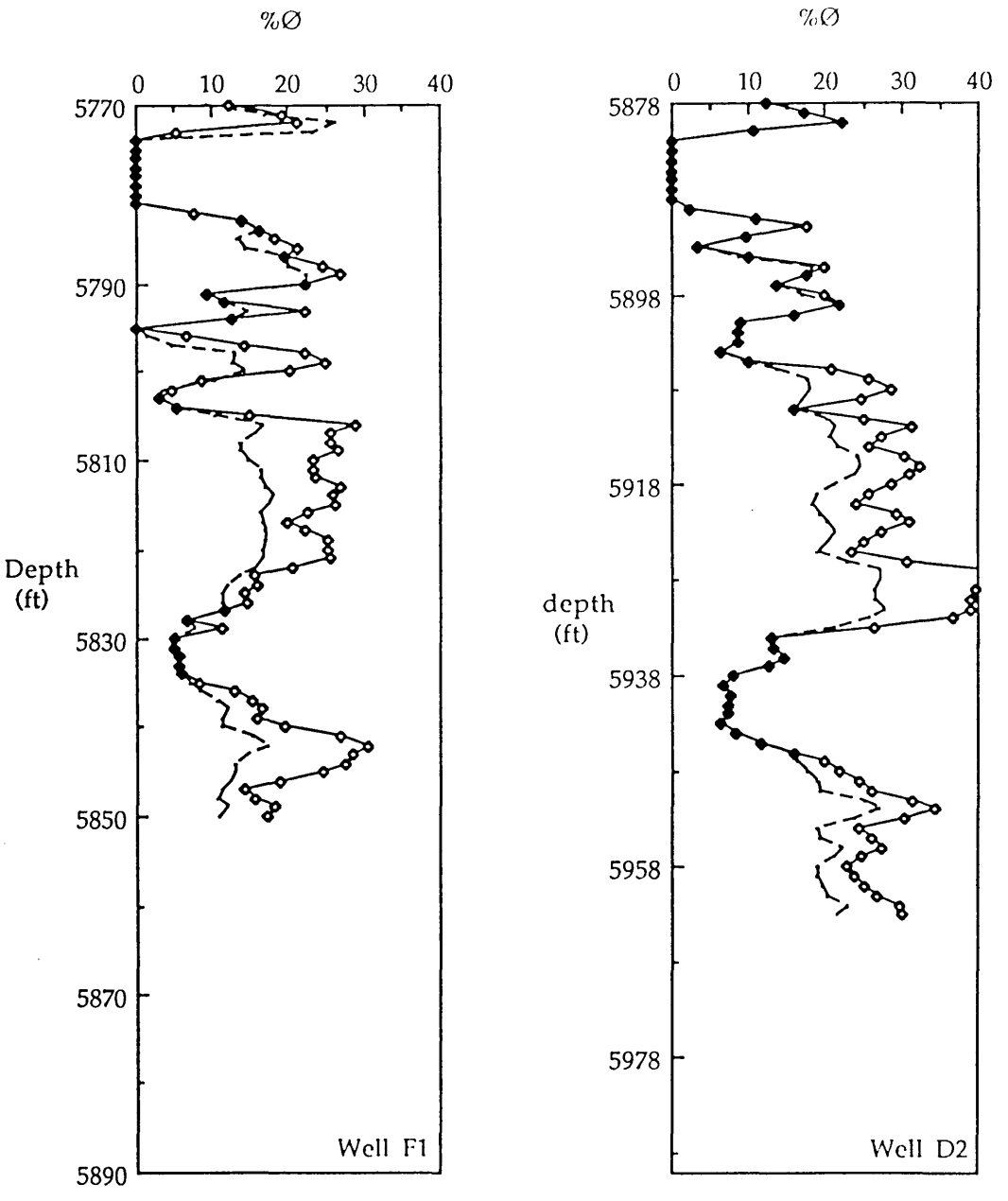

Fig. 5.4, Porosity distribution with depth, wells F1 and D2. It presents the total ($Ø_{ND}$) porosity (diamonds) and sonic ($Ø_S$) porosity (dashed).

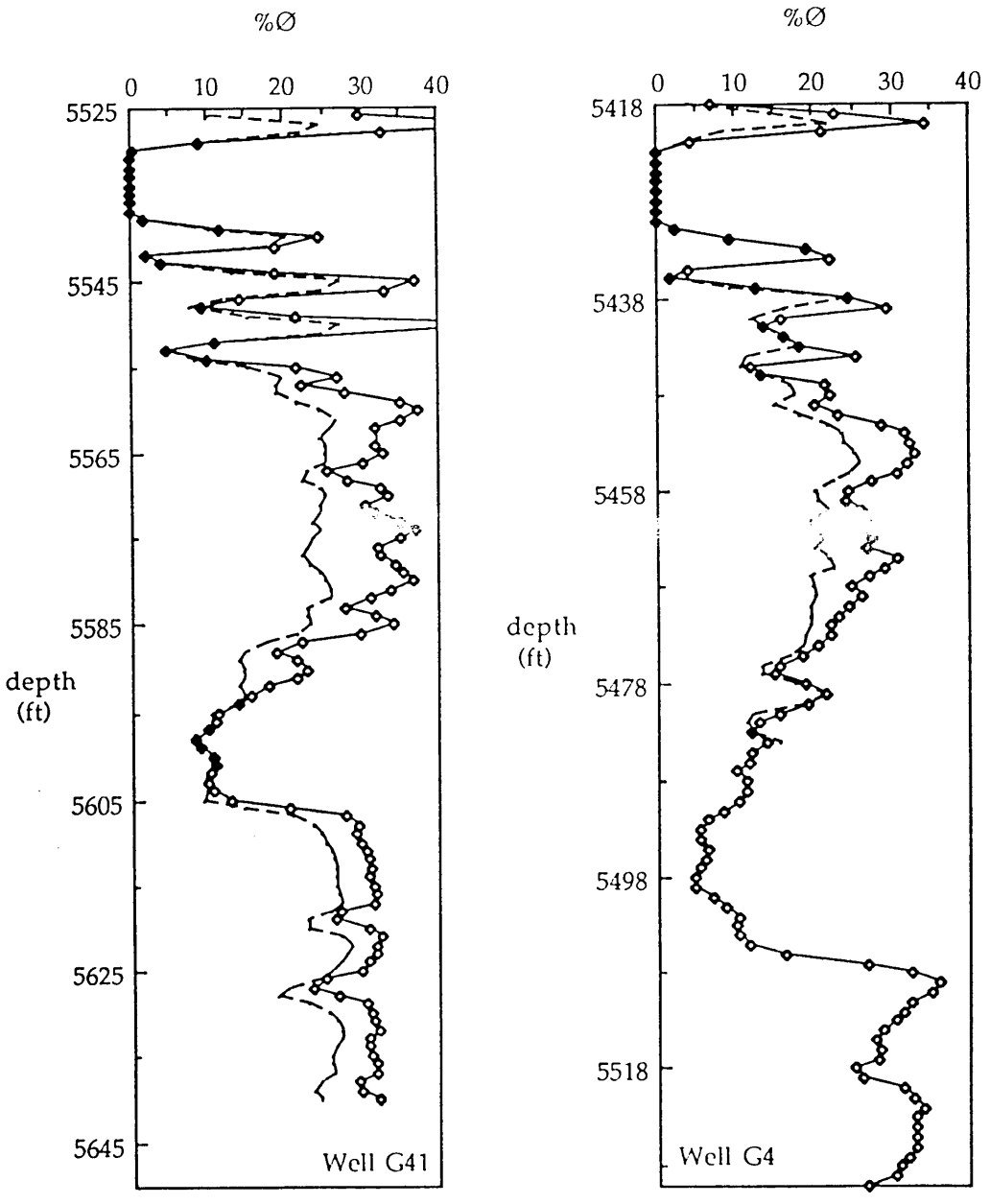

Fig. 5.5, Porosity distribution with depth, wells G41 and G4. It presents the total ($Ø_{ND}$) porosity (diamonds) and sonic ($Ø_S$) porosity (dashed).

which is dominated by sulphate and dolomite interbeds, very argillaceous and exhibiting variable porosity values. Laterally, these units are easily correlated and they show some lateral changes in porosity, which are shown by a southwest-northeast oriented cross-section (Fig. 5.6). This cross-section shows that in all three units there is a rapid increase in porosity between wells A1 and E2 and then, northeastwards from E2, the porosity generally increases but with a gentler gradient. The highest porosity values are recorded from wells D2, G41 and G4. The average total ($Ø_{ND}$) porosity percentages of the Beda Formation shows wide range of variations, ranging between less than 1% to approximately 30%, and the average porosity percentages of the main three units; units 2, 3 , and 4, of this interval are shown in Table 5.2.

Unit No.	A1	E2	F1	D2	G41	G4
Unit 2	5.8	21	23.5	28.3	29.9	26.2
Unit 3	0.9	8.2	8.8	10.4	11.2	11.5
Unit 4	4.4	14	20.6	26.5	30.3	31.7

Table 5.2, summarizing the average porosity percentages.

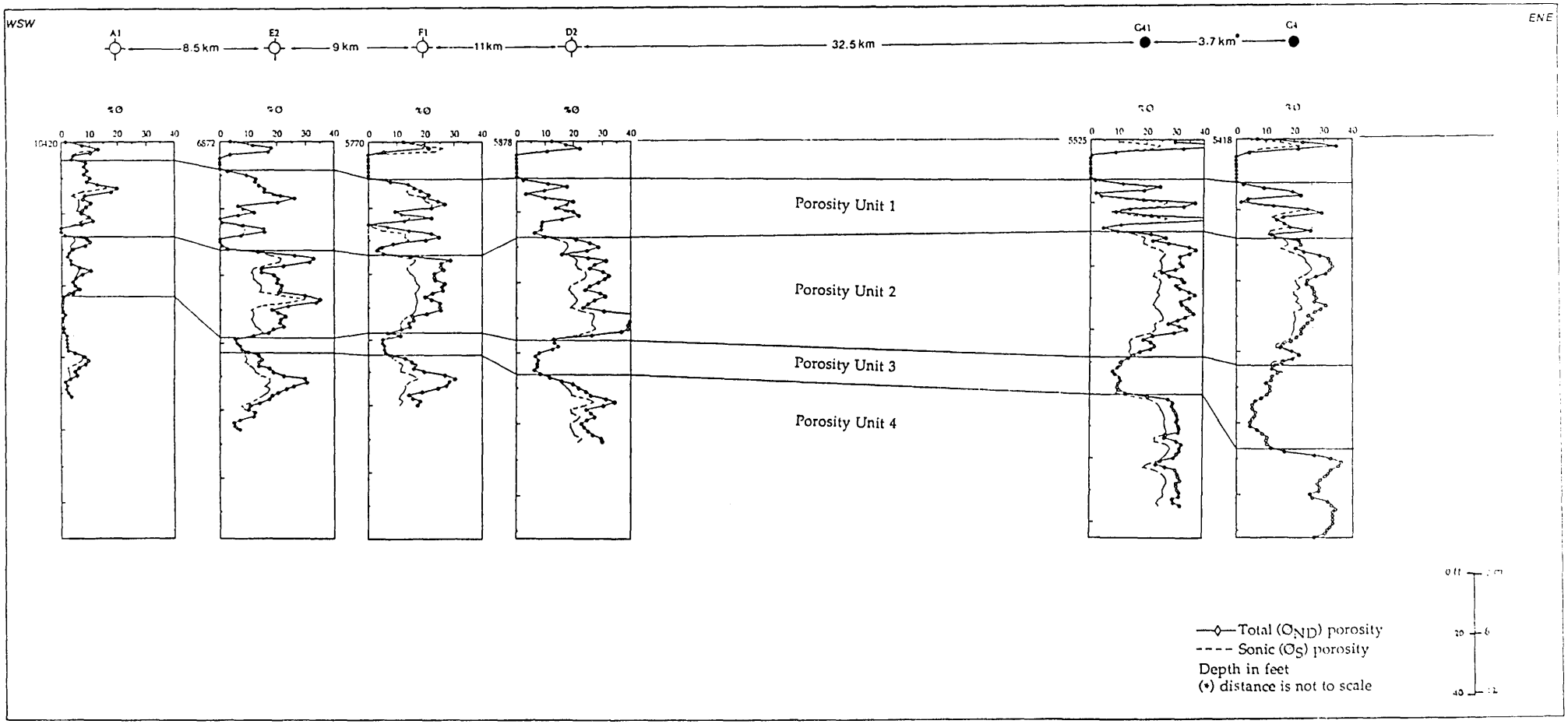

Fig. 5.6, WSW-ENE stratigraphic cross-section, showing lateral distribution and variations of porosity over the study area.

CONCLUSIONS

From the evidence and discussions presented in the different sections of this study, a number of concluding points are accomplished. These are summarized below.

1- A total of six lithofacies have been described from the studied part of the Beda Formation in the study area. These are (1) foraminiferal wackestone, (2) argillaceous foraminiferal wackestone, (3) dolomite mudstone, (4) Peloidal-foraminiferal wackestone, (5) evaporite; gypsum-anhydrite, and (6) argillaceous dolomite mudstone. These lithofacies are interpreted as having been deposited in a semi-open to restricted and hypersaline lagoon, dominated by intertidal and supratidal sediments.

2- The facies reflect three small-scale shallowing-upward cycles, probably formed as a result of either differential subsidence or differential accumulation of sediments, and/or sea level changes.

3- A sequence of significant diagenetic changes are inferred from petrographic observations. These diagenetic changes vary from early fibrous calcite cement growth through dissolution of aragonite and the growth of blocky calcite to dolomitization and the growth of sulfates cements to late diagenetic changes such as compaction, development of baroque dolomite cement, and Pb-mineralization.

4- The association of the Beda dolomite with evaporite sulfates, the fine grained rhombic character of the crystals, the high Sr contents, and the

low Fe and Mn concentrations, all indicate that dolomitization took place during early and near-surface diagenesis, as a result of hypersaline brine refluxion.

5- Oxygen isotope analyses indicate that this dolomite is depleted in ^{18}O and has negative $\delta^{18}O$ values. These values contradict values expected from dolomite occurring in evaporative environments. This oxygen isotopic change of the Beda dolomite towards negative $\delta^{18}O$ values is interpreted as suggesting a late neomorphism which has been caused by hydrothermal circulation of warm to hot fluids, resulting from the occurrence of volcanic activity in the area.

6- Anomalously high Sr have been measured by XRFS. These are interpreted as having been caused by celestite precipitation.

7- Porosity in the studied part of the Beda Formation is generally secondary porosity created by dolomitization and dissolution, and it was partly reduced by cementation and replacement. This porosity increases in an east-northeastward direction with the highest porosity values occurring in wells D2, G41, and G4, where porosity has been less affected by sulfates cements relative to wells E2 and F1.

FUTURE WORK

During the course of this study some assumptions have been made, and in the light of the present data, these assumptions are valid. However, further investigations need to be made. These include (1) The development of a barrier controlling deposition in the area. What type of barrier could this have been and where was it in relation to the study area?. (2) Were the negative oxygen isotope values of this study influenced by meteoric water input, or were they simply the result of high temperatures?. To answer these questions, the following studies are intended to be made:

1- A number of cores from wells outside the study area will be investigated. This investigation will include the sedimentology and petrography of the Beda Formation in these wells. Regional well to well correlation will then be made to determine facies changes and map their lateral distribution.

2- Sr isotope analyses (a few samples are currently under investigation at SURRC) will also be important to verify the source of the strontium, because variations in the $^{87}Sr/^{86}Sr$ ratios record changes in the geology of the drainage basin such as volcanic activity.

3- The analysis of oxygen and hydrogen isotopes of formation waters is also desirable. This would be to investigate the source of the fluid and to find out if there was meteoric water input, which might have influenced the oxygen isotope composition.

REFRENCES

Andrews, J. E., Hamilton, P. J., and Fallick, A. E. (1987). The geochemistry of early diagenetic dolostones from a low-salinity Jurassic lagoon. Jour. Geol. Soc., London, v. 144, p. 687-698.

Bain, R. J. (1990). Diagenetic, non-evaporitive origin for gypsum. Geology, v. 18, p. 447-450.

Barr, F. T. (1972a). Cretaceous biostratigraphy and planktonic foraminifera of Libya. Micropaleontology, v. 18, p. 1-46.

Bateman, R. M. and Konen, C. E. (1977). The log analyst and the programmable pocket calculator, part II-crossplot porosity and water saturation. The Log Analyst, v. 18, no. 6.

Bathurst, R. G. C. (1975). Carbonate Sediments and their Diagenesis. Developments in Sedimentology 12. (second edition). Elsevier, Amsterdam, 658p.

Bathurst, R. G. C. (1984). The integration of pressure-solution with mechanical compaction and sedimentation. In: Stylolite and Associated Phenomena Relevance to Hydrocarbon Reservoirs. Abu Dhabi Nat. Reserv. Res. Found. Spec. Publ., p. 41-55.

Bebout, D. G. and Pendexter, C. (1975). Secondary carbonate porosity as related to early Tertiary depositional facies, Zelten field. In: Geology and oil fields of Libya, Algeria and Tunisia. Bull. Am. Assoc. Petrol. Geol., Foreign repr. ser. 1, p. 67-95.

Beggren, W. A. (1969). Biostratigraphy and planktonic foraminifera zonation of the Tertiary system of the Sirte Basin of Libya, North Africa. In: Proc. 1st Int. Conf. Plankt. Microfossils (Ed. by P. Bronnimann and H. H. Renz). E. J. Brill, Leiden, p. 104-120.

Beggren, W. A. (1974). Paleocene benthonic foraminiferal biostratigraphy, biogeography and paleoecology of Libya and Mali. Micropaleontology, v. 20, p. 449-465.

Behrens, E. W. and Land, L. S. (1972). Subtidal Holocene dolomite, Baffin Bay, Texas. Jour. Sed. Petrol., v. 42, p. 155-161.

Bein, A. and Land, L. S. (1983). Carbonate sedimentation and diagenesis associated with Mg-Ca-Chloride brines: The Permian San Andres Formation in the Texas Panhandle. Jour. Sed. Petrol., v. 53, p. 243-260.

Braitsch, O. (1971). Salt Deposits, their origin and composition. N.Y., Springer-Verlag, 297p.

Coleman, M. L. and Moore, M. P. (1978). Direct reduction of sulfates to sulfur dioxide for isotopic analysis. Anal. Chem., v. 50, p. 1594-1595.

Conant, L. C. and Goudarzi, G. H. (1967). Stratigraphic and tectonic framework of Libya. In: Geology and oil fields of Libya, Algeria and Tunisia. Bull. Am. Assoc. Petrol. Geol., Foreign repr. ser. 1, p. 5-16.

Conley, C. D. (1971). Stratigraphy and lithofacies of Lower Paleocene rocks, Sirte Basin, Libya. In: Symp. Geol. Libya (Ed. by C. Gray). Fac. Sci. Univ. Libya, Tripoli, p. 127-140.

Colley, B. B. (1963). Libya: Petroleum geology and development. 6th World Petrol. Congr. (Frankfurt, 1963), sec. 1, pap. 43, 10 p.

Coplen, T. B., Kendall, C., and Hopple, J. (1983). Comparison of stable isotope reference samples. Nature, v. 302, p. 236-238.

Deffeyes, K. S., Lucia, F. J., and Weyl, P. K. (1965). Dolomitization of Recent and Plio-Pleistocene sediments by marine evaporite waters on Bonaire, Netherland Antilles. In: Dolomitization and Limestone Diagenesis-a Symposium (Ed. by L. C. Pray and R. C. Murray) Soc. Econ. Paleont. Miner. Spec. Publ. No. 13, p. 71-88.

Degens, E. T. and Epstein, S. (1964). Oxygen and carbon isotope ratio in coexisting calcite and dolomites from recent and ancient sediments. Geochim. et Cosmochim. Acta., v. 28, p. 23-44.

De Raaf, J. F. M., Reading, H. G. and Walker, R. G. (1965). Cyclic sedimentation in the Lower Westphalian of north Devon, England. Sedimentology, v. 4, p. 1-52.

Desio, A. (1970). Outlines and problems of the geomorphological evolution of Libya from the Tertiary to the Present day. In: Symp. Geol. Libya (Ed. C. Gray). Fac. Sci. Univ. Libya, Tripoli, p. 11-36.

Dickson, J. A. D. (1966). Carbonate identification and genesis as revealed by staining. Jour. Sed. Petrology, v. 36, p. 491-505.

Drever, J. I. (1974). The magnesium problem. In: The Sea (Ed. by E. D. Goldberg), v. 5, p. 1334-1336, Wiley Interscience, N.Y.

Elliott, G. F. (1968). Permian to Paleocene calcareous algae (Dasycladaceae) of the Middle East. Brit. Mus. (Nat. Hist.) Bull. Geol. Suppl. 4, 111p.

Enos, P. (1983). Shelf. In: Carbonate Depositional Environments (Ed. by P. A. Scholle, D. G. Bebout and C. H. Moore) Am. Assoc. petrol Geol. Mem. 33, p. 507-538.

Epstein, S., Graf, D. A., and Degens, E. T. (1964). Oxygen isotope studies on the origin of dolomites. In: Isotopic and Cosmic Chemistry (Ed. by H. Craig, S. L. Miller, and G. J. Wasserburg), p. 169-180. North Holland Publ. Co., Amsterdam, The Netherlands.

Fallick, A. E. (1991). Personal communication.

Folk, R. L. (1959). Practical petrographic classification of limestones. Bull. Am. Assoc. petrol. Geol., v. 43, pp. 1-38.

Folk, R. L. (1962). Spectral subdivision of limestone types. In: Classification of Carbonate Rocks (Ed. W. E. Ham). Am. Assoc. petrol. Geol. Mem. 1, p. 68-84.

Folk, R. L. (1965). Some aspects of recrystallization in ancient limestones. In: Dolomitization and Limestone Diagenesis (Ed. by L. C. Pray and R. C. Murray) Soc. Econ. Paleont. Miner. Spec. Publ. No. 13, p. 14-48.

Friedman, G. M. (1959). Identification of carbonate minerals by staining methods. Jour. Sedimentary Petrology, v. 29, p. 87-97.

Freidman, G. M. (1969). Trace elements as a possible environmental indicators in carbonate sediments. In: Depositional Environment in Carbonate Rocks (Ed. by G. M. Freidman) Spec. Publ. Soc. econ. Paleont. Miner. 14, p. 193-198.

Friedman, G. M. (1980). Dolomite is an evaporite mineral: evidence from the rock record and from sea-marginal ponds of the Red sea. In: Concepts and models of dolomitization (Ed. by D. H. Zenger, J. B. Dunham, and R. L. Ethington) Soc. Econ. Paleont. Miner. Spec. Publ. No. 28, p. 69-80.

Fritz, P. and Smith, D. G. W. (1970). The isotopic composition of secondary dolomites. Geochim. et Cosmochim. Acta, v. 34 p. 1161-1173.

Ginsburg, R. N. (1975). Tidal Deposits: A casebook of Recent Examples and Fossil Counterparts, 428 p. Spring-Verlag, New York.

Given, R. K. and Wilkinson, B. H. (1987). Dolomite abundance and stratigraphic age: constraints on rates and mechanisms of Phanerozoic dolostone formation. Jour. Sed. Petrol., v. 57, p. 1068-1078.

Gohrbandt, K. H. A. (1966b). Upper Cretaceous and Lower Tertiary stratigraphy along the western and southeastern edge of the Sirte Basin, Libya. In: South-central Libya and northern Chad (Ed. by J. J. Williams). Petrol. Explor. Soc. Libya, 8th Annu. Field Conf., p. 331-341.

Gumati, Y. D. and Kanes, W. H. (1985). Early Tertiary subsidence and sedimentation facies, northern Sirte Basin, Libya. Bull. Am. Assoc. Petrol. Geol., v. 69, p. 39-52.

Gumati, Y. D. and Nairn, A. E. M. (1991). Tectonic subsidence of the Sirte Basin, Libya. Jour. Petrol. Geol., v. 14, p. 93-102.

Hans, M. and Mountjoy, E. W. (1986). Chemistry and environments of dolomitization-a reappraisal. Earth Science Reviews, v. 23, p. 175-222.

Hardie, L. A. (1986a). Ancient carbonate tidal-flat deposits. Quart. Jour. Colorado Sch. Mines, v. 81, p. 37-57.

Hardie, L. A. (1986b). Startigraphic models for carbonate tidal flat deposition. Quart. Jour. Colorado Sch. Mines, v. 81, p. 59-74.

Hardie, L. A. and Eugster, H. P. (1971). The depositional environment of marine evaporites: a case for shallow, clastic accumulation. Sedimentology, v. 16, p. 187-220.

Holser, W. (1979). Trace elements and isotopes in evaporites. In: Marine Minerals (Ed. by R. G. Burns). Reviews in Mineralogy, Miner. Soc. Am., p. 293-346.

Hower, J., Eslinger, E. V., Hower, M. E., and Perry, E. A. (1976). Mechanism of burial metamorphism of argillaceous sediment: 1 mineralogical and chemical evidence. Geol. Soc. Am. Bull., v. 87, p. 725-737.

Irwin, M. L. (1965). General theory of epeiric clear water sedimentation. Bull. Am. Assoc. Petrol. Geol., v. 49, p. 445-459.

Jordi, H. A. and Lonfat, F. (1963). Stratigraphic subdivision and problems in Upper Cretaceous-Lower Tertiary deposits in northwestern Libya. Rev. Inst. Fr. Pet. Paris, v. 18, p. 1428-2436.

Kinsman, D. J. J. (1969). Interpretation of strontium concentrations in carbonate minerals and rocks. Jour. Sed. Petrol., v. 39, p. 486-508.

Kinsman, D. J. J. and Park, R. K. (1976). Algal belt and coastal sabkha evolution, Trucial Coast, Persian Gulf. In: Stromatolites (Ed. by M. R. Walter), p. 421-433.

Knauth, L. P. and Beeunas, M. A. (1985). Isotope geochemistry of fluid inclusions in Permian halite with implications for the isotopic history of ocean water and origin of saline formation water. Geochim. et Cosmochim. Acta., v. 50, p. 419-433.

Kretz, R. (1982). A model for the distribution of trace elements between calcite and dolomite. Geochim. Cosmochim. Acta, v. 46, p. 1979-1981.

Land, L. S. and Goreau, T. F. (1970). Submarine lithification of Jamaican reefs. Jour. Sed. Petrol., v. 40, p. 457-462.

Land, L. S. and Hoops, G. K. (1973). Sodium in carbonate sediments and rocks: a possible index to salinity of diagenetic solutions. Jour. Sed. Petrol., v. 43, p. 614-616.

Land L. S. (1980). The isotopic and trace element geochemistry of dolomite: the state of the art. In: Concepts and Models of Dolomitization (Ed. by D. H. Zenger, J. B. Dunham and R. L. Ethington) Spec. Publ. Soc. econ. Paleont. Miner. 28, p. 87-110.

Land, L. S. (1983). The application of stable isotopes to studies of the origin of dolomite and to problems of diagenesis of clastic sediments. In: Stable Isotopes in Sedimentary Geology (Ed. by M. A. Arthur and T. F. Anderson) Soc. econ. Paleont. Miner. Short Course No. 10, 4.1-4.22.

Land, L. S. (1985). The origin of massive dolomite. Jour. geol. Educ., v. 33, p. 112-125.

Laporte, L. F. (1967). Carbonate deposition near mean sea level and resultant facies mosaic: Manlius Formation (Lower Devonian) of New York State. Bull. Am. Assoc. petrol. Geol.,v. 51, p. 73-101.

Leake, B. E., Hendry, G. L., Kemp, A., Plant, A. G., Harvey, P. K., Wilson, J. R., Coats, J. S., Aucott, J. W., Lunel, T. and Howarth, R.J. (1969). The chemical analysis of rock powders by automatic X-ray fluorescence. Chemical Geology, v. 5, p. 7-86.

Leake, B. E. (1991). Personal communication.

Lehmann, E. P. (1964). Tertiary-Cretaceous boundary facies in the Sirte Basin. Proc. 22nd Int. Geol. Congr., (New Delhi), Pt. 3, p. 56-73.

Lindholm, R. C. and Finkelman, R. B. (1972). Calcite staining: semi-quantitative determination of ferrous iron. Jour. Sed. Petrology, v. 42, p. 239-242.

Lippmann, F. (1973). Sedimentary Carbonate Minerals. 228 p. Spring-Verlag, Berlin.

Logan, B. W., Rezaki, R. and Ginsburg, R. W. (1964). Classification and environmental significance of algal stromatolites. Jour. Geol., v. 72, p. 68-83.

Lucia, F. J. (1968). Recent sediments and diagenesis of south Bonaire, Netherlands Antilles. Jour. Sed. Petrol., v. 38, p. 845-858.

Magaritz, M., Goldenberg, L., Kafri, U., and Arad, A. (1980). Dolomite formation in the seawater-freshwater interface. Nature, v. 287, p. 622-624.

Mattes, D. h. and Mountjoy, E. W. (1980). Burial dolomitization of the Upper Devonian Miette buildup, Jasper National Park, Alberta. In: Cocepts and Models of Dolomitization (Ed. by D. H. Zenger, J. B. Dunham, and R. L. Ethington) Soc. Econ. Paleont. Miner. Spec. Publ. No. 28, p. 259-297.

McCrea, J. M. (1950). On the isotopic chemistry of carbonates and a paleo-temperature scale. Jour. Chem. Phys., v. 18, p. 849-857.

Mckee, E. D. and Gutschick, R. C. (1969). History of Redwell Limestone of northern Arizona. Geol. Soc. Am. Mem. 114, 726 p.

McKenzie, J. A. (1981). Holocene dolomitization of calcium carbonate sediments from the coastal sabkhas of Abu Dhabi: A stable isotope study. Jour. Geol., v. 89, p. 185-198.

Milliman, J. D. (1979). Marine Carbonates. Recent sedimentary carbonates, part I. 375 p., Spring-Verlag, Berlin.

Morrow, D. W. (1982a). Diagenesis I. Dolomite-part I. The chemistry of dolomitization and dolomite precipitation. Geoscience Canada, v. 9, p. 5-13.

Morrow, D. W. (1982b). Diagenesis II. Dolomite-part II. Dolomitization models and ancient dolostones. Geoscience Canada, v. 9, p. 95-107.

Murray, R. C. (1969). Hydrology of south Bonaire, Netherlands Antilles- a rock selective dolomitization model. Jour. Sed. Petrol., v. 15, p. 987-1035.

Patterson, R. J. and Kinsman, D. J. J. (1982). Formation of diagenetic dolomite in coastal sabkhas along the Arbian (Persian) Gulf. Am. Assoc. Petrol. Geol. Bull., v. 66, p. 28-43.

Petterson, J. A. and Hite, R. J. (1969). Pennsylvanian Evaporite- Carbonate cycles and their relation to petroleum occurrence, southern Rocky Mountains. Bull. Am. Assoc. petrol. Geol., v. 53, p. 884-908.

Pratt, B. R. and James, N. P. (1986). The St. George Group (Lower Ordovician) of western Newfoundland: tidal flat island model for carbonate sedimentation in shallow epeiric seas. Sedimentology, v. 33, p. 313-343.

Rittenhouse, G. (1971). Pore space reduction by solution and cementation. Am. Assoc. Petrol. Geol. Bull., v. 55, p. 80-91.

Royse, C. F., Wadell, J. S. and Petersen, L. E. (1971). X-ray determination of calcite-dolomite: an evaluation. Jour. Sed. Petrology, v. 41, pp. 483-488.

Schlumberger Well Services, Inc. (1972). Log Interpretation Manual, principles, v. 1, Houston. Schlumberger Well Services, Inc.

Schlumberger Well Services, Inc. (1984). Log Interpretation Charts, Houston. Schlumberger Well Services, Inc.

Scholle, P. A. and Halley, R. B. (1985). Burial diagenesis: out of sight, out of mind. In: Carbonate Cements (Ed. by N. Schneidermann and P. M. Harris) Soc. Econ. Paleont. Miner. Spec. Publ. No. 36, p. 309-334.

Schreiber, B. C. and Schreiber, E. (1977). The salt that was. Geology, v. 5, p. 527-528.

Schreiber, B. C. and Kinsman, D. J. J. (1975). New observation on the Pleistocene evaporites of Montallegro, Sicily and a modern analog. Jour. Sed. Petrol., v. 45, p. 469-479.

Schreiber, B. C., Roth, M. S. and Helman, M. L. (1982). Recognition of primary facies characteristics of evaporites and the differentiation of these forms from diagenetic overprints. Society of Economic Paleontologists and Mineralogists, core workshop 3, p. 1-32.

Shinn, E, A. (1968a). Practical significance of birds eye structures in carbonate rocks. Jour. Sed. Petrology, v. 38, p. 215-223.

Shinn, E, A. (1983a). Tidal flat environment. In: Carbonate Depositional Environments (Ed. by P. A. Scholle, D. G. Bebout and C. H. Moore). Am. Assoc. Petrol. Geol. Mem. 33, pp. 171-210.

Shinn, E. A. (1983b). Birdseyes, fenestrae, shrinkage pores, and loferites: a re-evaluation. Jour. sed. Petrology, v. 53, p. 619-629.

Shinn, E. A. (1986).Modern carbonate tidal flats: their diagenetic features. Quart. J. Colorado Sch. Mines, v. 81, p. 7-35.

Simms, M. (1984). Dolomitization by groundwater flow systems in carbonate platforms. Trans. Gulf Coast Assoc. Geol. Socs., v. 34, p. 411-420.

Sommer, S. E. (1972). Cathodoluminescence of carbonates, 1 characterization of cathodoluminescence from carbonate solid solution. Chem. Geol., v. 9, p. 257-273.

Tmalla, A. (1987). The Stratigraphy of B1-NC74F. Zueitina Oil Company. Unpublished Rep. No. PL10-87-2.

Taylor, T. R. and Sibley, D. F. (1986). Petrographic and geological characteristics of dolomite types and origin of ferroan dolomite in the Trenton Formation, Ordovician, Michigan Basin, USA. Sedimentology, v. 33, p. 61-86.

Tennant, C. B. and Berger, R. W. (1957). X-ray determination of dolomite-calcite ratio of a carbonate rock. Am. Mineralogist, v. 42, pp. 23-29.

Tucker, M. E. and Wright, V. P. (1990). Carbonate Sedimentology. 482 p., Blackwell Scientific Publications, Oxford.

Veizer, J. (1983a). Chemical diagenesis of carbonates: theory and application of trace element technique. In: Stable Isotopes in Sedimentary Geology (Ed. by M. A. Arthur and T. F. Anderson) Soc. Econ. Paleont. Miner. Short Course No. 10, 3.1-3.100.

Veizer, J. and Rudolf, D. (1974). Strontium as a tool in facies analysis. Jour. Sed. Petrol., v. 44, p. 93-115.

Veizer, J. and Lemieux, J., Jones, B., Gibling, M. R. and Savelle, J. (1978). Paleosalinity and dolomitization of Lower Paleozoic carbonate sequence, Somerset and Prince of Wales Islands, Arctic Canada. Can. Jour. Earth Science, v. 15, p. 1448-1461.

Wanless, H. R. (1979). Limestone response to stress: pressure solution and dolomitization. Jour. Sed. Petrol, v. 49, p. 437-462.

Watson, A. (1985). Structure, chemistry and origin of gypsum crusts in southern Tunisia and the central Namib Desert. Sedimentology, v. 32, p. 855-875.

Weber, J. N. (1964). Trace element composition of dolostones and dolomites and its bearing on the dolomite problem. Geochim. et Cosmochim. Acta, v. 28, p. 1817-1868.

Wilson, E. N., Hardie, L. A., and Phillips, D. M. (1990). Dolomitization front geometry, fluid flow patterns, and the origin of massive dolomite: The Triassic Latemar buildup, northern Italy. Am. Jour. Science, v. 290, p. 741-796.

Wilson, J. L. (1975). Carbonate Facies in Geologic History. 471 p. Spring-Verlag, Berlin.

Wray, J. L. (1977). Calcareous Algae. 185 p. Elsevier, Amsterdam.

Wyllie, M. R. J. and Rose, W. D. (1950). Some theoretical consideration related to the quantitative evaluations of the physical characteristics of reservoir rock from electric log data. Jour. Petroleum Technology, v. 189, p. 105-110.

APPENDIX A

During the course of this study, it was suspected that core 2 of well G4 was inverted and displaced, and that the upper part of the cored interval of well D2 was probably displaced also. In the case of well G4 core, this was implied by the complete mismatch between the core measured porosity data and the log derived porosity data, plotted at the reported core interval 1666-1671 m (5467-5482 ft) (Fig. A-1). This plot clearly shows that the two porosity curves have opposite trends in porosity with depth, suggesting that this core was possibly disoriented. On this assumption the core porosity data was inverted and plotted again. This resulted in the correction of the core porosiy trend, and the two curves began to show a similar trend in porosity with depth, but there were still some obvious differences in porosity values. However, the porosity differences became minimal when the core porosity curve was shifted down about 2.5 m (8 ft) deeper than the reported core top at 1666 m (5467 ft). This shift establishes the top of the core at 1669 m (5476 ft).

Since there is often some problem in porosity data derived from wireline logs, one might of course argue the validity of this assumption. However, the validity of using log porosity data in calibration was checked using porosity data measured from core 3 of the same well, which showed excellent match in porosity data between core measured porosity and log derived porosity (Fig. A-2), verifying, in this case, the reliability of using the log derived porosity data in the calibration.

In the case of well D2, the upper part of the cored interval was probably displaced, because there was a disagreement between the lithology described from this part of the core and its wireline log responses. For example, when this part was drawn at the reported core interval 1799-1807 m (5901-5929 ft), the shale unit of this part neither correlates with the high gamma-ray (GR) peak at 1798 m (5900 ft) nor with the shale unit at 1765 m (5790 ft) of well F1. Instead, this shale unit correlates with the lower readings of the GR curve at approximately 1800 m (5905 ft) of well D2, which indicate non shaliness, and laterally correlates with the evaporite sulfate unit of well F1 (Fig. A-3), suggesting that the upper part of well D2 core was probably displaced. Figure A-3, also shows the more likely orientation of the upper part of well D2 core after correction. It also shows that a good line of correlation with well F1 can now be seen.

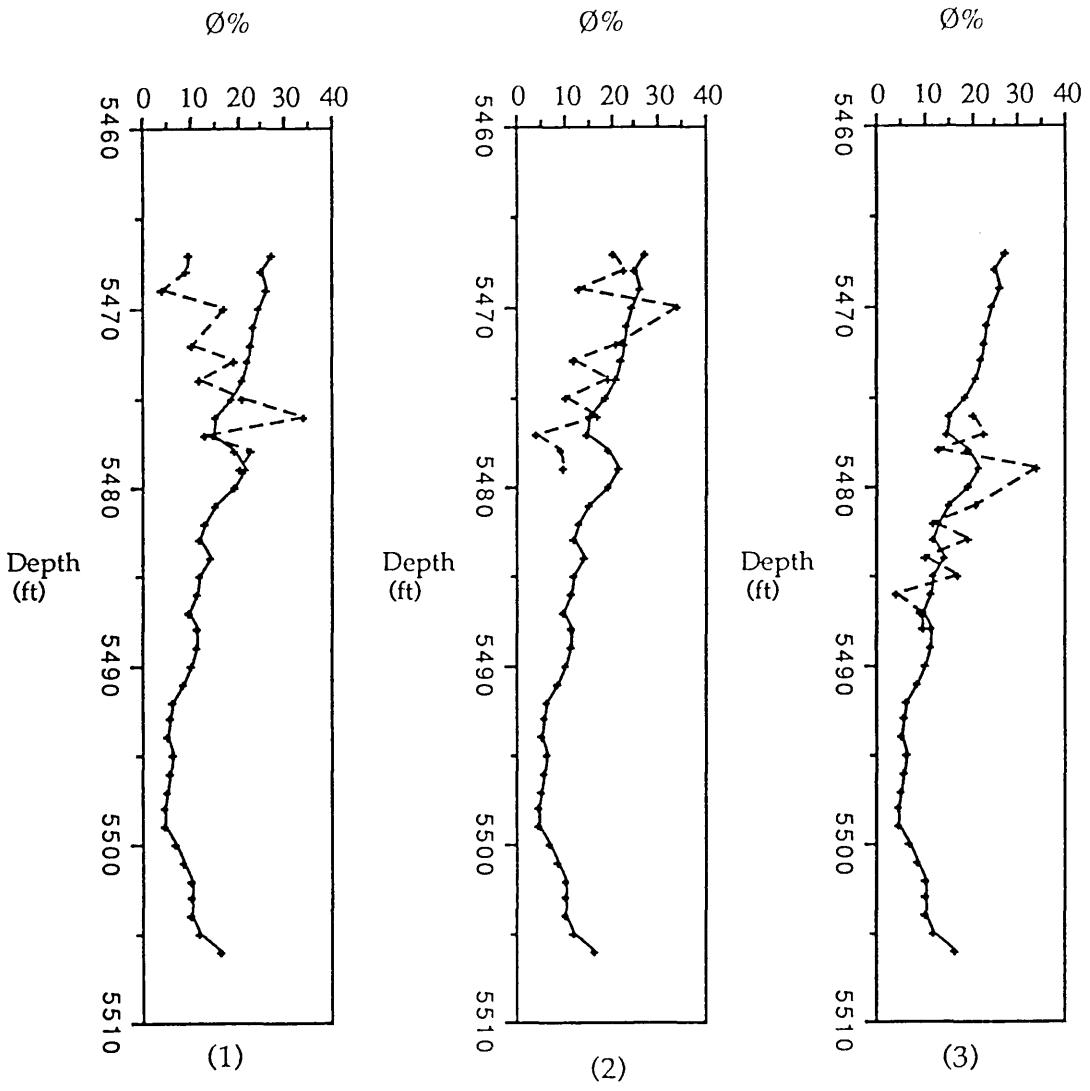

Fig. A-1, Correlations of log derived porosity (solid) with core measured porosity (dashed). (1) plot of porosity data before correction, showing clear mismatch, (2) plot of core porosity after have been invertad, but not depth-matched, showing a matched porosity trends, and (3) plot of the core porosity data after have been both inverted and depth-matched, showing good correlation.

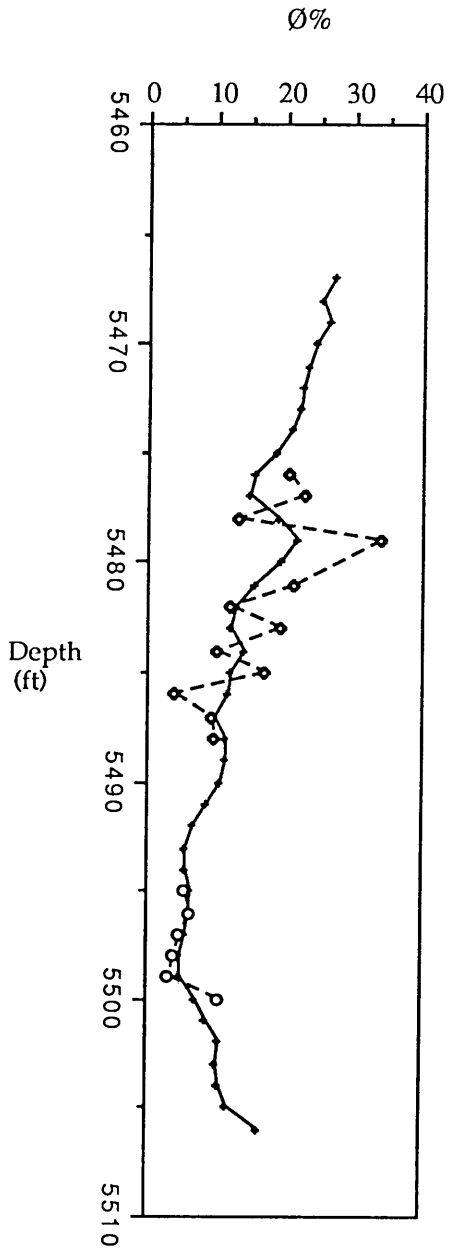

Fig. A-2, Plot of log porosity (solid), core 2 porosity (diamonds), and core 3 porosity (open circles) data, showing good correlation between the log calculated porosity and core 3 measured porosity data.

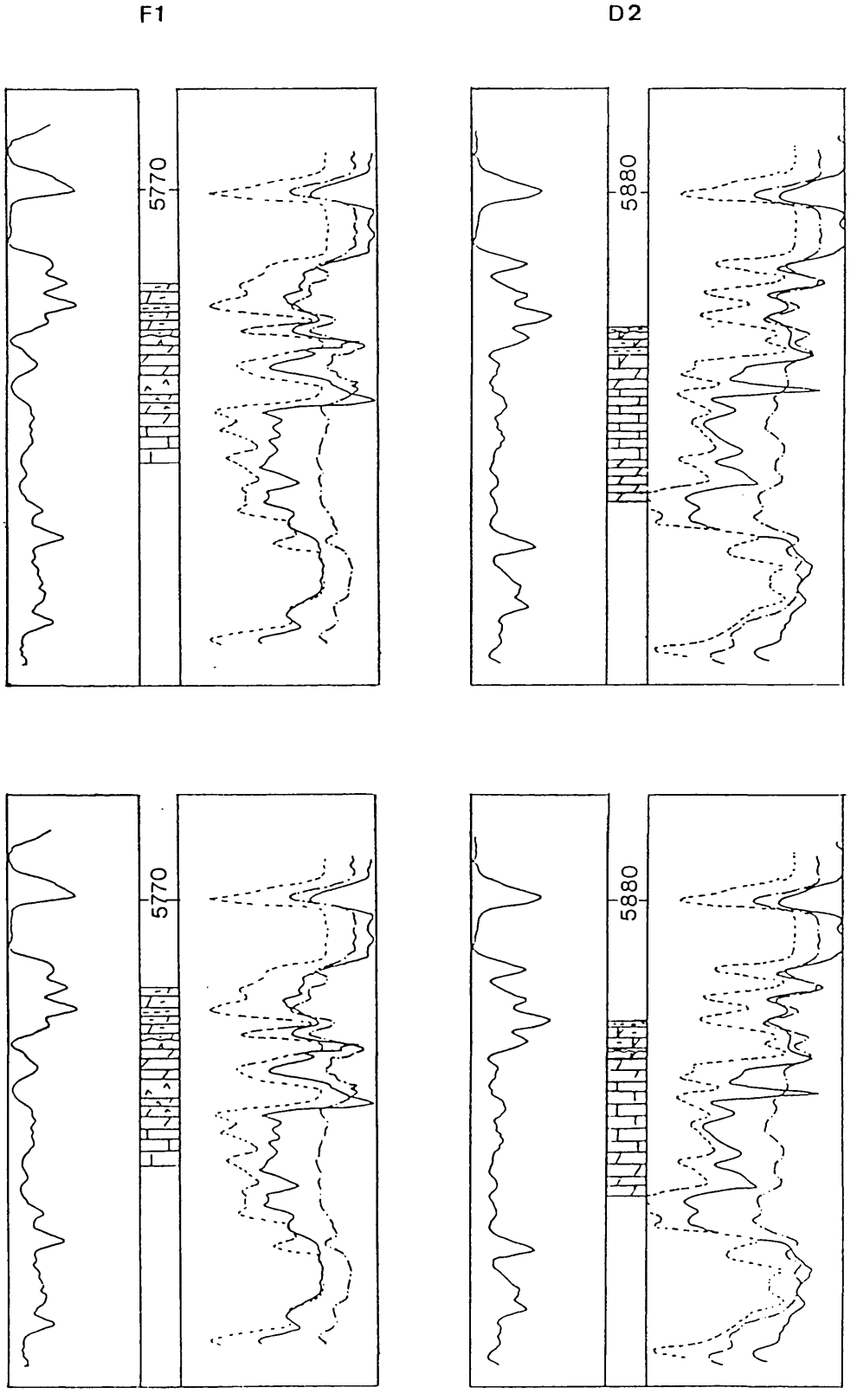

Fig. A-3, Correlation between wells D2 and F1, showing the upper part of the cored interval of well D2 before (top) and after correction (bottom).

APPENDIX B

B-1) Abbreviations

PDB	Pee Dee Belemnite
SMOW	standard mean ocean water
CDT	troilite of the Canon Diablo meteorite
PPM	parts per million
LDL-CNL*	litho-density and neutron compensated logs
LSS*	long space sonic.
BHC*	borehole compensated sonic log.
SPI	secondary porosity index.
DEP	depth

B-2) Symbols

Standards symb.	Program. symb.	Description
$\emptyset_N$	NEU	neutron log porosity.
ρ_b	DEN	bulk density of the formation.
ρ_{ma}	MD	density of matrix.
ρ_f	DF	density of fluid.
ΔT	SON	nterval transit time of the formation.
ΔTma	MT	interval transit time of matrix.
ΔTf	TF	interval transit time of fluid.
Ø (phi)	POR	porosity.
$\emptyset_D$	POR1	density derived porosity.
$\emptyset_{ND}$	POR2	neutron-density derived porosity.
$\emptyset_S$	POR3	sonic derived porosity.
SPI	POR4	secondary porosity index.

(*) Mark of Schlumberger

B-3) Calculation of total CO_2 (results are listed in Tables 3.1-3.4)

$$X1 = MgO_{(XRF)} \times Y$$
$$X2 = CaO_{(XRF)} \times Z$$
$$CO_{2(cal)} = X1 + X2$$

where:
$Y = CO_2$ (mol. wt.) + MgO (mol. wt.) = 1.0915
$Z = CO_2$ (mol. wt.) + CaO (mol. wt.) = 0.7848

B-4) Conversions between PDB ans SMOW Standards,

$$\delta^{18}O_{SMOW} = 1.03091 \times \delta^{18}O_{PDB} + 30.910$$
$$\delta^{18}O_{PDB} = 0.97002 \times \delta^{18}O_{SMOW} - 29.98$$

B-5) Calculation of $\delta^{18}O$ of water

$$10^3 \ln \alpha_{\text{dolomite-water}} = 2.78 \times 10^6 T^{-2} + .11$$

where:
$10^3 \ln \alpha_{\text{dolomite-water}} = \delta^{18}O_{dol} - \delta^{18}O_{water}$
T = temperature in ^oK

B-6) Porosity Calculation

1) Density derived porosity: (Schlumberger, 1972)

$$\emptyset_D = (\rho ma - \rho b) + (\rho ma - \rho f)$$

Where:
ρ ma = matrix density (Table 5.1,p. 105)
ρ f = 1.0

2) Neutron-density derived porosity: (Bateman & Konen, 1977)

a) if $\emptyset_N < \emptyset_D$

$$\emptyset_{ND} = (\emptyset_N - \emptyset_D \times y) + y$$

Where:

$y = 2.06 \times \emptyset_N + 1.17 + 10^x$

$x = 16 \times \emptyset_N \times 0.4$

b) if $\emptyset_N >= \emptyset_D$

$$\emptyset_{ND} = (z \times \emptyset_N - \emptyset_D \times y) + (z - y)$$

Where:

$y = 0.7 \times 10^x$

$x = 5 \times \emptyset_N + 0.16$

$z = (\rho ma - 4) + (\rho ma - \rho f)$

3) Sonic derived porosity and SPI: (Schlumberger, 1972)

$$\emptyset_S = (\Delta T - \Delta Tma) + (\Delta Tf - \Delta Tma)$$

$$SPI = \emptyset_{ND} - \emptyset_S$$

Where:

ΔTma = nterval transit of the matrix (Table 5.1,p. 105)

$\Delta Tf = 189$

APPENDIX C

This program was written to facilitate the calculation of porosity values. Logs required for this purpose are neutron-density and sonic logs. The program calculates the density derived porosity ($\emptyset_D$), neutron-density derived porosity ($\emptyset_{ND}$), and sonic derived porosity ($\emptyset_S$). The program operational coding are listed below

```
10 CLS
20 LET DEP = 0 : LET NEU = 0
30 LET DEN = 0 : LET SON = 0
40 LET MD = 0 : LET MT = 0
50 LET DF = 0 : LET TF = 0
60 INPUT "ENTER WELL FILE NAME :";NM$
70 OPEN NM$ AS #2 LEN=124
80 FIELD #2,8 AS DEP$,8 AS NEU$,8 AS DEN$,8 AS SON$
90 PRINT "ENTER WELL LOG DATA"
100 LOCATE 2,1
110 INPUT "TO END ENTERING OF DATA, INPUT 0 (zero) FOR DEPTH :"; DEP
120 LOCATE 5,1 : INPUT "DEPTH :"; DEP
130 LOCATE 6,1 : INPUT "NEUTRON (ØN) :"; NEU
140 LOCATE 7,1 : INPUT "DENSITY ( ρ b ) :"; DEN
150 LOCATE 8,1 : INPUT "SONIC ( Δ T) :"; SON
160 LOCATE 10,1 : INPUT "IS INPUT DATA CORRECT? (Y or N)";Y$
170 IF Y$ = "Y" THEN GOTO 180 ELSE GOTO 120
180 IF DEP=0 THEN GOTO 260
190 LSET DEP$ = STR$(DEP) : LSET NEU$ = STR$(NEU)
200 LSET DEN$ = STR$(DEN) : LSET SON$ = STR$(SON)
210 PUT #2,I
220 LET I = I + 1
230 LET DEP = 0 : LET NEU = 0
240 LET DEN = 0 : LET SON = 0
250 GOTO 120
```

```
260 CLS
270 LOCATE 2,1 : PRINT " ENTER RESERVOIR AND FLUID PARAMETERS "
280 LOCATE 5,1 : INPUT "Density of the matrix:"; MD
290 LOCATE 6,1 : INPUT "Interval transit time of the matrix:"; MT
300 LOCATE 7,1 : INPUT " Density of the fluid :"; DF
310 LOCATE 8,1 : INPUT " Interval transit time of the fluid :"; TF
320 LOCATE 10,1 : INPUT "IS INPUT DATA CORRECT? (Y or N)";Y$
330 IF Y$ = "Y" THEN GOTO 340 ELSE GOTO 280
340 CLS
350 LET I = 1
360 PRINT "POROSITY CALCULATION"
370 PRINT TAB(5);"Depth"; TAB(13);"Phi-D"; TAB(19);"Phi-ND"; TAB(26);"Phi-S";
TAB(32); "SPI"
380 GET #2,I
390 LET DEP = VAL(DEP$) : LET NEU = VAL(NEU$)
400 LET DEN = VAL(DEN$) : LET SON = VAL(SON$)
410 IF DEP = 0 THEN GOTO 600
420 LET NEU = NEU/100
430 LET POR1 = (MD-DEN) / (MD-DF)
440 IF NEU < POR1 THEN GOTO 490
450 LET Z = (MD-4)/(MD-DF)
460 LET X = -(5 * NEU + 0.16)
470 LET Y = 0.7 - 10^X
480 GOTO 520
490 LET Z = 1
500 LET X = -(16 * NEU + 0.4)
510 LET Y = -(2.06 * NEU + 1.17) + 10^X
520 LET POR2 = (Z * NEU) - (POR1 * Y) / (Z - Y)
540 LET POR3 = (SON - MT) / (TF - MT)
550 IF POR2 <= POR3 THEN LET SPI = 0 : ELSE LET POR4 = POR2 - POR3
560 LET FF$ = ####   ##.##   ##.##   ##.##   ##.##
570 PRINT USING FF$; VAL(DEP$), POR1, POR2, POR3, POR4
580 LET I = I + 1
590 GOTO 380
600 CLOSE #2
610 CLS
620 END
```